UNIVERSITY OF ICELAND

GRÓ · GTP Geothermal Training Programme

unesco Centre Under the auspices of UNESCO

M.S. thesis in Geophysics

Analysis, 2D and 1D Joint Inversion of Magnetotelluric and Transient Electromagnetic Data from Buranga Geothermal Prospect, Uganda

Fred Ssemuyaba

June 2024

FACULTY OF EARTH SCIENCES

Analysis, 2D and 1D Joint Inversion of Magnetotelluric and Transient Electromagnetic Data from Buranga Geothermal Prospect, Uganda

Fred Ssemuyaba

Thesis submitted in partial fulfillment of a
Magister Scientiarum degree in Geophysics

M.S. Committee
Gylfi Páll Hersir
Ásdís Benediktsdóttir
Halldór Geirsson

Master's Examiner
Kristján Óttar Klausen

Faculty of Earth Sciences
School of Engineering and Natural Sciences
University of Iceland
Reykjavik, June 2024

Analysis, 2D and 1D Joint Inversion of Magnetotelluric and Transient Electromagnetic Data from Buranga Geothermal Prospect, Uganda

60 ECTS thesis submitted in partial fulfilment of an *M.S. degree in Geophysics.*

Faculty of Natural Sciences
School of Engineering and Natural Sciences
University of Iceland
Sturlugata 7,
101 Reykjavik
Iceland

Telephone: 525 4000

Bibliographic information:
Ssemuyaba, F., 2024, *Analysis, 2D and 1D Joint Inversion of Magnetotelluric and Transient Electromagnetic Data from Buranga Geothermal Prospect, Uganda*, MS. thesis Faculty of Earth Sciences, University of Iceland, XX pp.

ISBN XX
Printing:

Abstract

Resistivity surveying is considered one of the most important methods when it comes to geothermal exploration due to its direct relationship with reservoir temperature and other physical properties. However, the choice of an appropriate interpretation technique is not always straightforward. In this study, results obtained through different interpretation techniques of electromagnetic data from the Buranga geothermal prospect in Uganda are compared to identify the most suitable interpretation technique. It is then used to assess the presence and understand the resistivity structure that characterizes the nature of the resource at Buranga.

Resistivity data from closely located Transient Electromagnetic (TEM) sites (88 stations) and Magnetotelluric (MT) sites (165 stations) are used in a 1D joint inversion to correct for static shifts caused mainly by near-surface inhomogeneities. Results of the 1D inversion from the rotationally invariant determinant and average as well as the rotationally variant XY and YX apparent resistivity and phase presented as depth slices and cross-sections are compared. Static shift factors from the 1D joint inversion for both the Transverse Electric (TE) and Transverse Magnetic (TM) modes are used in the 2D inversion of the MT data. Convergence and robustness of the 2D models are explored by using 100 Ωm and 30 Ωm homogeneous half-space initial models which yielded similar results and are presented as cross-sections with an RMS between 1.0 - 1.9 for all the TE, TM, TE+TM and TE+TM+Tzy modes.

Results from the 1D inversion show similarities for the average and the determinant apparent resistivity while for the XY and YX apparent resistivity and phase, they differ immensely as the YX is more influenced by the conductive structures while the XY strikes a balance between near-surface conductive structures and deep resistive structures. 2D resistivity models compare well with the 1D results of the XY apparent resistivity and phase and thus the general subsurface resistivity interpretations are based on the XY inversion results and the 2D TE+TM mode inversion. Both 1D and 2D models highlight a surface layer which corresponds to fresh unaltered rocks. It is underlain by a very conductive zone that could represent sediments that have been overly infiltrated with geothermal fluids. Underneath these sediments is a layer of relatively high resistivity which can be thought of as basement rocks. Below 5 km depth a high conductivity structure emerges which has been left out of the interpretation here due to poor data quality and hence resolution constraints of the data set at hand. The preliminary resistivity conceptual model characterizes Buranga as a low to medium-temperature, deep-circulation amagmatic fault-controlled system extracting heat from the crustal heat flow. Up-flow is due to buoyancy-driven convection within the permeable damage zones and fault splays along multiple fault segments linked to the N to NE striking west-dipping faults.

Útdráttur

Viðnámsmælingar eru taldar ein mikilvægasta aðferðin við jarðhitarannsóknir vegna þess beina sambands sem ríkir milli viðnáms og hitastigs í jarðhitageyminum sem og við ýmsar aðrar eðlisbreytur. Engu að síður er túlkun mæligagna nokkrum annmörkum háð. Hér eru bornar saman niðurstöður mismunandi aðferða við túlkun gagna úr rafsegulmælingum frá Buranga jarðhitasvæðinu í Úganda í því skyni að leiða fram eðlilegustu túlkunaraðferðina. Henni er síðan beitt til þess að meta og átta sig á viðnámsgerðinni sem einkennir jarðhitaauðlindina í Buranga.

Viðnámsmæligögn frá samliggjandi/nærliggjandi TEM mælingum (88 talsins) og MT mælingum (165 talsins) voru samtúlkuð einvítt þar sem leiðrétt var fyrir hliðrun MT mæligagna vegna viðnámsóreglu nærri yfirborði jarðar. Niðurstöður einvíðrar túlkunar snúnings óháðra gagna, ákveðnu og meðalgildi sýndarviðnáms og fasa ásamt snúnings háðum gögnum, XY og YX sýndarviðnámi og fasa eru sýndar sem lárétt og lóðrétt þversnið og bornin saman. Hliðrunarþátturinn samkvæmt einvíðri samtúlkun gagna er nýttur við tvívíða túlkun MT gagna fyrir bæði rafsviðið á þverveginn (TE) og fyrir segulsviðið á þverveginn (TM). Áreiðanleiki tvívíðrar túlkunar var kannaður sérstaklega með því að nota tvö byrjunarlíkön, 100 Ωm and 30 Ωm einsleit hálfrúm. Niðurstöður voru svipaðar og eru sýndar sem þversnið ásamt óvissu (RMS) sem var milli 1,0 og 1,9 fyrir öll gögn TE, TM, TE+TM og TE+TM+Tzy.

Niðurstöður einvíðrar túlkunar eru svipaðar fyrir ákveðnu og meðalgildi sýndarviðnáms og fasa. Þær eru hins vegar töluvert frábrugðnar fyrir XY og YX sýndarviðnám og fasa, YX mjög háð velleiðandi skrokkum en XY þræðir meðveg milli velleiðandi skrokka nærri yfirborði og háviðnáms skrokka dýpra í jörðu. Tvívíðu viðnáms líkönunum ber ágætlega saman við einvíða XY líkanið. Því er hin almenna viðnámstúlkun byggð á niðurstöðu XY einvíðu túlkunarinnar ásamt tvívíðu TE+TM túlkuninni. Bæði ein- og tvívíðu líkönin sýna yfirborðslag sem svarar til fersks óummyndaðs bergs. Neðan þess er mjög velleiðandi lag sem gæti verið set sem jafnframt inniheldur jarðhitavökva. Neðan þessara setlaga er lag með tiltölulega háu viðnámi sem endurspeglar væntanlega berggrunninn. Neðan 5 km dýpis kemur í ljós mjög velleiðandi skrokkur. Hann var ekki hafður með í túlkuninni vegna þess hve mæligögnin sem svara til þessa dýpis voru með lélega upplausn.

Bráðabirgða hugmyndalíkan einkum samkvæmt viðnámsgerðinni bendir til þess að Buranga sé lághita eða meðalstigshita djúpstætt kerfi, tengt misgengjum, en ótengt eldvirkni, sem sæki hita frá varmaflæði skorpunnar. Flotkrafturinn knýr áfram uppstreymið í hringsteymi inn í lekum sprungum og opnum misgengum sem tengjast norður- til norðaustlægum misgengum sem halla til vesturs.

Dedication

I dedicate this work to my wife and kids.

Table of Contents

List of Figures

Abbreviations

GRD	Geothermal Resources Department
MT	Magnetotelluric
TEM	Transient Electromagnetic
EM	Electromagnetic
EARS	East African Rift System
NASA	National Aeronautics and Space Administration
TE	Transverse Electric
TM	Transverse Magnetic
Det	Determinant
Ave	Average
GoU	Government of the Republic of Uganda
OPEC	Organization of Petroleum Exporting Countries
ICEIDA	Icelandic International Development Agency
UNDP	United Nations Development Programme
IAEA	International Atomic Energy Agency
MEMD	Ministry of Energy and Mineral Development
UGRDP	Uganda Geothermal Resources Development Programme
CNOC	China National Oil Company
GMT	Generic Mapping Tools
1D	One Dimension
EAGER	East African Geothermal Energy Facility
2D	Two Dimension
3D	Three Dimension

Acknowledgements

Every man must walk his journey. However, along the way, we meet people who make the journey easier, more fulfilling and memorable. Firstly, I would like to acknowledge the leadership at both the Ministry of Energy and Mineral Development and the Geothermal Resources Department for granting me the study leave and allowing me to use the data. GRÓ GTP is acknowledged for awarding me a scholarship to pursue postgraduate studies at the University of Iceland.

Special thanks go to my supervisors, Mr. Gylfi Páll Hersir and Mrs. Ásdís Benediktsdóttir for their unwavering support and guidance during the entire period of writing this thesis. I also extend my appreciation to the staff at the GRO-GTP, Málfríður Ómarsdóttir, Ingimar G. Haraldsson, Vigdís Harðardóttir (retired) and Director Guðni Axelsson, thank you for making Iceland a home away from home for me.

To my wife, our youngest son was born while I was away, and I know it was not an easy feat for you, but you have remained strong, resolute, and composed to go through it all by yourself and at the same time take care of the kids. Thank you for all the sacrifices during my long absence. And to my kids, I would like to applaud you for your patience and understanding during this period and may you be blessed as you grow up. To my Mum and Dad, you cannot imagine how your constant messages of encouragement and prayers kept me going, I can never thank you enough for the things you do for me.

I would like to make a notable mention of my colleagues Mayra Hernandez, Didas Makoye, and Paula Babirye for your support and the entire geophysics team at GRD, Uganda for collecting the data used in this thesis.

1 Introduction

The advancement in electromagnetic (EM) data acquisition and analysis techniques over the last five decades has enormously improved surface exploration studies of geothermal resources all over the world. The Magnetotelluric (MT) and transient electromagnetic (TEM) methods are now the primary geophysical mapping and exploration techniques for green field geothermal areas because geothermal fields produce strong variations in subsurface electrical resistivity that can be easily mapped out by MT and TEM. Improved computational capabilities have made it possible to characterize the resistivity structures more clearly and precisely through well-constrained models and inversions.

Over the recent past, the Ministry of Energy and Mineral Development of Uganda, through the Geothermal Resources Department (GRD) embarked on the search for alternative energy sources in response to the ever-increasing demand for clean, renewable and sustainable energy resources to support the growing economy in the different sectors such as agriculture, extractive industries, manufacturing industries, tourism, and other small scale value addition chains. One of the energy resources that has been earmarked for exploitation is the geothermal energy resource.

Geothermal prospects in Uganda are in the western branch of the East African Rift System (EARS) in the Albertine Graben and thus are mostly fault-controlled deep circulation systems (Kahwa et al., 2020). Therefore, these areas are somewhat special compared to conventional high-temperature volcanic-hosted geothermal fields that are found in the Eastern branch of the EARS and other parts of the world. Owing to the uniqueness of the prospects in Uganda, GRD has adapted a site-specific approach of exploration focusing on acquiring geoscientific data and integrating the results in conceptual models directed at targeting geothermal reservoirs heated by deep circulation, like those typical of the United States Basin and Range as well as Western Turkey (Heath et al., 2018) This site-specific exploration approach is aimed at reducing the upfront risks associated with drilling in deep circulation fault-controlled systems that might arise if proper geoscientific data integration is not undertaken.

Therefore, in addition to structural geological mapping campaigns and geochemical surveys, MT and TEM resistivity surveys have been undertaken at Buranga (also known as Sempaya) to help investigate the characteristics of the resistivity structure in the area to allow for proper delineation of an exploitable geothermal reservoir, as well as establishing the potential resource size (Ssemuyaba, 2021; Ssemuyaba et al., 2023). In addition, resistivity surveys at Buranga were intended to identify fault offsets of low-resistivity sediments and high-resistivity Precambrian rocks and detect low-resistivity clay caps over possible high-resistivity reservoirs in the sediments. The MT method has successfully been used to detect and characterize geothermal areas located in similar extensional tectonics where faults and fractures play a significant role in the deep circulation of geothermal fluids and heat transfer from deep to shallow crustal levels (Kahwa et al., 2020); (Faulds & Hinz, 2015).

This thesis focuses on the processing and 1D joint inversion of MT and TEM data as well as the 2D inversion of MT data collected at Buranga. The results were integrated with other

geological information to generate a conceptual model which will help decision-making on whether to drill and if so, where to drill temperature gradient wells which are less expensive compared to conventional deep exploration drilling.

Chapter 2 introduces the area of interest describing its location, the regional and local underlying geology, the location of surface geothermal manifestations as well as visible fault structures and lineaments. In addition, the general EARS structure is described highlighting the major spreading events and the seismicity of the area. Chapter 3 summarizes the previous exploration activities undertaken at the Buranga prospect under the different campaigns. The exploration activities include surface geological mapping, structural geological mapping, geochemical and isotope surveys, micro-earthquake surveys, gravity, TEM, and MT surveys. Findings from early drilling campaigns are also presented.

The main geothermal exploration methods are introduced in Chapter 4, highlighting their basic theory, application, and relevance in characterizing geothermal resources. Chapter 5 expounds on Chapter 4 by going into detail about the working principles of the TEM and MT methods. Maxwell's equations and the concepts of electromagnetic induction within the earth are discussed as well as the MT transfer functions, impedance tensors, strike analysis and dimensionality.

Chapter 6 discusses the electromagnetic distortions within the earth that effectively contribute to the so-called static shift effect. Further emphasis is put on the correction of these distortions, especially by inverting co-located TEM and MT data. Field set-up and data acquisition are described in detail for the MT and TEM methods. Chapter 7 deals with the treatment of data after field acquisition starting from MT time series processing, data editing, static shift correction, and geo-electric strike analysis to 1D joint inversion of MT and TEM data and 2D inversion of MT data. The algorithms of the 1D and 2D inversion codes are also discussed. Chapter 8 deals with the results of the inversions comparing the 1D inversion results of the transverse electric (TE), transverse magnetic (TM), determinant and average modes. The chapter concludes with discussions on the interpretation of the results from a geothermal point of view characterizing the resistivity structure at Buranga and then building a preliminary conceptual model of the area. An insight into the most probable areas for drilling temperature gradient wells has been given to aid decision-making regarding the next step in the exploration program. Chapter 9 summarizes the key recommendations for future work.

2 Location and Geological Overview of Buranga Geothermal prospect

The Buranga geothermal field is located in the Western branch of the East African Rift System (EARS) (Figure 2.1) that runs along the joint border of Uganda and the Democratic Republic of Congo. The Buranga geothermal field is located in the Kasitu sub-county in Bwamba county of Bundibugyo district (Nyakecho, 2008) (Sempaya geologic map sheet 56/1). It is located 50 km southwest of Fort Portal town in Bundibugyo district which lies in Western Uganda (Figure 2.2).

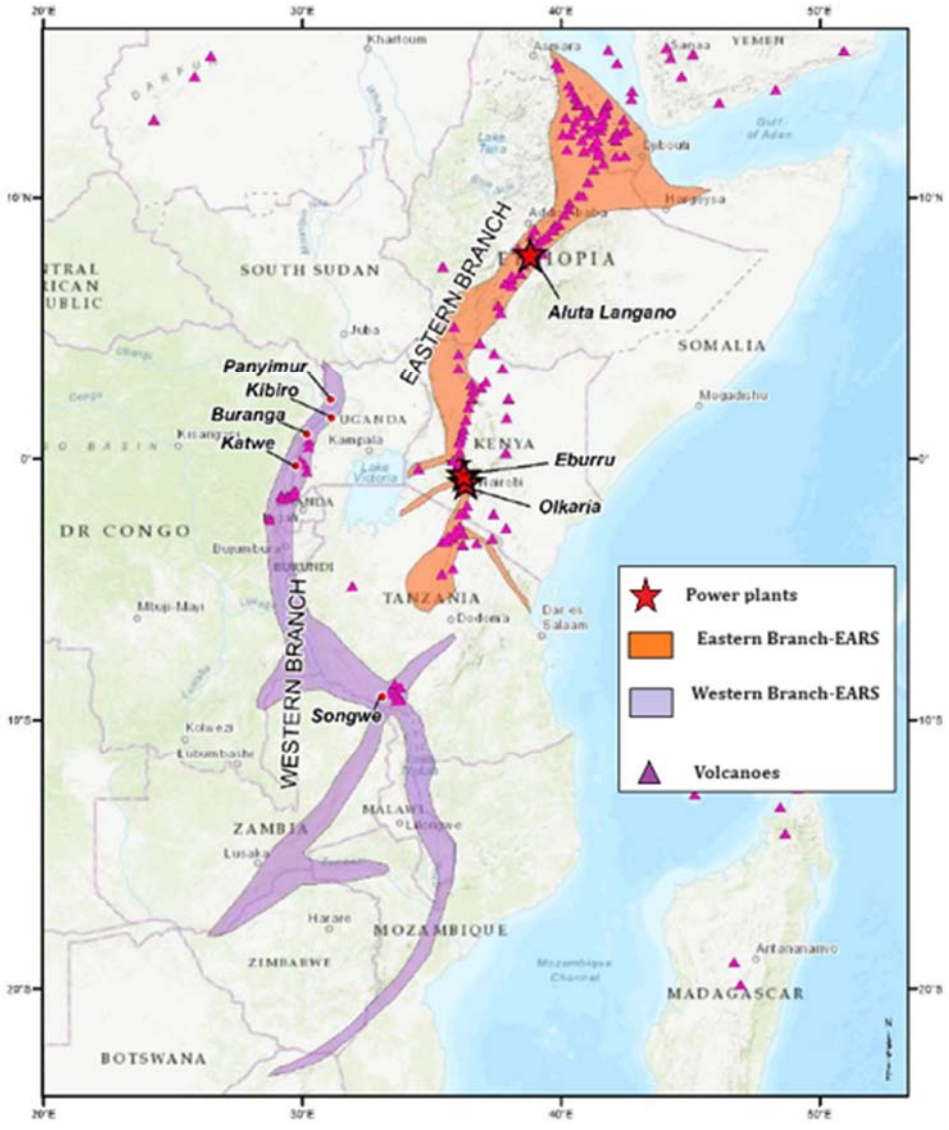

Figure 2.1: Map showing the extent of the EARS and the location of major central volcanoes within the rift. Geothermal power plants are shown by red stars and geothermal prospects as red circles. Modified from (Hinz et al., 2018)

2.1 Regional and Local Geology

The spreading of EARS began at least 15 million years ago in Miocene time. The Western Rift is considered to be younger (late Miocene-Recent) than the more mature Eastern branch (Morley & Wescott, 1999); (Lindenfeld et al., 2012). The region of the rift has a markedly higher heat flow than the surrounding pre-Cambrian terrain (Natukunda, 2010). In Uganda, the high heat flow within the Western branch of the rift valley is located within the precincts of the rift system. Geothermal areas where visible surface manifestations are found include, Panyimur, Amoro, Amoropi, Kibiro, Buranga, Kibenge, Kabuga, Katwe, Ihimbo, Kiruruma, Kisizi, Rubaare, Karagamba, Minera and other small-scale manifestations (see Figure 2.2). The major geothermal prospects in Uganda are Buranga, Katwe, Kibiro and Panyimur but in total there are over 28 geothermally active sites in the country all spread along the western branch of the EARS, except for Kanagorok and Kaitabosi which are situated on the eastern side of the country close to the Eastern branch of the EARS (Armannsson et al., 2007)

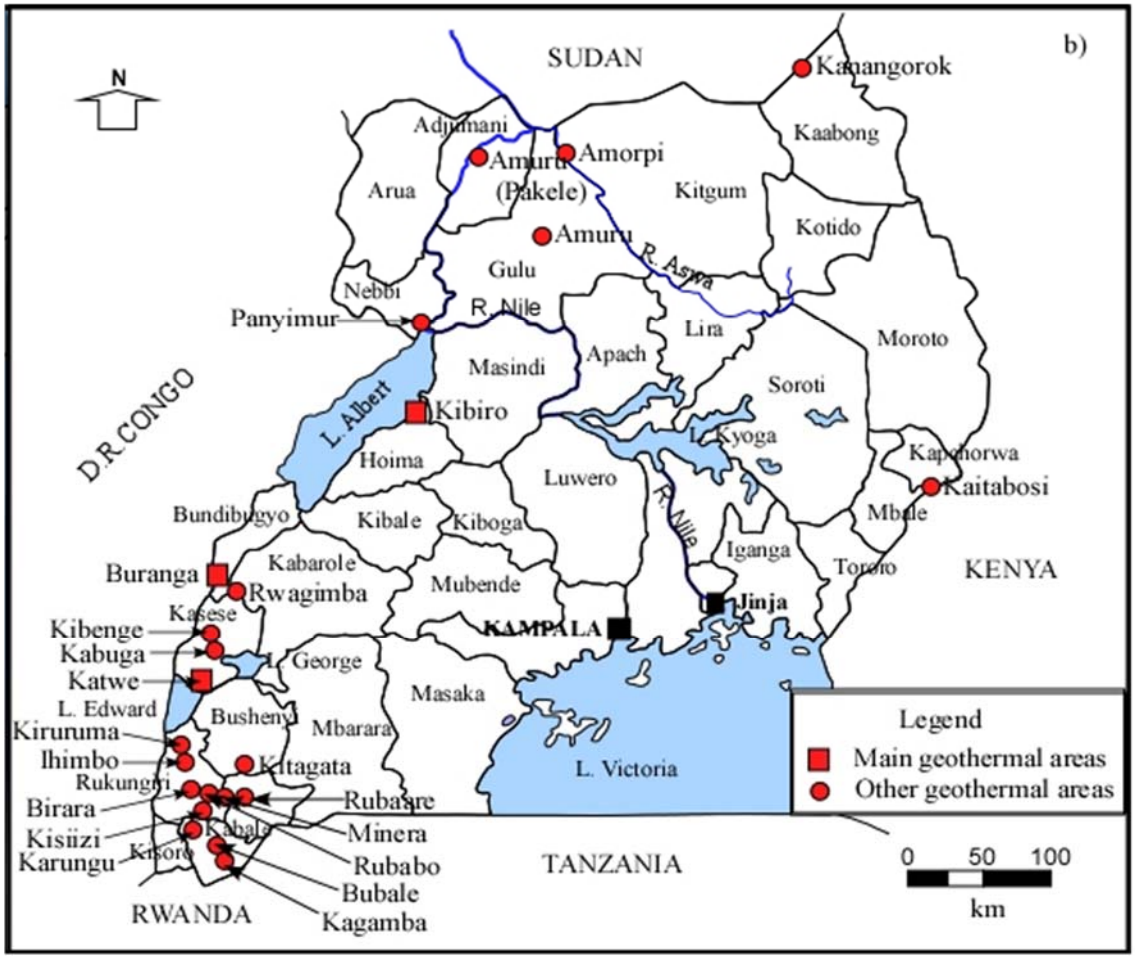

Figure 2.2: Map of Uganda showing the location of all the known geothermal prospects within the country. Adopted from Nyakecho, (2008).

Uganda comprises an exposed pre-Cambrian basement divided by the Western branch of the East African Rift System in the western part of the country. The Western branch, known as the Albertine Rift, starts north at the Sudan border, curves to the west and then southwest along the border with the Democratic Republic of Congo, and then runs south to Rwanda, Burundi, and western Tanzania (Figure 2.1).

Two different echelon strands are found in the Western Rift Valley, separated by the Rwenzori Mountains (Figure 2.3), which rise from a base of less than 1,000 m a.s.l. in the rift to over 5,000 m a.s.l. There are thick layers of late Tertiary and Quaternary sediments, freshwater, and saline crater lakes. Volcanic and plutonic bodies have been identified beneath L. Albert and L. Edward in the south (EDICON, 1984); (Natukunda, 2010).

Buranga geothermal area is situated at the north-western base of the Rwenzori Mountains in the Western Rift Valley. Surface geological mapping has noted a tertiary succession of sands, clays and boulder beds with occasional tuffs (Figure 2.3). Geological logs from the old, drilled boreholes at Buranga indicate that the tertiary succession is terminated in the main Bwamba fault (Figure 2.3) zone by a breccia cemented by calc tuff followed by mylonite (Harris et al., 1956; Natukunda, 2010). In addition, according to Natukunda (2010),

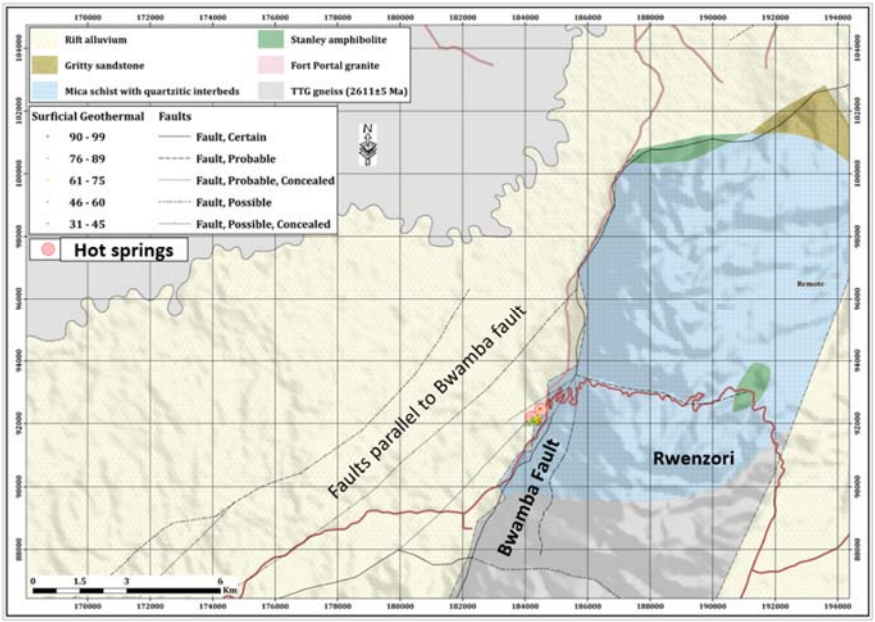

Figure 2.3: Map showing the local geology at the Buranga prospect together with the mapped faults shown as grey dotted lines.

the clays have various colours, and the sands are fine to medium-grained, varying in colour between white, brown, grey, and green. Clay is the most common binding material although patchily replaced by calcium carbonate giving rise to calcareous sandstones and grits.

This prospect area is in the Semliki Kaiso sedimentary basin some 300 to 600 m to the northwest of the Bwamba escarpment which forms the NW boundary of the Rwenzori Massif. It lies under the Bwamba fault, which strikes 20-40° to the northeast and has a dip of 60-65° to the west (Natukunda, 2010). The sedimentary basin around Buranga is generally covered with boulder beds and scree but geothermal activity is found in an area of swamps and rain forest. Surface manifestations cover an area of about 0.125 km^2 (Hinz et al., 2017) and consist of three main hot spring areas: Mumbuga Springs, the Nyansimbe pool and the Kagoro Springs (Figure 2.4). These three groups of springs lay approximately on a line extending some 550 m along a strike N-35°-E, approximately parallel to the Bwamba fault. In addition to these three hot spring groups, over seventy-six springs (Figure 2.4) with temperatures greater than 31°C were mapped in 2017 by inserting 1 m deep temperature

probes in the spring.

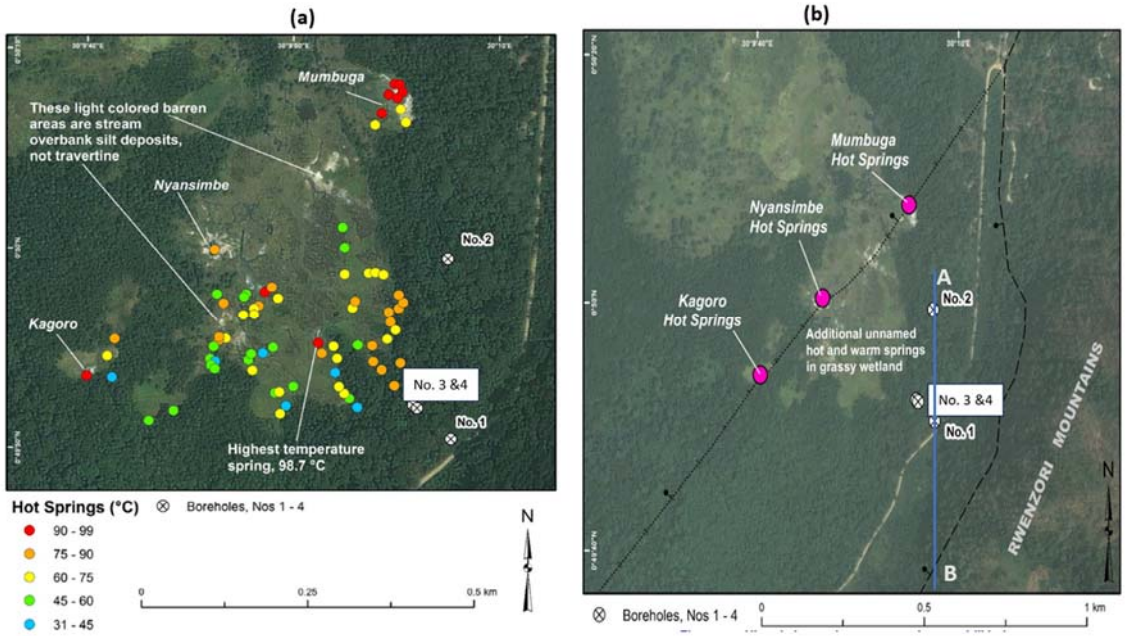

Figure 2.4: (a) Surface geothermal manifestations mapped at Buranga prospect. Brown patches indicate active and non-active travertine moulds, and coloured circles are the mapped hot springs with their measured temperatures as of 2017 (b) The three major hot springs with mapped faults and boreholes 1-4. Line AB represents a cross-section between boreholes 1 and 2. Adapted from Hinz et al. (2017).

Travertine moulds are seen around the three hot spring clusters of Mumbuga, Nyansimbe and Kagoro.

2.1.1 Structural Geology and Fault Dip Measurements

The range-front fault system around the Buranga geothermal prospect consists of several 0.5 -1 km left and right steps (Hinz et al., 2017) with Buranga sitting adjacent to a 0.5 km wide left step along the range front (Figure 2.5). Measured dips on exposed fault surfaces in Precambrian rock East of the hot springs range from 50-60°, an average of 55° to NW similar to 64° trigonometric calculation based on the intercept in borehole 1 (McConnell & Brown, 1954) Striations indicate dip-slip motion and a WNW-ESE extension direction.

During a post-field presentation in 2017, the East Africa Geothermal Energy Facility (EAGER) team described the faults surrounding the Rwenzori block and through the prospect area as being Quaternary active structures with the footwall and hanging wall faults being associated with the Quaternary fault scarp (Hinz et al., 2017). The area is highly vegetated, so smaller Quaternary fault scarps and fault splays are probably not recognized.

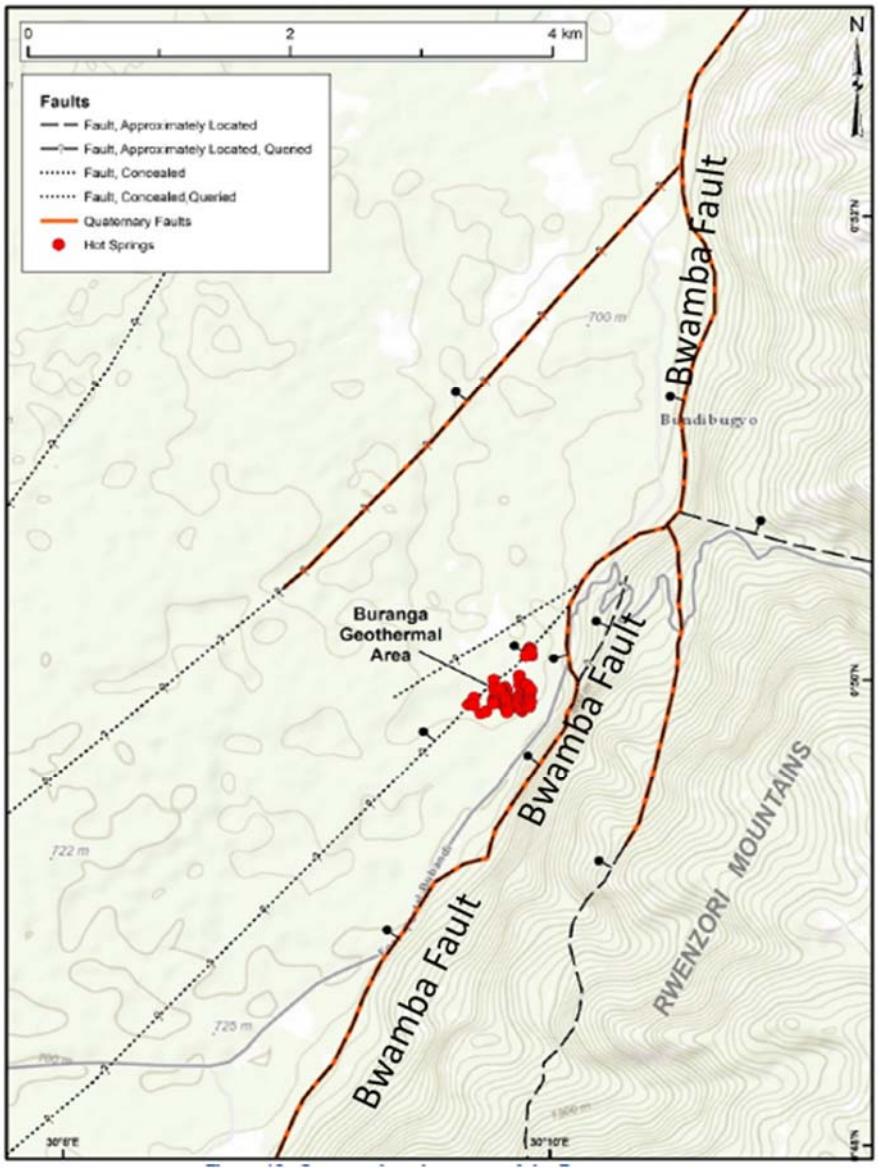

Figure 2.5: Structural geology setting at Buranga geothermal prospect. Orange and black-dotted lines represent quaternary and concealed faults, respectively. Adapted from Hinz et al. (2017).

The Kagoro, Mumbuga and Nyansimbe hot springs lie along line N45°E (Figure 3.1) and are believed to be associated with a step-over fault parallel to the main escarpment. The dense vegetation at Buranga makes it difficult to recognize and map out other key quaternary fault scarp details that might be present. Hot springs have not been identified northwest of the concealed NE striking fault on which the three hot springs lie, this fault may act as a barrier or as both a barrier and conductor of fluid flow (Hinz et al., 2017). On the southern side of this concealed fault, however, several hot spring fissures are observed with approximately N20°E trends and some have temperatures greater than 70°C (Hinz et al., 2017). The hot spring trends are also parallel to the local range fault which may indicate that there are several N to NNE striking faults and fractures that underline the Buranga field between the range-front fault and the outer NE striking concealed normal fault. The distribution of the active hot springs at Buranga suggests an upflow along multiple segments within the step-over probably along the primary range-front fault, the outer concealed NE striking fault or even in any cross-cutting concealed faults.

3 Previous Exploration Activities

According to Kato (2016) the earliest geothermal exploration activities in Uganda date as far back as the early 1950s. However, the first detailed exploration phase was undertaken as a collaboration between the Government of Uganda (GoU), the Organization of Petroleum Exporting Countries (OPEC), the Government of Iceland through ICEIDA (The Icelandic International Development Agency) and the United Nations Development Program (UNDP) in 1993-1994 where three (3) high ranking prospects i.e., Katwe, Buranga, and Kibiro were investigated (Armannsson, 1994). The primary activities included geological, geochemical, and isotope surveys. Geochemistry at Buranga indicated relatively alkaline-chloride-sulphate carbonate waters and the temperatures inferred from geothermometry were about 120°C with a possible maximum of 150°C (Armannsson, 1994).

In 1999-2003, the International Atomic Energy Agency (IAEA) together with the Ministry of Energy and Mineral Development (MEMD) funded a project called "The Isotope Hydrology for Exploring Geothermal Resources Phase 1" to upgrade and refine the exploration models of Kibiro, Buranga and Katwe-Kikorongo prospects, using isotopes (Kato, 2016).

The German Federal Institute for Geosciences and Natural Resources (BGR), in collaboration with MEMD, undertook preliminary exploration in the Buranga geothermal area starting in 2003. This was part of the GEOTHERM program, which was aimed at promoting the utilization of geothermal energy in developing countries. The project activities included surface water sampling and analysis, isotopic studies, and geophysical surveys (gravity, TEM, and Schlumberger resistivity soundings) (Christopher et al., 2007). Additionally, a micro-earthquake survey was conducted around Buranga to map seismically active structures (Ochmann et al., 2007). The results of these investigations indicated the presence of active Rwenzori bounding faults, which were presumed to control the flow of geothermal fluids. Furthermore, a magma body was inferred to be present beneath the Rwenzori Mountain. The elevated 3He/4He ratios observed in the geothermal fluids from the isotopic and water sampling surveys were believed to be evidence of deep permeability and the possible existence of deep, high-temperature fluid reservoirs (Christopher et al., 2007).

In 2015, M/s GIDDS, a private exploration license holder at Buranga acquired data from 32 MT stations and 38 TEM stations using the expertise of geophysicists from the Geothermal Development Company (GDC) in Kenya. More detailed and infill surveys were recommended at that time in the preliminary data analysis report that was submitted by the license holder to GRD as part of its quarterly activity report (Kato, 2018).

In 2011, the Uganda Geothermal Resources Development Project 1199 fully funded by GoU came on board to undertake appraisal studies on all the geothermal prospects of the country and then come up with a priority ranking of these areas (Kato, 2016). During this project a total of 23 geothermal areas were appraised, Kibiro, Buranga and Panyimur geothermal prospects ranked top. At Buranga, detailed structural geological mapping, geochemical surveys, soil temperature surveys and geophysical surveys were conducted between 2015 to 2019.

This thesis focuses on the processing, analysis and interpretation of the MT and TEM

resistivity data that were collected in Buranga during this period to understand the resistivity structure of the area.

3.1 Early Drilling Campaign

The exploration activities at Buranga Prospect date back to the early 1950s. The first geophysical surveys utilizing gravimetric, magnetometry and electrical resistivity methods were undertaken in April 1953 by L.J. Dyke and J.M. Brown (McConnell & Brown, 1954). According to J.M Brown, a resistivity contour map was produced. Drilling of temperature gradient boreholes began in July 1953 using a percussion rig which was later superseded by a rotary machine in October 1953 (McConnell & Brown, 1954). Four boreholes were drilled, their location is shown in Figure 2.4.

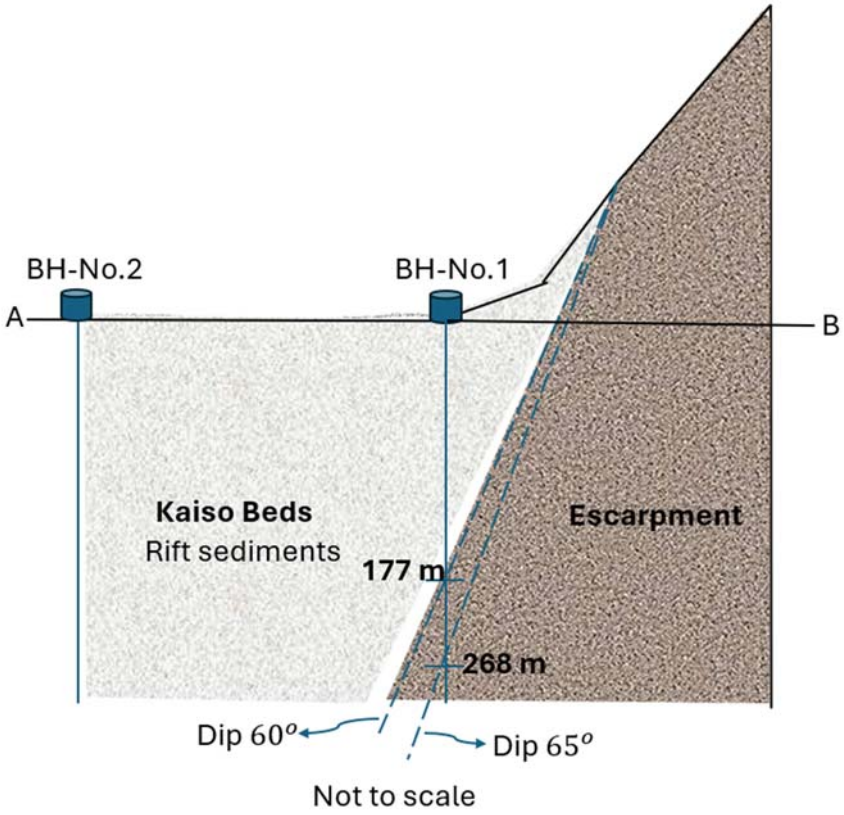

Figure 3.1: Cross-section AB shows the location of drill holes BH-1 and BH-2 and the inferred fault dip of the Bwamba fault. Modified from unpublished reports McConell & Brown, (1954).

Borehole no.1 was drilled to a depth of roughly 180 m with a rotary drill and heavy mud flush. Fault breccia and mylonite like that on the main fault scarp were recovered from the drill core at depths of 172 – 177 m (McConnell & Brown, 1954). From this depth to the bottom of the borehole, granitic rocks are traversed, first appearing as crushed rocks but becoming more solid with increasing depth. The field team at the time believed that the main boundary fault of the Rwenzori massif was cut by the borehole at 172-177 m (Figure 3.1). Moderate permeability was noted between 68.5 m to 110.5 m in the basin fill sediments. The

fault cut by the drill hole would correspond to the range front fault and would have a dip of 60° based on the distance to the surface trace of the fault (Hinz et al., 2017). The highest recorded downhole temperature of 58°C was obtained from the drilling logs of borehole no. 1 at a depth of 173.4 m.

Borehole no. 2 was drilled to a total depth of 394 m in the basin fill sediments and encountered a loss of circulation zone from 186 m to 191 m (Hinz et al., 2017). The returns consisted of sands and boulders with the sands comprising mostly of quartz and a small proportion of feldspar and biotite. A scum of oil was noticed throughout the drilling indicating an oil reservoir underground like those encountered in the northern part of the rift system. Drilling for crude oil is currently underway about 100 km north of Buranga. Borehole no. 3 was drilled to a total depth of 120 m and encountered a loss of circulation at 12.5 m while drilling of borehole no. 4 was started but never completed due to the failure of the drilling equipment.

4 Geothermal Exploration Methods

The goal of geothermal exploration is to facilitate the extraction of hot fluids at depth for power production or direct use. This is achieved by undertaking a series of scientific-based work processes for detecting and delineating exploitable geothermal resources, understanding their characteristics, and constructing a preliminary model of the area coupled with an initial resource assessment to guide the siting of wells. Due to the complexity of the subsurface systems, effective exploration methods are crucial for successful geothermal development. The complexity of geothermal subsurface systems, therefore, necessitates a multidisciplinary approach where geology, geochemistry, geophysics, and other remote sensing techniques complement each other (Huenges & Ledru, 2011)

4.1 Structural and Geological Mapping

In a greenfield geothermal area like Buranga, geological mapping is the first step of exploration obtaining crucial information about the surface features of the area. In geological surveys, geothermal manifestations, rock types, and geological structures such as faults, fractures and joints are mapped (Faulds et al., 2006).

Although this method is limited to mainly surface observations which might not give very precise subsurface information, reservoir physical parameters and arrangement, it is usually of immense importance when used jointly with other geoscientific results to help join the dots in understanding the intricate nature of the subsurface.

The deliverables from a typical geological mapping campaign are usually maps, cross-sections, and sometimes an initial geological model of the area. The geological model together with resistivity and shallow temperature gradient drilling data usually indicate the inferred up-flow and outflow zones, the heat source and estimated depth to the reservoir, and main controlling structures such as fractures and faults as well as the lithologic units. Geological models are very preliminary when it comes to subsurface conditions, but they

provide vital surface information that is used later for integrated conceptual modelling of the area.

4.2 Geochemical Surveys

Geochemical surveys are usually undertaken to understand the chemical composition of the fluids at the surface and then infer the interactions and chemical processes that have taken place at depth. Therefore, in the presence of hot spring fluids and fluids from fumaroles, geochemical methods are used to estimate the reservoir temperature using chemical, gas, and water geothermometers. Geochemistry plays a crucial role in informing us about reservoir properties such as salinity, fluid equilibrium state, fluid origin, fluid flow directions, source of recharge, etc. Therefore, integrating geochemical data with other geoscientific data sets such as structural mapping data, soil temperature survey data and remote sensing (Bahati et al., 2005) can provide insights into field extent as well as help in siting of drilling targets.

4.3 Soil Temperature Surveys

Soil temperature survey is usually deployed together with gas flux measurements during the initial stages of geothermal exploration. This involves the collection of surface temperature data by using thermistor rods pushed about 50 cm -100 cm into the soil and then measuring the temperature at those depths (Olmsted & Ingebritsen, 1986), (Zehner et al., 2012). Soil gas flux on the other hand measures the upflow of gases usually CO_2, H_2S and Radon (Harvey & Harvey, 2015), (Klusman et al., 2000) in areas with notable fractures. These methods are useful in delineating areas of elevated heat and mass transfer in areas with wide fracture zones and faults. However, in blind and heavily capped systems, soil gas flux and shallow temperature measurements can be rather misleading.

4.4 Geophysical Methods

Geological and geochemical mapping are primarily based on direct observations made at the Earth's surface. From these surface-level data, we can conclude and make extrapolations about the underlying subsurface structures and systems. In contrast, geophysical surface exploration methods measure the surface signatures that are indicative of properties and processes occurring at depth (Hersir et al., 2022).

Within the geoscientific exploration industry, various geophysical exploration techniques are classified into several groups including seismic methods, electrical resistivity methods, potential methods (gravity and magnetics), heat flow measurements, and surface deformation measurements.

Geophysical methods are classified into those that are directly related to the parameters that are diagnostic to and characterize the reservoir (direct methods) and those that are indirectly related to the reservoir, known as the structural or indirect methods.

During exploration stages, geophysical surveys are used to outline the size of the geothermal

area, locate the geothermal reservoir, estimate the depth of the reservoir, inform us about reservoir parameters such as permeability, locate the heat source, the up flow, outflow and recharge zone, location of the clay cap and the nature of reservoir rocks and finally help us to site wells.

Additionally, there are some geophysical methods used to monitor reservoir behaviour when geothermal fields are being utilized. Microgravity, ground/surface deformation and micro-seismicity techniques provide information on reservoir behaviour, such as subsidence and uplift from mass extraction and reinjection (Heimlich et al., 2015) over time, reinjection triggered micro seismicity and fault-related permeability from hypocenter distribution analysis or simple shear dilation – permeability enhancement relationships, consequently enabling the development of better production and reinjection strategies to improve sustainable utilization (Bromley, 2018).

4.4.1 Indirect (structural) Methods

These methods focus on detecting parameters that are associated with geological formations or structures. These methods include:

Gravity methods - These are methods in which the spatial variations of gravitational acceleration are measured. The data undergo a series of corrections to produce a Bouguer gravity map which shows the variations of the density in the subsurface at the survey area. The density contrast is correlated with geological information to delineate features such as faults, dense intrusions, or sediments in a dense basement (Hersir et al., 2022).

Additionally, gravity and surface deformation measurements are very important during the lifetime of the geothermal power plant as they can be used as a monitoring tool to investigate the net total fluid withdrawal from the reservoir as well as investigate the presence of vapour or steam caps in high enthalpy geothermal systems (Hersir et al., 2022).

Magnetic surveys – Magnetic surveys measure the spatial variations in the local strength of the Earth's magnetic field. Anomalous magnetic variations are associated with the composition and structure of the rock assemblages in the subsurface. The physical parameter of interest in magnetic prospecting is the magnetic susceptibility of the rocks which influences the natural magnetic field in the survey area (Huenges & Ledru, 2011). Magnetic surveys can be airborne for regional exploration or

surface-based in the case of localized geothermal exploration (Hersir et al., 2022). More recently, drones have been used for magnetic surveying.

In geothermally active areas, the high-temperature alteration processes lead to a reduction in the magnetic susceptibility of the rocks. The alteration processes are linked to high-temperature fluids related to a geothermal reservoir and other conduit structures such as faults, dykes, and fissures. Magnetic lows are, therefore, seen in areas of geothermal activity compared to the surrounding areas where there is no hydrothermal alteration and activity.

Rocks acquire magnetization during formation and this magnetization reflects the orientation and strength of the magnetic field at the time of rock formation (solidification). However, rocks can lose their magnetic properties over time if they are exposed to temperatures above Curie temperature (Huenges & Ledru, 2011), i.e., the temperature above which magnetic minerals lose their magnetization. Ferromagnetic minerals have varying Curie temperatures, but two of the most common strongly magnetic minerals magnetite and pyrrhotine, have Curie temperatures of 580ºC and 320ºC, respectively (Didas et al., 2022); (Huenges & Ledru, 2011).

Magnetic surveys play an important role in geothermal exploration as they can be used to detect the depth at which the Curie temperature is reached, locate dykes, hydrothermally altered areas, fissures and buried lavas (Didas et al., 2022; Hersir et al., 2022)

4.4.2 Direct Methods

Here the variations in the physical properties are directly related to the geothermal resource, for example.

- Resistivity surveys - resistivity is related to key geothermal parameters such as pore structure and porosity, water saturation, salinity, hydrothermal alteration, and temperature. Resistivity methods are discussed in detail in the following chapter.
- Temperature measurements - these are used to determine the temperature gradient and the total heat flow in an area. They are usually done in shallow boreholes or temperature gradient holes, commonly to locate the upflow. Heat transfer within the earth's subsurface occurs through three major processes, i.e. Conduction, where heat transfer is through the vibration of atoms, Convection, in which there is buoyancy-driven heat transfer and radiation. Radiation doesn't influence geothermal systems (Georgsson, 2009).

5 Theory of Resistivity Methods

5.1 Resistivity of rocks

Understanding the fundamentals of resistivity of rocks is a key aspect of resistivity surveying for geothermal resource exploration. A well-detailed account of these fundamentals is provided by (Hersir et al., 2022) and references therein. A brief discussion is given here.

According to Ohm´s law, the electrical field, **E** (V/m) at a particular point in a material is proportional to the current density, **j** (A/m^2)

$$\mathbf{E} = \rho\mathbf{j} \tag{5.1}$$

The proportionality constant, ρ, depends on the type of material and is called the (specific) resistivity whose unit is Ωm. The reciprocal of resistivity is conductivity. Electrical conduction in materials takes place by the movement of electrons and ions (Figure 5.1). Conductivity in rocks is mostly through pore fluid conduction and surface conduction by dissolved ions in the fluid and on the pore surface. Surface conduction is a result of highly mobile ions on the boundary between the pore fluid and the pore wall. The ability to form a

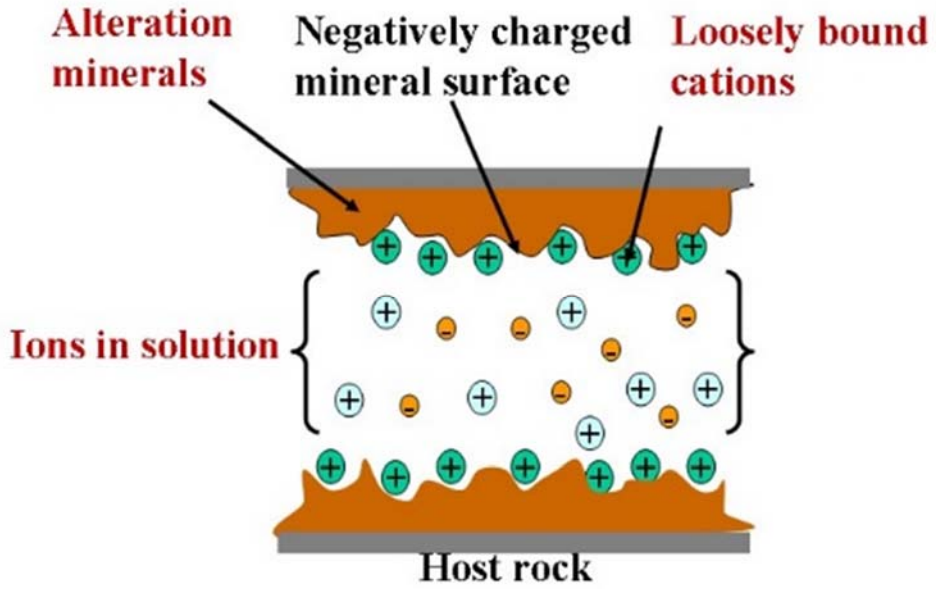

Figure 5.1: Conduction mechanisms in rocks (Hersir & Arnason, 2009)

conductive layer along the pore walls varies from mineral to mineral depending on the cation exchange capacity (CEC) (Hersir et al., 2022). Mineral conduction is negligible in most cases since the rock matrix, which is the non-porous part of the rock, is normally an insulator except at very high temperatures when the rock matrix conductivity becomes significant.

The resistivity of rocks is influenced by many factors. The most important ones are:

a) **Porosity and pore structure of the rock**

The porosity of a material is defined as the ratio of the pore volume to the total volume of the rock.

$$\varphi_t = \frac{V_\varphi}{V} \quad (5.2)$$

Where, φ_t= Fractional porosity

V_φ = Volume of pores and

V = Total volume of the rock

The degree of saturation and porosity are of great importance to the bulk resistivity of the rock. Archie's law (Archie, 1942) asserts that resistivity decreases with increasing porosity of the host rock when fluid conduction dominates other conduction mechanisms in the rock. Generally, the resistivity of the bulk rock is a function of the resistivity of the rock matrix and the resistivity of the pore fluid.

$$\rho = \frac{\rho_w a}{\emptyset_t^n} \quad (5.3)$$

Where $\emptyset$ = Porosity in proportions of total volume (0-1).

ρ_w = Resistivity of the pore fluid (Ωm).

ρ = Bulk resistivity (Ωm).

a = Parameter describing porosity ≅ 1 and

n = Cementing factor ≅ 2.

b) The temperature of pore fluids

At moderate temperatures (0 – 200°C), an increase in temperature corresponds to a decrease in the resistivity of aqueous solutions due to the increase of mobility of ions caused by a reduction in viscosity of the water. This relationship has been described in (Dakhnov, 1962) and is shown in Equation (5).

$$\rho_w = \frac{\rho_{wo}}{1+\alpha(T-T_o)} \quad (5.4)$$

Where, ρ_{wo}= Resistivity of fluid at reference temperature T_0

ρ_w = Resistivity of the fluid at temperature T (Ωm)

α = Temperature coefficient of resistivity (°C) α ≅ 0.023 $°C^{-1}$ for T_0 =25°C

T = Temperature (°C)

T_0 = Reference temperature

However, at temperatures exceeding 250°C, increasing temperature increases the resistivity of the fluid due to the decrease in the dielectric permittivity of water resulting in a decrease

in the number of dissociated ions in the solution. Figure 5.2 shows how the resistivity decreases with increasing temperature.

c) Salinity of fluids

Resistivity and salinity of pore fluids have an inverse proportionality relationship as described by (Keller & Frischknecht, 1966).

$$\text{Resistivity, } \rho \approx 10/\text{Concentration}$$

Ions are dissolved and are mobile in an aqueous salt-solution. In the presence of an electric field, the cations and anions are accelerated to the electrode and cathode, respectively. The

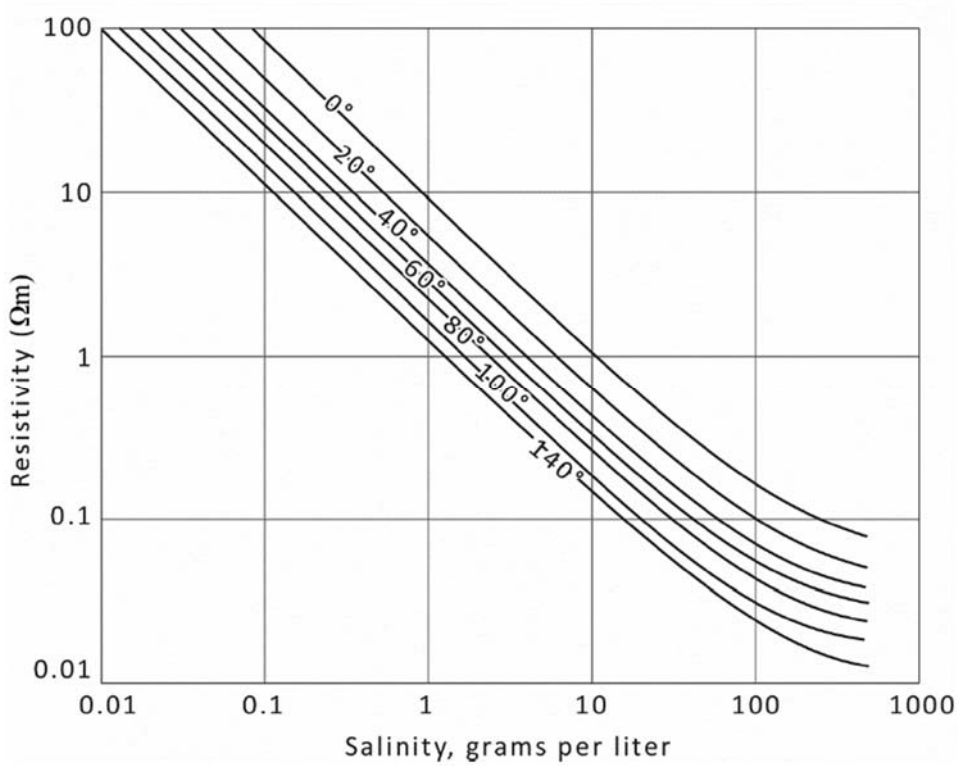

Figure 5.2: Plot of resistivity of solutions of NaCl as a function of temperature and concentration of ions in solutions. Adopted from Hersir et al. (2022); Keller & Frischknecht, (1966).

mobility of these ions is dependent on the temperature and concentration of the ions in the solution. A plot (Figure 5.2) of the resistivity of solutions of sodium chloride (NaCl) with respect to temperature and concentration shows a nearly linear relationship between conductivity and salinity except at very high salinities (Keller & Frischknecht, 1966).

d) Water rock interaction and alteration

In the presence of water and sufficiently high temperature, rocks undergo hydrothermal alteration and subsequently give rise to the production of alteration minerals that are characteristic of the formation temperature at that time. These minerals (Figure 5.3) provide us with information about the flow paths of the geothermal water as well as the temperature as the alteration was formed. Although alteration starts at around 50°C, it becomes pronounced as temperatures approach 100°C with the formation of low-temperature smectite

clay minerals making the rocks conductive due to the high CEC of smectite (Hersir & Arnason, 2009). This is referred to as the smectite zone.

At high temperatures, ranging between 220-240°C, smectite and zeolites are slowly turned into chlorite as the dominant alteration mineralogy in the mixed layered clay zone (Kristmannsdóttir, 1979), (Hersir & Arnason, 2009) and the resistivity increases again as their CEC decreases. At still higher temperatures (260-270°C), epidotes dominate in the chlorite-epidote zone. This type of zoning is mostly applicable to freshwater basaltic systems. In brine systems, a similar zoning exists although the mixed-layer clay zone covers a broader temperature range of about 250-300°C (Kahwa, 2012).

In Silicic areas where silicic rocks such as rhyolite or dacite are predominant, the formation temperatures are estimated to be in the range of 160°C-270°C (Ylagan et al., 1996). The interaction between the hot fluids and the primary silicic mineral in the rocks leads to the formation of distinct alteration mineral assemblages such as sericite, kaolinites, and various clay minerals.

In low-temperature geothermal systems, at < 150°C, the common alteration mineral is the smectite clay which is present in the smectite-zeolite zone.

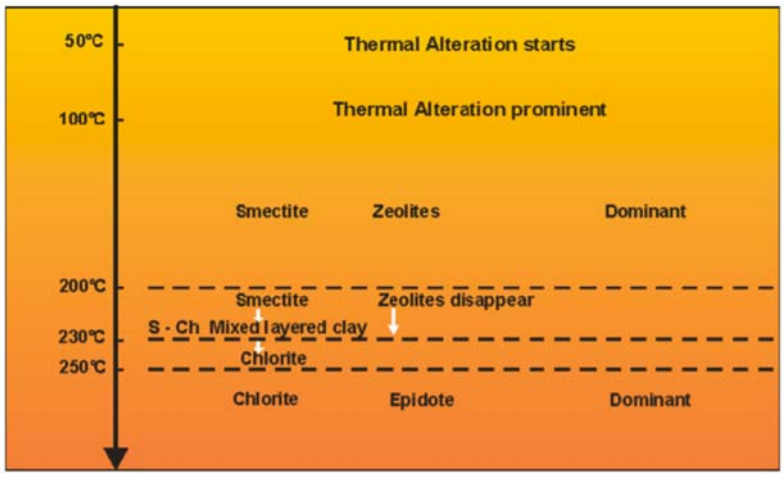

Figure 5.3: Alteration temperatures and mineralogy (Hersir & Arnason, 2009)

At Buranga geothermal area, the system is thought of as a low-temperature geothermal area. Therefore, the dominant alteration regime might take place at 150-180 °C giving rise to highly conductive smectite alteration minerals that usually form the reservoir caprock. Previous 1D resistivity studies did not show the presence of high-temperature alteration mineralogy (Ssemuyaba et al., 2023). It is important to note that sometimes the alteration of mineralogy might indicate a fossil geothermal system (rock temperature is lower than the formation temperature). The system has cooled down over time where the inferred alteration temperatures do not match the present temperatures.

5.2 Transient Electromagnetics

Before the advancement and global boom of the TEM method, resistivity surveys were undertaken by direct current (DC) resistivity methods. The downside of conventional DC resistivity methods is the difficulty encountered when trying to inject current in volcanic areas where the surface is usually covered with dry lava and in areas that are very rocky and mountainous. Over the last three decades, TEM surveys have increasingly been applied in geothermal exploration because data collection is much cheaper and quicker since no current needs to be injected into the ground opposite to conventional DC resistivity methods.

When modelling geophysical data, the structure of the Earth can be assumed to vary in one, two or three dimensions. In a one-dimensional (1D) approach, the resistivity of the Earth is assumed to vary only with depth. For a two-dimensional (2D) approach, the resistivity distribution varies both vertically and laterally in one of the two principal directions. In the three-dimensional approach (3D) the resistivity distribution is considered to vary vertically and in both lateral dimensions (Árnason, 1989; Chave & Jones, 2012).

The TEM central loop method is less sensitive to lateral resistivity variations than DC resistivity methods (Árnason, 1989) but sufficiently sensitive to vertical resistivity variations making one-dimensional inversion justifiable. The low sensitivity of TEM to lateral resistivity variations is a result of the induced current rings diffusing downwards and outwards at late times.

TEM is categorized as an active geophysical method. In this approach, a direct current from a transmitter is fed into a transmitter loop of wire laid on the ground and then this current is abruptly turned off and on in succession. By Faraday's law, once the current in the transmitting loop is turned off, a nearly identical current is induced in the subsurface to preserve the magnetic field produced by the original current. Due to ohmic losses, these induced currents decay, causing a change in the magnetic field which subsequently induces new eddy currents below (Figure 5.4).

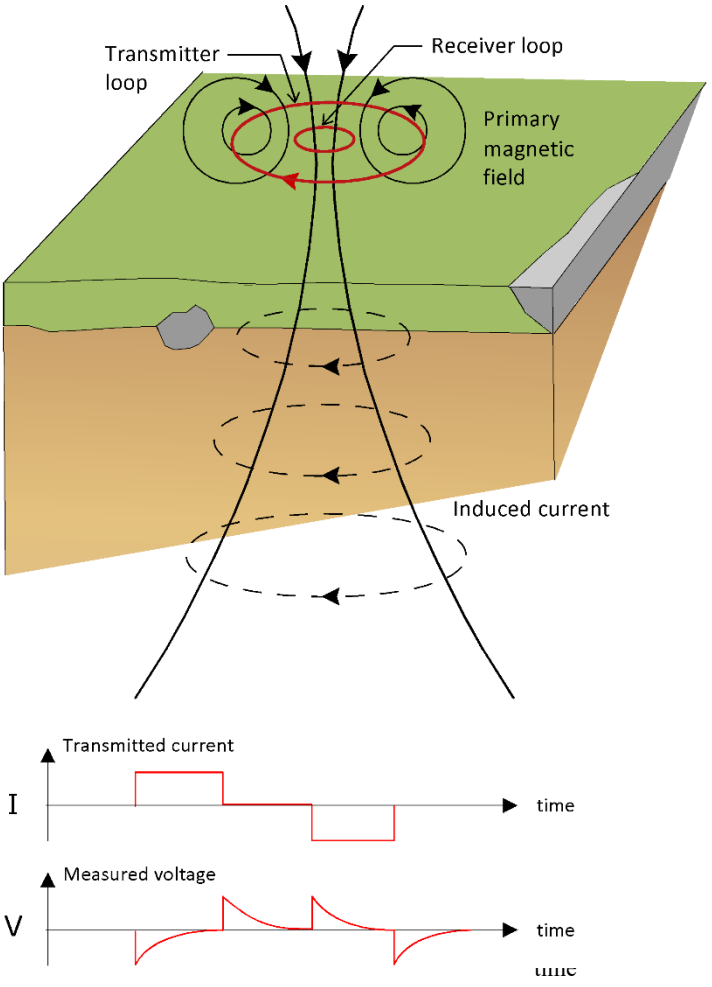

Figure 5.4: TEM setup and propagation of induced currents in the ground (Hersir et al., 2022)

This results in a downward and outward diffusion of currents in the subsurface (Figure 5.4). The receiver coil then measures the voltage decay at different time gates after the transmitted current is turned off. The decay rate of the measured secondary magnetic field depends on the resistivity structure of the earth. TEM surveys allow for probing of the subsurface to almost one

kilometer. However, the actual depth of penetration is dependent on how long the induction in the receiver coil can be traced before it is obscured by noise (Árnason, 1989). Depth of penetration also depends on the resistivity structure of the area as well as the transmitter loop size and the transmitted current.

At "late times" after the current is switched off, the induced voltage in the receiver loop in a homogeneous half-space is given by Equation (5.5);

$$V(t,r) = I_o \left(\frac{C(\mu_o \sigma r^2)^{3/2}}{10\pi^{1/2} t^{5/2}}\right) \tag{5.5}$$

When the current is switched off, at late times the voltage is proportional to $\sigma^{3/2}$ and falls off with time as $t^{-5/2}$. The apparent resistivity $\rho_a(r,t)$, which is described as the resistivity of homogeneous earth that would give the measured voltage for a specific geometry can then be calculated using Equation (5.6)

$$\rho_a(r,t) = \frac{\mu_0}{4\pi}\left|\frac{2\mu_0 I A_r n_r A_s n_s}{5t^{5/2} V(r,t)}\right|^{2/3} \tag{5.6}$$

Where,

$$C = A_r n_r A_s n_s \frac{\mu_o}{2\pi r^3}$$

A_r = Cross-sectional area of the receiver coil [m^2].
A_s = Cross-sectional area of the transmitter loop [m^2].
n_r = Number of windings in the receiver coil.
n_s = Number of windings in the transmitter loop.
V = The voltage response [V], the induced voltage at time t.
μ_o = Magnetic Permeability in vacuum [H/m].

σ = Conductivity.
I = Current strength [A].
t = Current Decay Time [s]
r = Radius of the transmitter loop [m]

If we plot the transient response for a uniform half-space with resistivities 1, 10 and 100 Ωm and r=100 m versus time according to Equation 5.6, then the apparent resistivity approaches the true resistivity of the half-space at later times as the resistivity is lower (Figure 5.5)

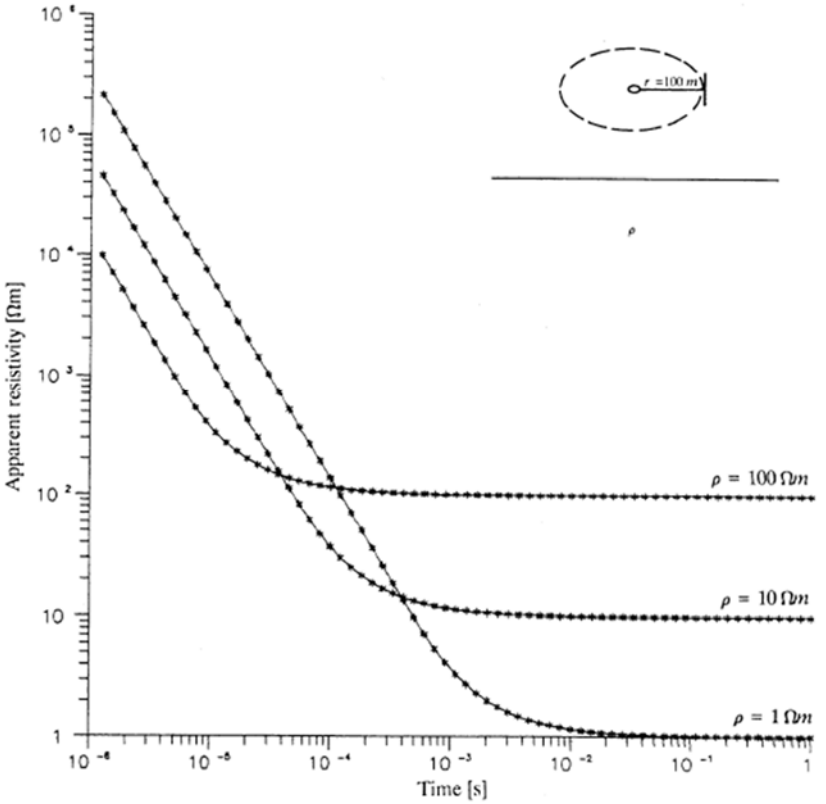

Figure 5.5: Late time apparent resistivity for a homogeneous half-space. Adopted from (Árnason, 1989)

In TEM measurements, the transmitter couples inductively to the earth such that no current has to be injected into the ground making TEM more advantageous over other conventional non-passive resistivity methods, less problems with a high resistive surface. TEM has been preferred over MT and DC methods in areas where the surface conductivity is high since signals from the MT and DC methods tend to stay within the conductive layers hence screening the resistive layers below. TEM has a high signal in low resistivity areas at the near-surface.

Contrary to DC methods and MT, TEM suffers minimal distortions due to shallow subsurface resistivity inhomogeneities since the late time signals are little affected by near-surface variations (see discussion of "static shifts" in Chapter 5.4.4).

The main noise sources in TEM soundings are cultural noise such as power lines and buried cables.

5.3 Magnetotelluric method

5.3.1 MT Overview and EM Theory

The geophysical community credits the initial work on the theory of Magnetotellurics (MT) to Tikhonov (1950) in the USSR, Cagniard (1953) in France, and Kato, Kikuchi and Rikitake (1950) in Japan. It is worth mentioning that the development and improvements in MT are the cumulative result of research by several academicians and practitioners over the first half of the twentieth century.

The MT method has undergone a series of fundamental changes and development, especially over the last three decades mainly due to the four major factors as highlighted in (Chave & Jones, 2012).

(i) The development of fast and reliable two and three-dimensional modelling and inversion algorithms (codes) that are tenable due to the ever-increasing computing power and speed of modern machines (computers).
(ii) Improvement in the understanding and handling of noise in electromagnetic measurements is achievable through the evolution of data processing algorithms.
(iii) The emergence of low-power, low-cost digital electromagnetic sensing and recording technologies.
(iv) Advances in the ability to recognise and remove/reduce errors due to near-surface resistivity inhomogeneities close to the sounding site.

The MT method is characterized as a passive geophysical technique that utilizes the natural variations in the Earth's magnetic and electric fields with the micro pulsations and the sferics being the signal source (Hersir et al., 2022). The time variations of the earth's electric and magnetic fields at a site are recorded in orthogonal directions simultaneously over a wide range of frequencies and analyzed to obtain their spectra and apparent resistivity of the subsurface as a function of frequency. The data are then inverted to infer the resistivity structure below the measurement site on depth scales ranging from a few tens of meters to tens of kilometres. The periodicity of the source signals as well as the resistivity structure of the subsurface determine the depth of the information retrieved. This is based on the electromagnetic skin depth which describes the exponential decay of electromagnetic waves as they diffuse into a medium (Didana, 2010). The skin depth (δ) is the depth where the EM fields have attenuated to a value of e^{-1} (about 0.37) of their surface amplitude (Hersir et al., 2022), and is given by,

$$\delta(T) = 500\sqrt{T\rho} \qquad (5.7)$$

Where, $\delta(T)$= Skin depth in m
T= Period (s)
ρ= Average resistivity of the subsurface down to that depth

Source of Signal

The Earth's time-varying magnetic field is generated by two sources which strongly differ in amplitude and in their time-dependent behaviour. MT generally refers to recording time series of electric and magnetic fields of wavelengths from around

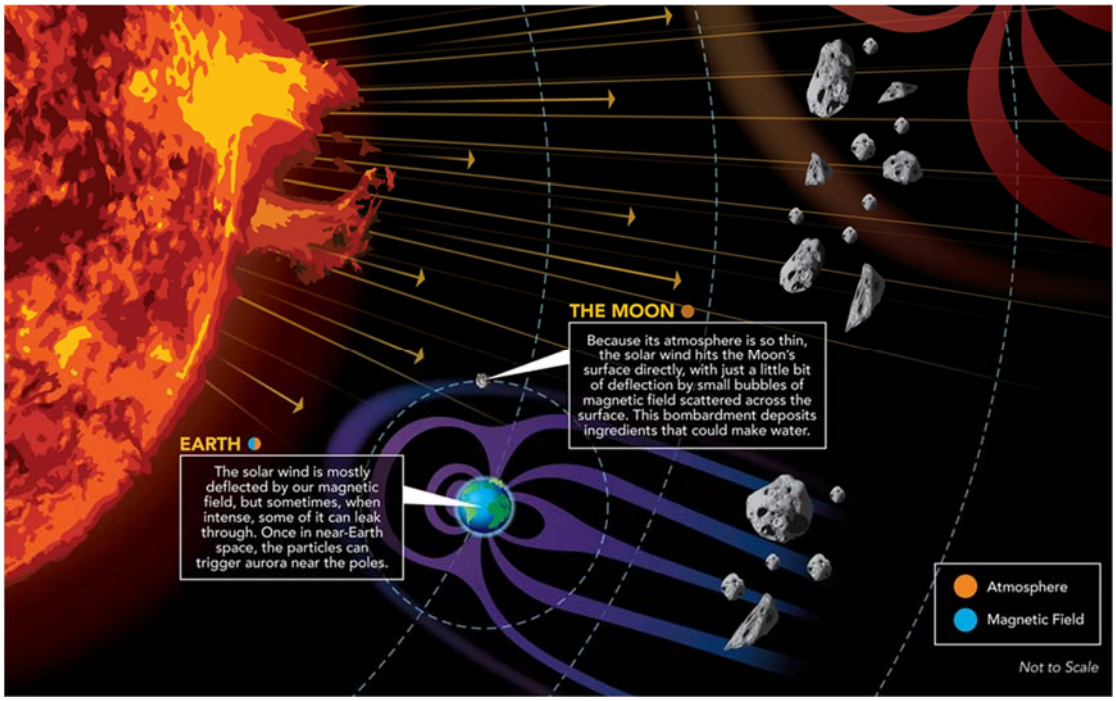

Figure 5.6: Interaction of the solar wind with different celestial bodies. The solar wind is mostly deflected by the earth's magnetic field but when sufficiently intense, it leaks through and once near earth space the particles can trigger auroras near the poles. Courtsey (NASA, 2023; Ssemuyaba et al., 2023)

0.0025 s (400 Hz) to 1000 s (0.001 Hz) (Figure 5.7) and these are of special interest as they induce eddy currents and secondary magnetic fields in the earth due to their transient nature. The small geomagnetic time variations that fall on a wide spectrum are generated by two different sources (Hersir et al., 2022). Low frequencies (< 1 Hz) are generated by the ionospheric and magnetospheric interactions with the solar wind (plasma) being emitted from the sun. The solar wind is a continuous stream of plasma carrying a weak magnetic field. The constant pressure of the solar wind onto the magnetosphere causes compressions on the sun-directed side and a tail on the night side (Figure 5.6). Because of the variations in the strength, density and velocity of the solar wind, the Earth's magnetosphere is subject to varying distortions and changes in the magnetic field.

On the sun-directed side of the Earth, ionization of air molecules takes place in the ionosphere due to soft X-rays and ultraviolet light. Solar heat induces thermal convection of the ionized air molecules and thus establishes large-scale electric currents acting as magnetic field sources (Thiel, 2008).

The higher frequencies (>1 Hz) are generated because of thunderstorm activity near the equator and distributed as guided waves (the so-called sferics) between the ionosphere and the ground surface to regions of higher latitudes.

Between 0.5-5 Hz lies a region (Figure 5.7) in which the natural electromagnetic fluctuations have low intensity/amplitude and thus affect MT measurements made in this frequency range, commonly called the MT dead band. The data from this frequency range are usually of poor quality. MT signals are generally of slightly poor quality and

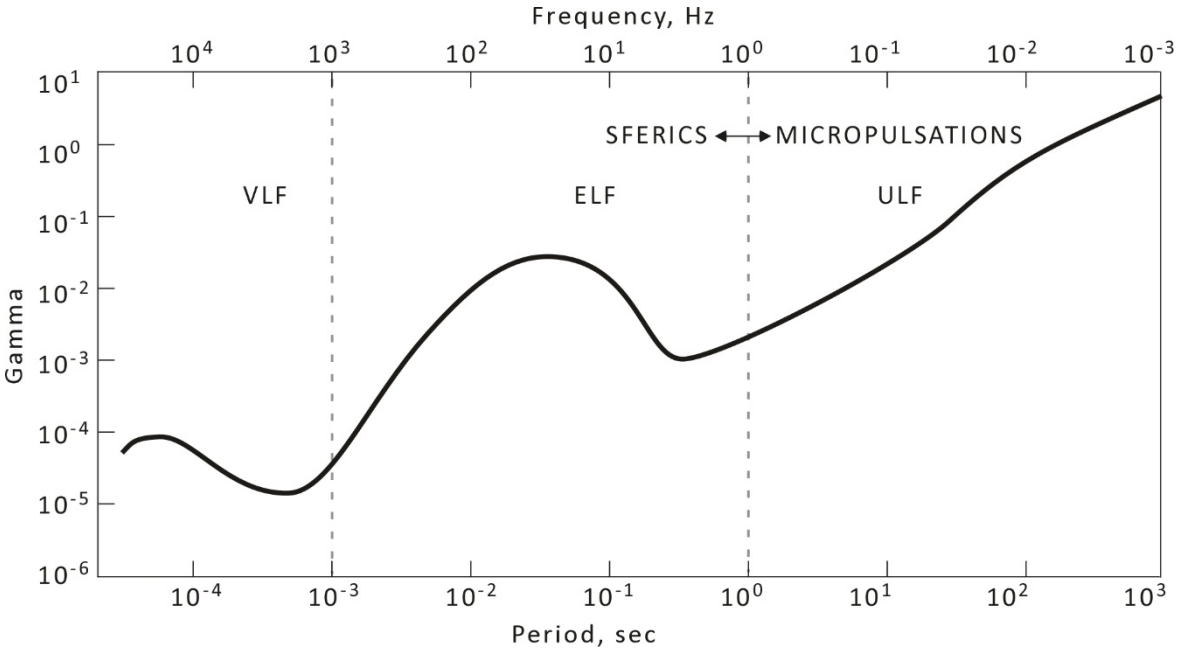

Figure 5.7: Strength of the natural magnetic field spectrum in gamma (γ=nT) against frequency (and period). The MT dead band is in the range ≈ 0.5-5 Hz while the AMT dead band is in the range ≈ 1-5 kHz. (Hersir et al., 2022; Keller & Frischknecht, 1966)

sometimes noisy near the equator compared to data in polar regions although the harsh conditions in the latter present their unique challenges (Hill, 2020). At higher frequency there is another dead band at 1-5 kHz, the AMT dead band.

5.3.2 Propagation of EM fields in the Earth

To understand the behaviour of EM fields for a polarizable and magnetizable medium having no electric and magnetic sources, we shall employ four relations collectively known as Maxwell's equations which are said to hold at all times under the above conditions for all frequencies (Thiel, 2008). These equations are said to be covariant under the Lorentz transformations (Chave & Jones, 2012)

$$\nabla \times \vec{E} = -\frac{\partial \vec{B}}{\partial t} \text{ Faraday's Law} \quad (5.8a)$$

$$\nabla \times \vec{H} = \vec{j} + \frac{\overrightarrow{\partial D}}{\partial t} \text{ Ampere's Law} \quad (5.8b)$$

$$\vec{\nabla} \cdot \vec{B} = 0 \text{ Gauss's Law for Magnetism} \quad (5.8c)$$

$$\vec{\nabla} \cdot \vec{D} = \eta \text{ Gauss's Law} \quad (5.8d)$$

Where, $\vec{\boldsymbol{B}}$ is the induced magnetic field (in T), $\vec{\boldsymbol{D}}$ is the electric displacement field (in C/m^2), $\vec{\boldsymbol{H}}$ is the magnetic field strength (in A/m), $\vec{\boldsymbol{j}}$ is the current density (in A/m^2), **E** is the electric field (in V/m), $\boldsymbol{\eta}$ is the electric charge density (in C/m^3). Faraday's law (5.8a) states that circulating electric fields in a closed loop are a result of time-varying magnetic fields (Figure 5.9b) whereas Ampere's law (5.8b) states that circulating magnetic fields are produced by the vector sum of electric currents and time-varying electric fields (Figure 5.9a).

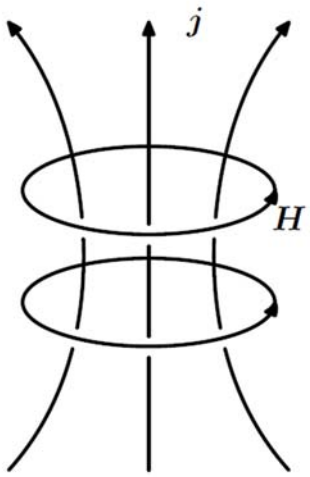

Figure 5.9a: Representation of Ampere's Law (Thiel, 2008)

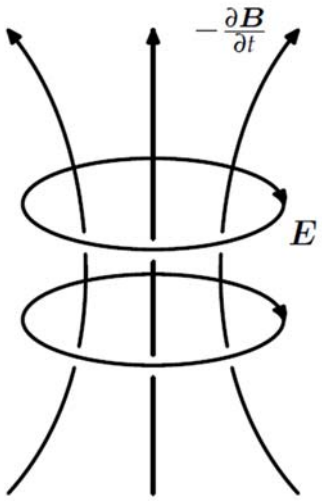

Figure 5.9b: Representation of Faraday's Law (Thiel, 2008)

If we introduce a linear isotropic medium, then the material equations can be incorporated to create for the intrinsic properties of the material, (these are better known as the constitutive relationships).

$$\vec{B} = \mu\vec{H} \tag{5.9a}$$

$$\vec{D} = \varepsilon\vec{E} \tag{5.9b}$$

$$\vec{j} = \sigma\vec{E} \tag{5.9c}$$

Where $\mu = \mu_0\mu_r$ is the magnetic permeability of the material, μ_r is the relative permeability of the material and indicates the permeability of the material relative to the vacuum (free space). If μ_r =1, then its permeability is equal to vacuum. $\varepsilon = \varepsilon_o\varepsilon_r$ is the dielectric permittivity of the material, ε_r is the relative permittivity of the material which indicates the permittivity of the material relative to vacuum (free space). σ = electric conductivity (S/m).

$\mu_0 = 4\pi \cdot 10^{-7}$ H/m (Magnetic permeability of free space)

$\varepsilon_o = 8.85 \cdot 10^{-12}$ F/m (Dielectric permittivity of free space)

On the spatial scales relevant to MT surveys, except within certain types of ore bodies, the Earth's materials are generally not magnetizable. As a result, the magnetic permeability of the subsurface can be approximated as that of free space μ_0.

Using the intrinsic relationships above, and assuming harmonic dependency of the fields, i.e., $e^{-i\omega t}$, where ω is the angular frequency, then we can rewrite Faraday's and Ampere's equations as;

$$\nabla \times \boldsymbol{E} = -\mu \frac{\partial \boldsymbol{H}}{\partial t} = i\omega\mu \boldsymbol{H} \tag{5.10a}$$

$$\nabla \times \boldsymbol{H} = \sigma \boldsymbol{E} + \varepsilon \frac{\partial \boldsymbol{E}}{\partial t} = (\sigma - i\omega\varepsilon)\boldsymbol{E} \tag{5.10b}$$

In a homogeneous medium, the electric charge density is zero and therefore, Gauss's law reduces to

$$\nabla \cdot \boldsymbol{E} = 0 \tag{5.10c}$$

If we take the time derivative of Equation (5.10b) we obtain,

$$\nabla \times \frac{\partial \boldsymbol{H}}{\partial t} = \sigma \frac{\partial \boldsymbol{E}}{\partial t} + \varepsilon \frac{\partial^2 \boldsymbol{E}}{\partial^2 t}$$

Using Equation 5.10a and substituting for H in the equation above we obtain

$$-\nabla \times (\nabla \times \boldsymbol{E}) = \sigma \mu \frac{\partial \boldsymbol{E}}{\partial t} + \varepsilon \mu \frac{\partial^2 \boldsymbol{E}}{\partial^2 t} \tag{5.10d}$$

If we use the vector identity $\nabla \times (\nabla \times A) = -\nabla^2 \mathrm{A} + \nabla \cdot (\nabla \cdot A)$ and considering that $\vec{\nabla} \cdot \vec{E} = 0$, then Equation (5.10d) can be rewritten as.

$$\nabla^2 \mathbf{E} = \mu\sigma \frac{\partial \boldsymbol{E}}{\partial t} + \mu\varepsilon \frac{\partial^2 \boldsymbol{E}}{\partial t^2} \tag{5.10e}$$

Performing the same operations on Equations (5.8a) and (5.8b) we obtain

$$\nabla^2 \mathbf{H} = \mu\sigma \frac{\partial \boldsymbol{H}}{\partial t} + \mu\varepsilon \frac{\partial^2 \boldsymbol{H}}{\partial t^2} \tag{5.10f}$$

In materials with zero conductivity, such as insulators, Equations (5.10e) and (5.10f) can be rewritten to represent non-diffusive wave equations. These equations describe the nature of electromagnetic wave propagation in a non-conductive medium, where the waves propagate with a specific velocity $v = \frac{1}{\sqrt{\varepsilon\mu}}$. Both these equations are frequency-dependent.

$$\nabla^2 \mathbf{E} - \mu\varepsilon \frac{\partial^2 \boldsymbol{E}}{\partial t^2} = 0 \tag{5.11}$$

$$\nabla^2 \mathbf{H} - \mu\varepsilon \frac{\partial^2 \boldsymbol{H}}{\partial t^2} = 0 \tag{5.12}$$

For harmonically dependent fields, Equations (5.10e) and (5.10f) can be written as

$$\nabla^2\mathbf{E} + i\omega\mu\sigma\boldsymbol{E} + \omega^2\mu\varepsilon\boldsymbol{E} = 0 \qquad (5.13a)$$

$$\nabla^2\mathbf{H} + i\omega\mu\sigma\boldsymbol{H} + \omega^2\mu\varepsilon\boldsymbol{H} = 0 \qquad (5.13b)$$

Equations (5.13a) and (5.13b) are in the Helmholtz differential equation form $\boldsymbol{\nabla^2\mathbf{F} + k^2F = 0}$ where k is the propagation constant (wave number) in the medium given by;

$$k^2 = i\omega\mu\sigma + \omega^2\mu\varepsilon \qquad (5.14a)$$

For quasi-stationary (diffusive) electromagnetic field behaviour, we assume that the EM field varies slowly over time compared to the time of the measurements such that the displacement currents are negligible compared to the conduction currents over the MT frequency range (Tezkan, 1999). This implies that $\omega\mu\sigma \gg \omega^2\mu\varepsilon$ and therefore,

$$k^2 = i\omega\mu\sigma \qquad (5.14b)$$

The Helmholtz differential equations for (5.13a) and (5.13b) are in the form.

$\boldsymbol{\nabla^2\mathbf{E} + k^2E = 0}$ $\boldsymbol{\nabla^2\mathbf{H} + k^2H = 0}$ and have wave solutions represented as;

$$\boldsymbol{E}(x,t) = \boldsymbol{E}^+e^{-i(kx-\omega t)} + \boldsymbol{E}^-e^{-i(kx+\omega t)} \qquad (5.15a)$$

$$\boldsymbol{H}(x,t) = \boldsymbol{H}^+e^{-i(kx-\omega t)} + \boldsymbol{H}^-e^{-i(kx+\omega t)} \qquad (5.15b)$$

$\boldsymbol{E^+, E^-, H^+ and\ H^-}$ are general complex arbitrary constants determined by examining the exponential terms (e^{-ikx}) and (e^{ikx}) $\boldsymbol{k = ku}$ represents the propagation vector whereas **u** is normal to the planes of constant phase. The first terms in equations (5.15a) and (5.15b) represent the wave moving in the direction of **u** and the second term represents a wave moving opposite to **u**. (Lichoro et al., 2017).

If we take a plane EM wave with angular frequency ω incident at an angle θ_i at the surface of a homogeneous earth with resistivity $\rho = \frac{1}{\sigma}$. Part of the wave propagates through the half-space at a refracted angle of θ_t and another can be reflected at the air-earth interface through an angle θ_r schematically represented in Figure 5.10.

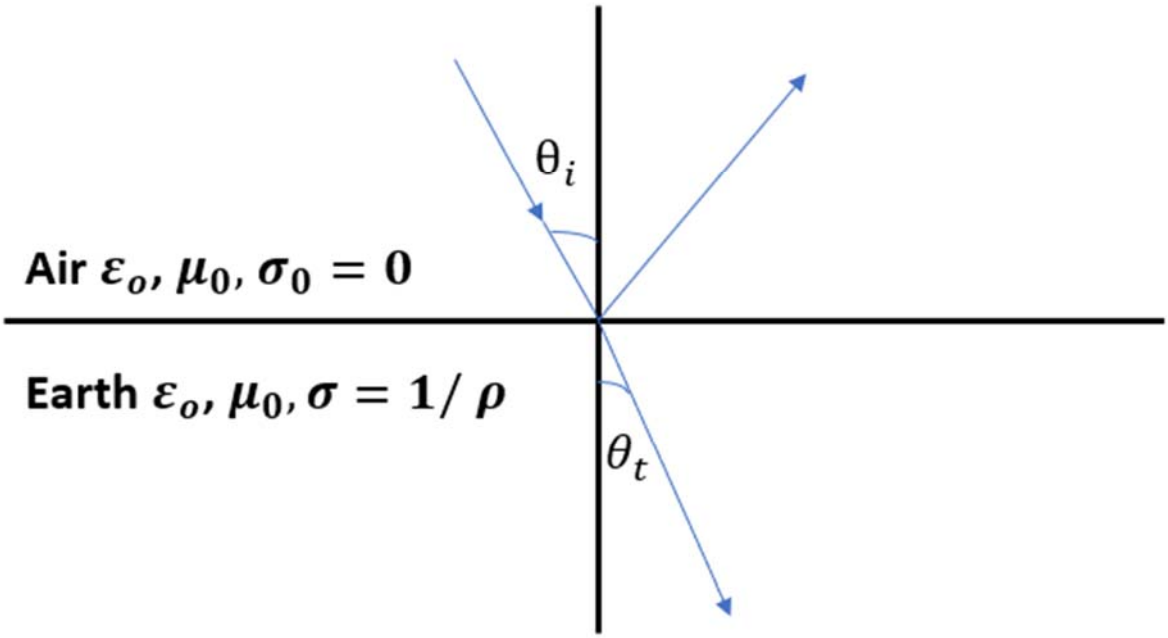

Figure 5.10 : Refraction of a plane electromagnetic wave at the air- earth interface

If we consider Snell's law at the air-earth interface then we have,

$$\frac{sin\theta_i}{v_0} = \frac{sin\theta_t}{v} \qquad (5.16)$$

Such that $v_0 = c = \frac{1}{\sqrt{\mu o \varepsilon_0}}$ and $v = \sqrt{\frac{2\omega}{\mu_0 \sigma}}$, c being the speed of light and v_0 and v are the velocities of EM waves in air and the earth, respectively. Therefore, if we substitute for the velocities in equation (5.19)

$$sin\theta_t = sin\theta_i \sqrt{\frac{2\varepsilon_0 \omega}{\sigma}}$$

The angular frequency, ω of MT measurements is < 10^4 Hz and since the subsurface resistivity, ρ is < 10^4 Ωm, then the term $\frac{2\varepsilon_0 \omega}{\sigma}$ <10^{-3}. This implies that θ_t will almost be zero hence the refracted wave will travel vertically downwards into the subsurface for all angles of incidence at the earth-air boundary.

Consider a Cartesian coordinate system with x, y, and z in the north, east, and vertical directions, respectively. If a uniform plane wave is propagating along the z direction, then there is no variation of electric and magnetic vectors for x and y. ($\frac{\partial}{\partial x} = 0, \frac{\partial}{\partial y} = 0 \; and \; E_z = 0$)

Equations 5.10a and 5.10b without the displacement terms can be rewritten as;

$$\frac{\partial E_x}{\partial z} = i\omega\mu_o H_y \qquad (5.17)$$

$$\frac{\partial H_y}{\partial z} = -\sigma E_x \qquad (5.18)$$

Differentiating the above equations for z, we obtain

$$\frac{\partial^2 E_x}{\partial z^2} = i\omega\mu_o \frac{\partial H_y}{\partial z} = -i\omega\mu_o\sigma E_x = -k^2 E_x \qquad (5.19)$$

$$\frac{\partial^2 H_y}{\partial z^2} = -\sigma \frac{\partial E_x}{\partial z} = -i\omega\mu_o\sigma H_y = -k^2 H_y \qquad (5.20)$$

Writing the general solutions of equations (5.19) and (5.20) we get

$$E_x = Ae^{-ikz} + Be^{ikz}$$

$$H_y = Ae^{-ikz} + Be^{ikz}$$

If we use Ampere's law, $\nabla \times \vec{H} = \vec{j} + \frac{\overrightarrow{\partial D}}{\partial t}$ and the relationship $\boldsymbol{k} = k\boldsymbol{u}$, where k is the propagation vector and **u** is normal to the planes of the constant phase.

From $\nabla \times \vec{H} = \overrightarrow{\sigma E} + \varepsilon \frac{\overrightarrow{\partial E}}{\partial t}$, it follows that $-ik \times \boldsymbol{H} = (\sigma E + i\varepsilon\omega)\boldsymbol{E} = \frac{ik^2}{\mu\omega} E$ or $\boldsymbol{E} = -\frac{\boldsymbol{\mu\omega}}{\boldsymbol{k}} \boldsymbol{u} \times \boldsymbol{H}$ (5.21)

For a vertically incident wave, then

$$\boldsymbol{u} = (0,0,1) \qquad \boldsymbol{u} \times \boldsymbol{H} = (-Hy, Hx, 0) \qquad (5.22)$$

Therefore, we have $E_x = \frac{\mu\omega}{k} H_y$ $E_y = \frac{\mu\omega}{k} H_x$ (5.23)

Equation (5.23) can be expressed in matrix form as

$$\begin{pmatrix} E_x \\ E_y \end{pmatrix} = \begin{pmatrix} 0 & Z_{xy} \\ Z_{yx} & 0 \end{pmatrix} \begin{pmatrix} H_x \\ H_y \end{pmatrix} \qquad (5.24)$$

Where,

The 2x2 matrix is a complex-valued second-rank impedance tensor (Z) while each element in the impedance tensor matrix represents the ratio of the electric field component to the magnetic field component in a specific direction.

$$Z_{xy} = \frac{E_x}{H_y} = \frac{i\mu\omega}{k} = \frac{i\mu\omega}{\sqrt{-i\mu\sigma\omega}} = \sqrt{\mu\rho\omega} \cdot e^{i\pi/4} \quad (5.25a)$$

$$\text{and } Z_{yx} = \frac{E_y}{H_x} = \frac{-i\omega\mu}{k} = -Z_{xy} \quad (5.25b)$$

The apparent resistivity and phase of the half-space can be determined by measuring the orthogonal elements of H and E

$$\rho = \frac{1}{\sigma} = \frac{1}{\mu\omega}\left|\frac{E_y}{H_x}\right|^2 = \frac{1}{\mu\omega}\left|\frac{E_x}{H_y}\right|^2 = \frac{1}{\mu\omega}|Z|^2 \text{ and } \emptyset = \arg(Z) = \frac{\pi}{4} \quad (5.26)$$

In non-homogeneous earth, the phase is not always equal to 45°, i.e., $\rho_a = \frac{1}{\mu\omega}|Z_0|^2$;

and $\emptyset_a = \arg(Z_0) \neq \frac{\pi}{4}$ and Z_0 is the impedance at the surface.

If we consider a 1D layered earth consisting of a set of N horizontal layers each with uniform conductivity σ, and thickness d (Figure 5.11). The EM field is excited in the earth by a

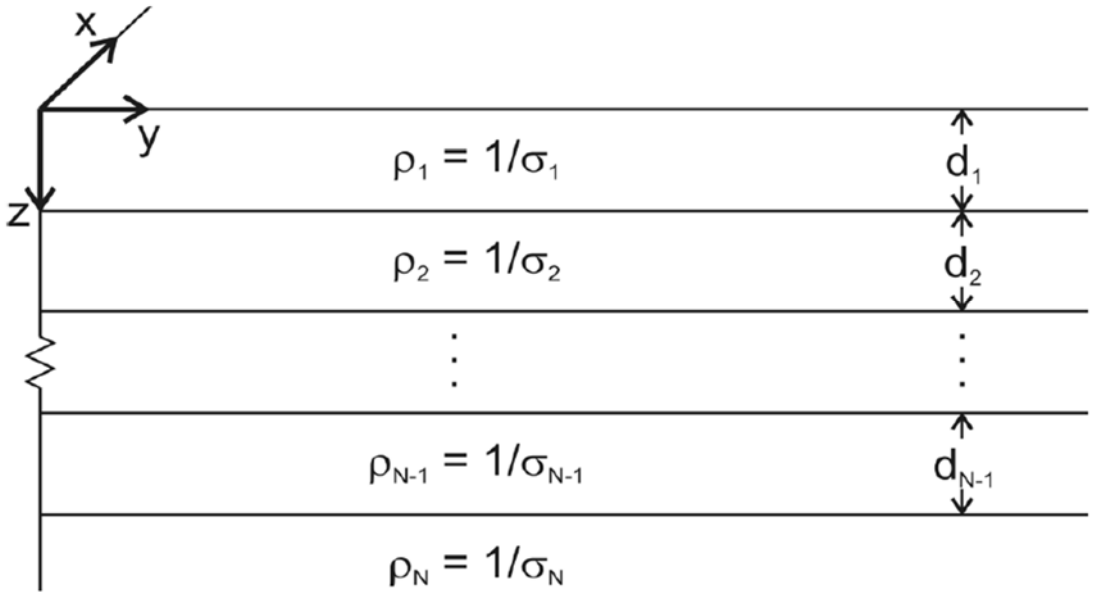

Figure 5.11: Representation of propagation of EM wave through a 1D layered earth. Adopted from (Lichoro, 2013)

downward travelling EM wave.

At the air-earth interface (resistivity varies with depth), Z=0 and therefore

$$\begin{pmatrix} E_x(\omega) \\ E_y(\omega) \end{pmatrix} = \begin{pmatrix} 0 & Z_{xy}(\omega) \\ Z_{yx}(\omega) & 0 \end{pmatrix} \begin{pmatrix} H_x(\omega) \\ H_y(\omega) \end{pmatrix} \quad (5.27)$$

$$\text{With} \qquad Z_{xy}(\omega) = -Z_{yx}(\omega) = \widehat{Z_1} \quad (5.28)$$

Magnetotelluric Transfer Functions

MT transfer functions describe the electrical resistivity of a half-space having the measurement site situated at the centre of the bounding horizon. MT transfer responses relate the measured EM components with the corresponding frequencies and are dependent on the electrical properties of the underlying Earth materials. MT transfer functions comprise the impedance tensor (Z) and geomagnetic transfer functions.

5.3.3 Impedance tensor functions and invariants

The impedance tensor relates the electric and magnetic fields at a given frequency. In matrix notation, this relationship can be represented as equation (5.29) and linearly represented as in Equations (5.30a) and (5.30b).

$$\begin{pmatrix} E_x(\omega) \\ E_y(\omega) \end{pmatrix} = \begin{pmatrix} Z_{xx}(\omega) & Z_{xy}(\omega) \\ Z_{yx}(\omega) & Z_{yy}(w) \end{pmatrix} \begin{pmatrix} H_x(\omega) \\ H_y(\omega) \end{pmatrix} \quad (5.29)$$

The diagonal elements relate the fields measured in the same direction whereas the off-diagonal elements relate the orthogonally measured fields.

$$E_x(\omega) = Z_{xx}(\omega)H_x(\omega) + Z_{xy}(\omega)H_y(\omega) \quad (5.30a)$$

$$E_y(\omega) = Z_{yx}(\omega)H_x(\omega) + Z_{yy}(\omega)H_y(\omega) \quad (5.30b)$$

Therefore, $\vec{E} = \hat{Z}\vec{H}$

1D Impedance Tensor

In a 1D environment, we assume that the resistivity varies with depth alone and thus the MT transfer functions are independent of the orientation of the measurement axes. The 1D impedance tensor is represented as;

$$\boldsymbol{Z}_{1D} = \begin{pmatrix} 0 & Z_{xy} \\ Z_{yx} & 0 \end{pmatrix}$$

In 1D structure, the diagonal elements are zero whereas the off-diagonal elements are equal in magnitude but have opposite signs. Therefore, in a homogeneous half-space, the apparent resistivity and phase which are dependent on ω can be given as.

$$\rho_a(\omega) = \frac{1}{\mu\omega}|\boldsymbol{Z}|^2 \qquad \text{Phase, } \emptyset = tan^{-1}\left(\frac{Im\boldsymbol{Z}}{Re\,\boldsymbol{Z}}\right) \quad (5.31)$$

2D Impedance Tensor

In a 2D earth, the resistivity varies with depth and in one of the two principal horizontal directions but remains constant in the other principal horizontal direction (the geo-electric strike). If we consider a 2D resistivity model with a lateral contact striking in the x-direction as shown in Figure 5.12. Then the EM fields can be decoupled into two modes where the E-field is parallel to the strike and the B-field perpendicular to the strike. The Transverse electric mode (TE) or E-polarization is where the electric field is parallel to the strike and the Transverse magnetic mode (TM), or B-polarization is where the magnetic field is parallel

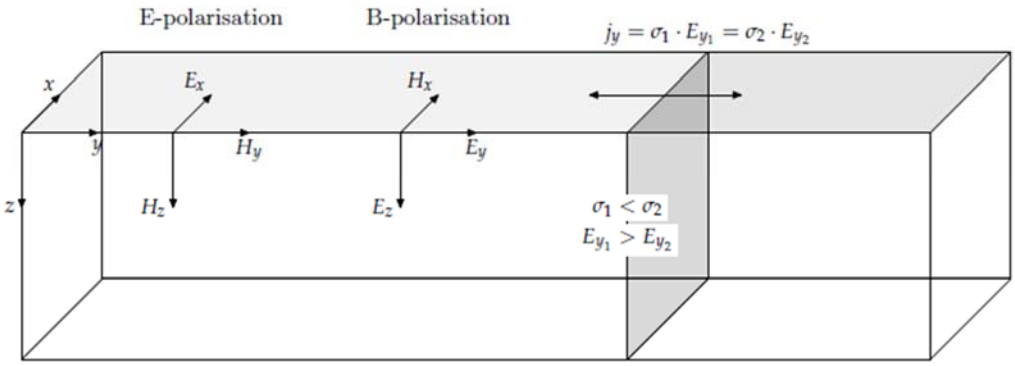

Figure 5.12: 2D resistivity model with a resistivity boundary separating two regions of differing conductivities. Adopted from (Thiel, 2008)

to the strike.

From the equation of continuity, it follows that the electric currents on either side of the resistivity boundary (which could be a fault, dyke or any other rock assemblage) must be conserved implying that normal current components must be continuous on both sides of the boundary (Thiel, 2008). Using Equation (5.9c) and the continuity condition we can see that $j_{y1} = \sigma_1 \cdot E_{y1} = \sigma_2 \cdot E_{y2} = K$, where K is a constant.

The resistivity boundary causes a jump in the electric field normal to the boundary whereas the normal and tangential components of the magnetic field are continuous across the boundary. For a 2D Earth, if the measurement direction is parallel and perpendicular to the strike direction, then the diagonal elements of the impedance tensor are zero. However, this is rarely achieved in practice due to the current distortions during measurements.

$$\boldsymbol{Z}_{2D} = \begin{pmatrix} 0 & Z_{xy} \\ Z_{yx} & 0 \end{pmatrix} \tag{5.32}$$

Where,

$$Z_{xy}(\omega) = Z_{TE} = \frac{E_x(\omega)}{H_y(\omega)}$$

$$Z_{yx}(\omega) = Z_{TM} = \frac{E_y(\omega)}{H_x(\omega)}$$

The above equations give rise to two sets of apparent resistivity and phases;

$$\text{TM-mode } \rho_{yx} = \frac{1}{\mu\omega}\left|Z_{yx}\right|^2 \text{ ; } \emptyset_{yx} \text{ and TE-mode } \rho_{xy} = \frac{1}{\mu\omega}\left|Z_{xy}\right|^2 \text{ ; } \emptyset_{xy}$$

From Figure 5.12, the electric field component E_{y1} of the B-polarization is discontinuous at the boundary hence making the TM apparent resistivity discontinuous with an offset of $(\sigma_2/\sigma_1)^2$. Because of this offset in the apparent resistivity, the B-polarization achieves a sharper resolution in the lateral variation of resistivity. However, caution should be taken when considering the B-polarization since the resistivity close to the boundaries is estimated too low for the conductive region and too high for the more resistive region (Thiel, 2008). On the other hand, the E-polarization apparent resistivities vary smoothly across vertical contacts hence TE-mode provides a more stable apparent resistivity estimate.

3D Impedance Tensor

To accurately characterize the Earth's properties, the Earth needs to be treated in a 3D manner. In a 3D setting, the impedance tensor is given as;

$$\boldsymbol{Z}_{3D} = \begin{pmatrix} Z_{xx} & Z_{xy} \\ Z_{yx} & Z_{yy} \end{pmatrix} \tag{5.33}$$

The impedance tensor components are non-zero and are, therefore, all considered during the data processing and interpretation. The full impedance tensor can be used to derive different forms of the apparent resistivities both rotationally dependent and independent.

Rotationally dependent apparent resistivities can be given as;

$$\rho_{yx} = \frac{1}{\mu\omega}\left|Z_{yx}\right|^2 \text{ and } \rho_{xy} = \frac{1}{\mu\omega}\left|Z_{xy}\right|^2 \text{ ; Phase } \emptyset = tan^{-1}\left(\frac{ImZ}{ReZ}\right) \tag{5.34}$$

Invariants

Several parameters exist that are the same, independent of the azimuth of the principal axis of the impedance tensor. These are called invariants.

One invariant is the determinant of the impedance tensor is $Z_{det} = \sqrt{Z_{xx}Z_{yy} - Z_{xy}Z_{yx}}$ and the corresponding apparent resistivity is

$$\rho_{det} = \frac{1}{\mu\omega}|Z_{det}|^2 \text{ and the phase } \emptyset_{det} = \arg\left(Z_{det}\right) \tag{5.35}$$

Other invariants include the arithmetic mean

$$Z_{ave} = \frac{Z_{xy} - Z_{yx}}{2}$$

with a corresponding apparent resistivity

$$\rho_{ave} = \frac{1}{\mu\omega}|Z_{ave}|^2 \text{ , Phase } \emptyset_{ave} = \arg\left(Z_{ave}\right) \tag{5.36}$$

The geometric mean can also be calculated from;

$$\text{Geometric mean; } Z_{gme} = \sqrt{-Z_{xy}Z_{yx}}$$

The average, determinant and geometric mean are useful in calculating different types of apparent resistivities and phases which can then be compared to find the most reasonable representation of the subsurface resistivity structure of an area.

5.3.4 Dimensionality tools

Before the inversion of MT data, careful analysis should be made to determine the appropriate dimensionality of the data. It is important to know whether the data are 1D, 2D or 3D - at which periods and for which sites. Various dimensionality tools have been proposed and are listed below.

Ellipticity

The ellipticity of the MT response tensor is represented as the ratio of the minor axis of the impedance ellipse divided by the major axis (Chave & Jones, 2012). The ellipticity is a function of rotation angle thus for a pure 1D response is undefined regardless of the angle. On the contrary, the ellipticity for a 2D response will be zero when the rotation angle is in the strike coordinates. This implies that ellipticity can be used as both a dimensionality and directionality tool.

$$ellipticity\ (\theta)\ =\ \frac{|Z_{xx}(\theta)-Z_{yy}(\theta)|}{|Z_{xy}(\theta)+Z_{yx}(\theta)|} \tag{5.37}$$

It is important to note that ellipticity is highly sensitive to noise and ellipticity distribution can have many extreme values regardless of dimensionality (Chave & Jones, 2012)

Skew

The skew is also known as the Swift skew after Charles Swift (Swift, 1967). It is the skew of the MT impedance tensor mathematically given as the ratio of trace to the anti-trace of the MT response tensor. The trace is the sum of the elements on the diagonal while the anti-trace is the sum of the elements on the anti-diagonal of the MT impedance tensor. It is based on the amplitude of the response tensor.

$$Skew\ =\ \frac{|Z_{xx}+Z_{yy}|}{|Z_{xy}-Z_{yx}|} \tag{5.38}$$

The skew is rotationally invariant since the trace and anti-trace of the MT response tensor are rotationally invariant. Common practice is to consider data sets with skew values below 0.2 as being either 1D or 2D and data with skew values above 0.2 as being 3D (Chave & Jones, 2012). Due to the statistical complexities involved in the skew and the error propagation in the presence of noise and distortions (Pedersen & Svennekjaer, 1984), caution should be taken while implementing the skew. This is because skew is highly sensitive to noise. Also, in the presence of noise, there is a likelihood that the data over 1D or 2D structures would be misinterpreted as 3D since the skew value would lie above 0.2.

Polar diagrams

Another amplitude-based dimensionality tool is the polar diagrams which are essentially shapes derived from the magnitudes of the diagonal and off-diagonal tensor elements of the MT impedance tensor by plotting $|Z_{xx}(\theta)|$ and $|Z_{xy}(\theta)|$ as (θ) is rotated through 360° (or 90° due to symmetry) (Chave & Jones, 2012). For a purely 1D earth, the $|Z_{xx}(\theta)|$ term is zero for all angles and $|Z_{xy}(\theta)|$ describes a perfect circle (Figure 5.14a). On the other hand, when the response is from a purely 2D earth, $|Z_{xy}(\theta)|$ describes an ellipse for low to moderate anisotropy Z_{xy} *and* Z_{yx}. For higher anisotropy, the shape changes to a peanut (Figure 5.14b).

Symmetry is lost for 3D responses except when the site is located at a point of geometric symmetry. For 3D scenarios, the $|Z_{xx}(\theta)|$ does not display zeros at four cardinal points 90° apart at the angles where the $|Z_{xy}(\theta)|$ reaches maxima and minima (Figure 5.14c).

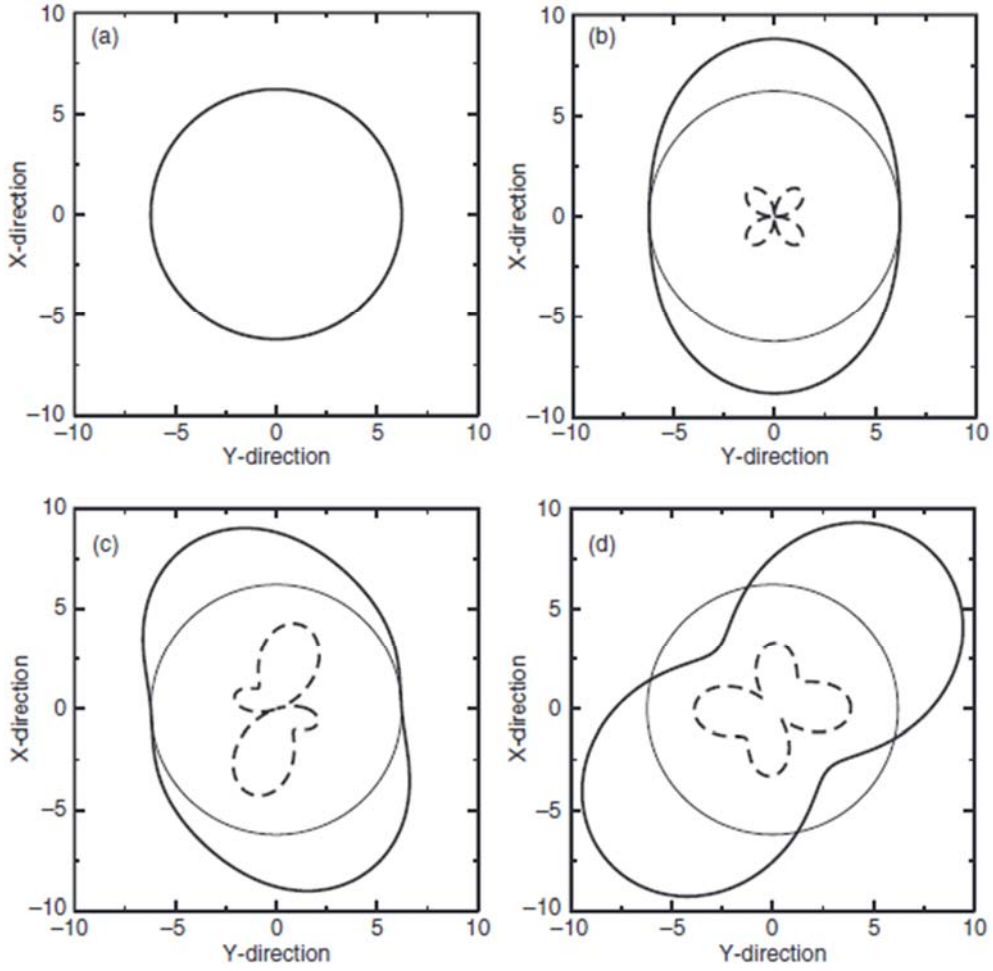

Figure 5.13: Polar diagrams for (a), 1D (b), 2D (c) 3D and (d) 2D/3D MT responses. The thin circle represents a 1D unit circle, the dashed lines represent the diagonal elements and the thick full circle represents the off-diagonal elements. Adopted from (Chave & Jones, 2012)

Polar diagrams are badly affected by noise and distortions and, therefore, they can be misleading and ought to be used with caution. So far, the three-dimensionality tools discussed above are amplitude-based and are all seriously affected by distortion and, therefore, deemed unreliable.

Better dimensionality tools have been proposed and are described at length (Chave & Jones, 2012). They include Bahr's phase-sensitive skew, WAL invariants, Groom-Bailey dimensionality analysis, and phase tensor.

Phase Tensor

The phase tensor in MT expresses the relationships between the phases of the magnetic and electric fields with period (depth). This approach is advantageous due to its independence from the galvanic distortion of the electric field caused by shallow inhomogeneities and preserves the regional phase information (Caldwell et al., 2004). The phase tensor can be visualized as an ellipse where the major and minor axes of the ellipse represent the principal axes of the tensor. The lengths of these axes correspond to the values of the tensor elements.

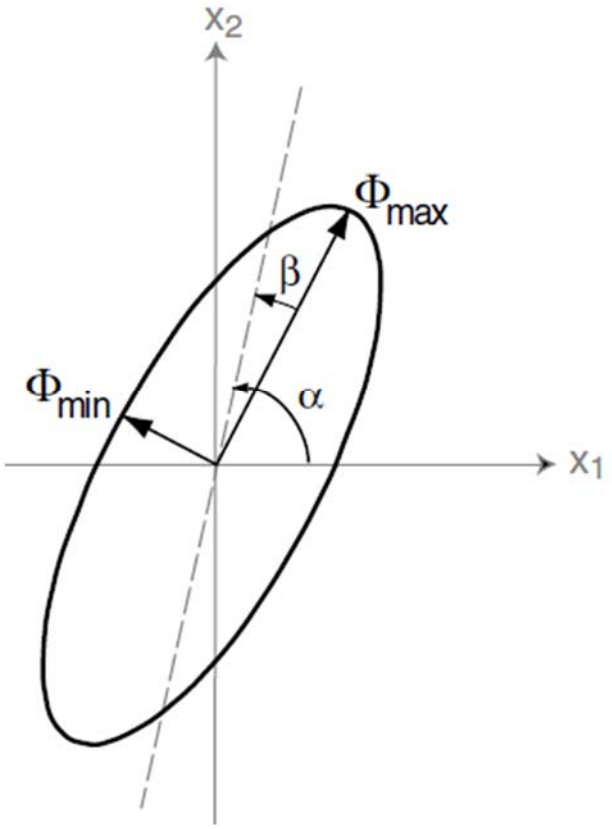

Figure 5.14: *Schematic of MT phase tensor. The lengths of the ellipse axes correspond to the principal values of the tensor elements. A non-symmetric phase tensor is characterised by an angle β which is a third coordinate invariant dependant on the skew of the tensor ellipse. Adapted from (Caldwell et al., 2004; Ssemuyaba et al., 2023)*

The orientation of the major axis is specified by the angle $\alpha - \beta$ (Figure 5.15).

The representation of the tensor ellipse for a 1D scenario is a circle of unit radius at all periods. If the conductivity is both anisotropic and 1D, the radius of the circle varies with the period in tandem with the variation of conductivity with depth. (i.e., the radius increases if the conductivity increases with depth).

Phase tensor representation of the impedance tensor is advantageous because the two sets of principal axes that characterize the impedance tensor can be simply and directly depicted. In addition, the phase tensors are independent of the rotational angle, only the angle specifying the orientation of the diagram for the observer changes. Phase tensor is independent of near-surface galvanic distortions and hence the regional phase information is preserved or unaffected at all periods.

5.3.5 Directionality tools

Electrical strike analysis of MT data indicates the directions of resistivity contrasts which are often due to geological structures but are not necessarily seen on the surface. In addition to the resistivity structures below and around the site, the elements of the MT impedance tensor depend on the orientation of the x and y directions of the field layout.

In electrical strike analyses, the MT data are mathematically rotated from the measurement layout coordinate system to minimize the diagonal elements of the impedance tensor. In the rotated coordinated system, the x-axis (Z-strike) is parallel or perpendicular to the main resistivity boundaries (main geological features). Whether it is parallel or perpendicular, can be resolved by analyzing the relation between measured vertical (Hz) and the horizontal (Hx and Hy) magnetic fields and expressed as induction arrows or T-strike. The description of the T-strike and Z-strike presented here is based on the publication by Hersir et al., 2022.

For a 2D Earth, the resistivity varies with depth and in one principal horizontal direction. The horizontal angle perpendicular to that direction is called the electrical strike. The angle it makes with geographical north is called the Swift angle or Z-strike Φ (Hersir et al., 2022). It is possible to rotate the coordinate system and recalculate the elements of the impedance tensor for any desired direction. This allows the fields (electric, E, and magnetic, H) to be represented as if they had been measured in these rotated directions. If the Earth is 2D and the coordinate system of the field layout has an axis parallel to the electrical strike direction, the impedance tensor elements are $Z_{xx} = Z_{yy} = 0$, but $Z_{xy} \neq Z_{yx}$.

From the rotated tensor, we obtain two different apparent resistivities (ρ_{xy} and ρ_{yx}) and two apparent phases (θ_{xy} and θ_{xy}). In a 1D Earth model, these values are equal. The electrical strike, also known as the Z-strike, can be determined by minimizing the absolute values of the diagonal tensor elements, $|Zxx|^2 + |Zyy|^2$, with respect to the angle of rotation, Φ. However, there is a 90-degree ambiguity in the strike angle determined in this way, as the diagonal elements are minimized when either the x-axis or the y-axis is aligned with the electrical strike. The depth of investigation increases with the period of the measurements. Importantly, the dominant electrical strike can vary at different depths, reflecting the presence of different geological structures at different subsurface levels.

The tipper vector, **T**, relates the vertical component of the magnetic field to the two horizontal components:

$$H_Z = T_x H_x + T_y H_y \tag{5.39}$$

Where T_x and T_y are the x and y components of the tipper, respectively.

For a 1D Earth model, the tipper value is zero, meaning $T_x = T_y = 0$. In the case of a 2D Earth model, the coordinate system can be rotated so that the x-axis is aligned with the strike

direction. This results in $T_x = 0$ while $T_y \neq 0$. This alignment is achieved by minimizing $|T_x|$. Unlike the Z-strike, which suffers from a 90° ambiguity, the T-strike determined in this way does not have this ambiguity. The tipper can be represented by two real vector quantities corresponding to its real and imaginary parts.

At sufficiently low frequencies, the real component of the tipper vector points away from zones of high conductivity and towards zones of low conductivity. The length of the arrows indicates the magnitude of the resistivity contrast. For a 2-dimensional Earth, the real and imaginary components of the tipper arrows are collinear and point perpendicular to the geoelectric strike direction (Hersir et al., 2022), (Berdichevsky & Dmitriev, 2010). This means the arrows are aligned with the direction of the geological structures or features that cause the observed electrical resistivity variations.

6 Electromagnet distortions in the Earth

One of the greatest challenges in the application and interpretation of MT data is the distortion of regional electric fields by local structures causing erroneous interpretations and unreliable conclusions about the Earth's subsurface resistivity structure. Various types of distortions can interfere or obscure the recorded signals complicating the interpretation of the subsurface electrical properties. The distortions can arise from a range of sources which include (Chave & Jones, 2012);

- **Cultural noise**: This distortion arises from human activities and infrastructure such as railway lines, electrical power lines, fences and other industrial machinery that generates electromagnetic interference that can impede natural MT signals.
- **Coastal effects:** The presence of conductive seawater in coastal areas can influence the MT signals leading to distortions that need to be accounted for during data processing and interpretation.
- **Topographic effects:** Variations in topography can influence the MT measurements at a particular site causing subsurface resistivities to be under or over-estimated depending on whether one is in the valley or on the mountainous side (Jiracek, 1990)
- **Static shift:** This is a systematic bias in the data resulting from near-surface resistivity heterogeneities that lead to frequency-dependent distortions in the apparent resistivity. The static shift phenomenon is explored later in the chapter.
- **Instrument Drift:** Drift in the MT recording equipment can introduce low-frequency variations in the data which might distort the true response from the subsurface
- **Instrument noise:** These may include thermal noise, electronic noise, and environmental interferences such as wind that affect the quality of the data hence leading to distortions in the recorded signal.
- **Galvanic/or Near-surface effects**: Shallow subsurface features such as very resistive or very conductive layers can introduce distortions in the MT data impacting the accuracy of the subsequent subsurface electrical conductivity models.

Distortions due to dimensionality occur when the MT responses are of a higher dimension than being used in their interpretation i.e., using 1D interpretation techniques for 2D and 3D dimensional structures or 2D interpretation of 3D structures.

The primary goal of using MT data is to obtain the regional resistivity structure from time variations of the electric and magnetic fields. The regional electromagnetic fields (especially the electric field) are disturbed by site-specific local features that produce local electric and magnetic fields. The inherent task would then be separating regional from local fields and understanding how the local fields affect the observations.

Electromagnetic field distortions can be categorized into two forms, those due to currents and those due to charges. Because magnetic fields are continuous and integrating, they are directly affected by distortion due to currents (indirect magnetic effects of charge due to current deflection fall off rapidly with increasing periods and can usually be neglected on land) (Chave & Jones, 2012).

On the other hand, the local nature of electric fields and their discontinuity at resistivity boundaries leads to their strong distortion from charges at these boundaries. Since the charge effects are frequency-independent in the inductive case, they are present even at the smallest frequency (longest period)/ present across all the frequency ranges.

Therefore, it is important to identify distortions and be able to devise methods or techniques that can be used to remove them. Chave & Jones, 2012 summarize some of the theoretical approaches to distortion identification and removal that have been proposed by numerous researchers. One of the methods is the Groom-Bailey distortion decomposition (Groom & Bailey, 1991) in which the determinable and indeterminable distortion elements are separated. The indeterminable elements comprise effects that only cause a change in the electric field amplitude (manifested as static shifts) whereas the determinable comprise effects that result in changes to both the amplitude and phase of the electric field (Chave & Jones, 2012). Other approaches include the phase tensor approach of (Caldwell et al., 2004), Berdichevsky's galvanic distortion effects (Berdichevsky & Dmitriev, 2009), Larsen's galvanic distortion of a 1D regional Earth (Larsen, 1977) and Pedersen's distortion decomposition (Zhang et al., 1987).

6.1 The static shift phenomenon

Static shift is an inherent uncertainty in MT data, which is largely attributed to local near-surface resistivity inhomogeneities and topographic effects. Both MT and DC methods are susceptible to this issue because they rely on measuring the electric field or voltages at the Earth's surface over relatively short distances (Árnason, 2015). This static shift typically arises from the accumulation of electrical charges at resistivity boundaries, causing the electrical field to be discontinuous near these boundaries (Lichoro, 2013). Static shifts occur when the dimensions of an anomalous subsurface body are much smaller than the electromagnetic skin depth, which is the depth at which the electromagnetic field amplitude decreases by a factor of 1/e.

Static shift refers to a parallel shift of the apparent resistivity curves when plotted on a logarithmic scale. This shift is characterized by a constant multiplicative factor 'S' that affects

the apparent resistivity values independently of the frequency. As a result, the true or correct resistivity level may be located above, below, or in between the measured responses, depending on whether the two polarizations (e.g., TE and TM modes) are shifted differently. If this static shift is not corrected, it will introduce erroneous structures in the final inversion models. It is important to note that the static shift only affects the apparent resistivity and not the phase (Jones & Groom, 1993) since the phase data alone lacks information on the absolute resistivity values.

At late times, the apparent resistivity from a TEM sounding is independent of near-surface resistivity structures. The most common and reliable method to correct the MT data for static shift is to use a co-located central loop TEM sounding and jointly invert the TEM data with the MT data and adjust the shift multiplier S as well as the resistivity model. Apart from topographic distortions, there are two main reasons for MT static shift:

Current distortion (current channelling)

When the current flowing in the Earth encounters near-surface conductivity anomalies, its flow path will be altered. Current channeling is due to superficial bodies that distort the current distribution hence distorting the electric field, causing the impedance magnitude to increase or decrease by a scaling factor. This factor shifts the apparent resistivity curve on logscale as mentioned earlier. Consider a superficial body of resistivity ρ_2 which is lower than the resistivity of the surrounding ground ρ_1. Considerable amounts of the current will be channeled through the body due to its low resistivity reducing the current density (and voltage difference) at the surface. However, if $\rho_2 > \rho_1$, then all the current will be repelled away from the body leading to increased current density at the surface. This is referred to as current distortion (Figure 6.1).

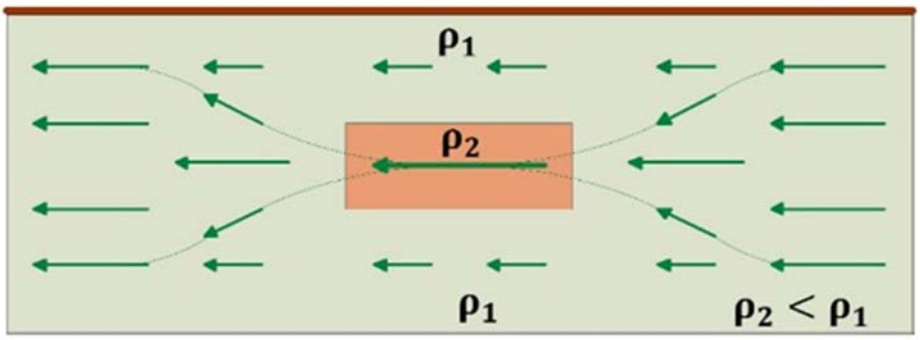

Figure 6.1: Current distortion. Adopted from (Árnason, 2008)

Electrical/voltage field distortion

A vertical resistivity discontinuity that is embedded within a homogeneous Earth yields a different electric field and voltage measurements compared to the homogeneous Earth, assuming the same current density. A measurement over an anomaly that is more conductive yields a lower electrical field and voltage measurement compared to measurements over the

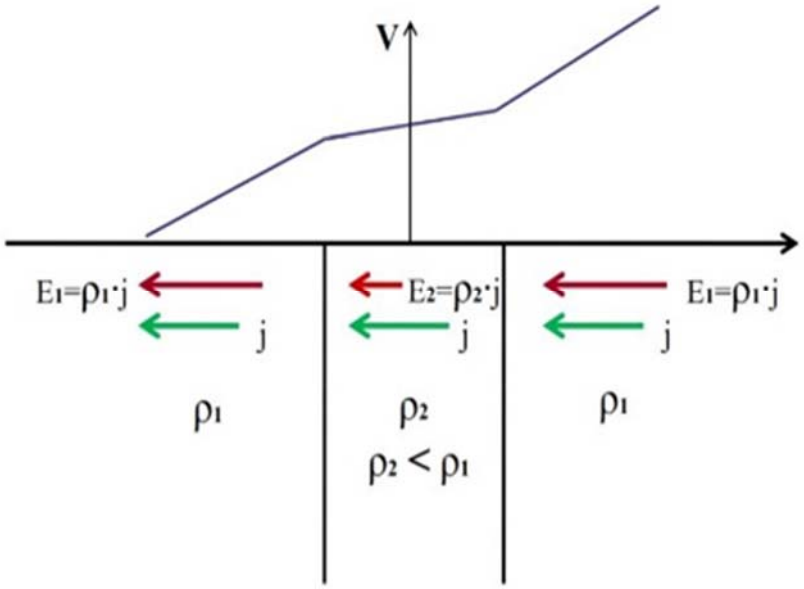

Figure 6.2: Electrical field distortion with a conductive anomaly embedded in a resistive Earth. Voltage measurements over the different parts of the subsurface are shown. Adopted from (Árnason, 2008)

resistive homogeneous Earth without the conductive anomaly (Figure 6.2). The effect is the opposite for a resistive anomaly embedded within a more conductive homogenous half-space. The distortion of the voltage measurement is most severe when the dipole length is in the same order as the width of the anomaly. When the dipole length is much larger than the anomaly, the measurements of the electrical field start to approach that of the homogeneous Earth.

6.1.1 Galvanic Topographic Effects

Undulations in the topography of an area can cause static distortions such that currents accumulate more beneath depressions and disperse on peaks (Lichoro, 2013) hence increasing the electric field in valleys and reducing it on the hills. Jiracek (1990) described the formation of charges on the surface of the undulations (Figure 6.3) in accordance with

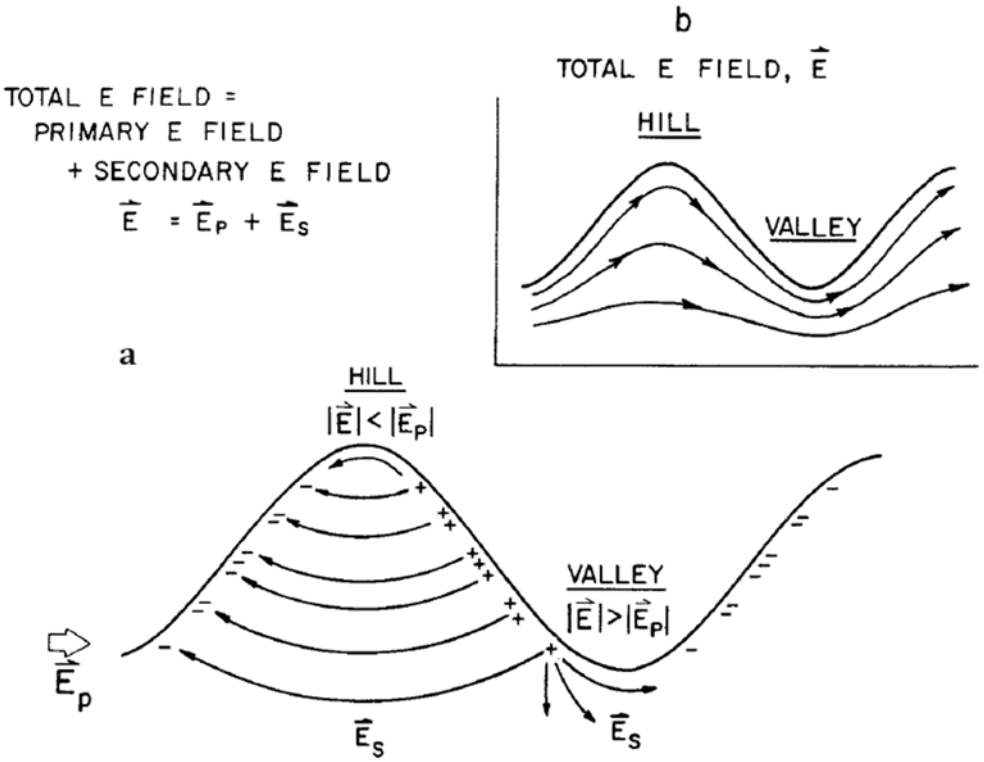

Figure 6.3: Galvanic effects due to topography: (a) Galvanic charge distribution for a hill-valley setting. (b) Resulting total electric field pattern from the vectorial summation of primary and secondary fields. Adopted from (Jiracek, 1990)

the surface charge density equation.

The resultant electric field is high in the valley and low on the hillside resulting in an apparent shift of the resistivity curves. In the central loop TEM method, the magnetic field decay rate is measured, which reflects the current distribution induced by the turn-off of the current in the source loop. As the induced currents propagate outward and downward over time, they are initially only dependent on the near-surface resistivity structure. However, at later time gates, the distortions due to topography and apparent resistivity become primarily dependent on the conductivity structure at depth, rather than the shallow, near-surface topographical effects (Árnason et al., 2010). The current distortion caused by topographic features at shallow depths has a diminishing influence on the TEM data at later time gates. This is because the induced currents have had sufficient time to diffuse deep below the surface, effectively masking the impact of the near-surface topographical distortions.

In the central loop TEM method, we measure the magnetic field decay rate from the current distribution induced by the current turn-off in the source loop. As the currents propagate outward and downward with time, they only depend on the near-surface resistivity structure at early times. For late times, the distortions due to topography and apparent resistivity are only dependent on the conductivity structure at depth rather than shallow (near surface) topographical effects (Árnason et al., 2010). The current distortion at shallow depth due to topographic effects has a vanishing influence on the TEM data at late times when the induced currents have diffused deep below the surface.

7 MT and TEM Data Post-field Treatment

7.1 TEM Field procedure and measurement

TEM data at the Buranga geothermal prospect were collected in two campaigns in 2015 and 2019 using two types of equipment, the Zonge GDP 32^{24} and the Phoenix V8 receiver with a T4 transmitter (Figure 7.1).

Figure 7.1: (a) The Phoenix V8 receiver, (b) The Phoenix T4 Transmitter.

Both the Zonge and the Phoenix TEM systems consist of a transmitter, a transmitting (source) loop, a receiver, a receiver loop usually having an effective area of 10,000 m^2, and a power source (such as a generator or car battery). For the Phoenix system, 10,000 m^2 coincident receiver and source loops were used. The synchronization between the receiver and transmitter is achieved by radio communication. A square transmitting loop of 100 m x 100 m is laid out on the ground and a current is injected into the source loop by using a 12

V car battery. The input voltage is then amplified by the transmitter to achieve higher voltages. The synchronization for the Zonge equipment is achieved by warming up the high-precision crystal clocks for about an hour and then the transmitter is synchronized with the receiver. The transient response (induced voltages) is measured at the center of the transmitter loop hence the name central loop sounding.

7.1.1 TEM data processing

Raw TEM data files (*.CAC, *.TSS) from the receiver are dumped to a field computer and then converted to AVG and USF file formats using the "TEMAVGW" (Zonge Engineering & Research organization, 1993) and WinG Link (Lichoro, 2015) programs for the Zonge and Phoenix equipment, respectively. AVG and USF files are further processed by the TemX code that was developed at Iceland GeoSurvey, ÍSOR (Árnason, 2006b). This code performs normalization of the voltages for the transmitted current, gain and effective area of the transmitter and receiver loop/coil and then displays all the data graphically, allowing the user to omit outliers and input site-specific information such as site name, location and coordinates, source loop size, turn off time, elevation, and receiver loop size. TemX calculates and averages voltage readings and calculates late-time apparent resistivity. The program produces an output file, an INV file, ready for inversion by the TEMTD program (Árnason, 2006a). A special script, Zavg2temtd, was also used to convert AVG files to TEMTD readable INV files in the pre-inversion preparation of the Zonge TEM data.

The output from the TemX program is used as an input for TEMTD which is a program used to perform a 1D inversion of TEM and MT data either separately or jointly for both datasets. The TEMTD program utilizes a forward algorithm that calculates the induced transient voltage in the receiver coil. This calculation is performed by summing the responses from the successive turn-on and turn-off events of the transmitted current.

When performing 1D inversion of TEM data, the Earth is assumed to consist of horizontally

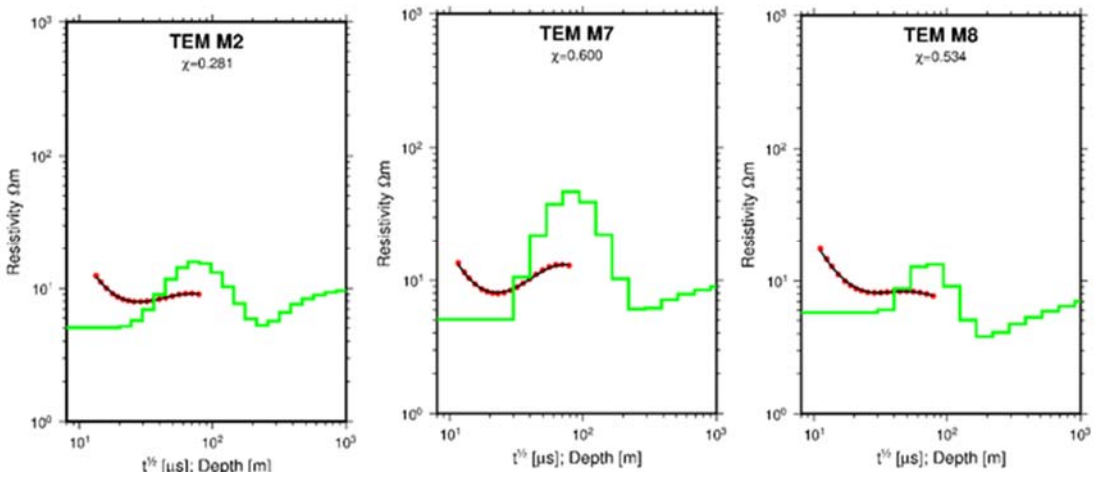

Figure 7.2: 1D Occam inversion of three TEM soundings, M2, M7 and M8, from the Buranga prospect (Ssemuyaba, 2021),(Ssemuyaba et al., 2023) Red dots are measured apparent resistivity values, black line shows the calculated apparent resistivity from the 1D model in green, and χ is the RMS misfit between the measured and calculated data from the model.

stratified layers with varying resistivities and thicknesses. Therefore, the inversion routine seeks to fit the measured responses to a layered Earth model with the optimal resistivity and thicknesses for each layer. The TEMTD program also offers the option of performing a minimum structure (Occam) inversion where the thicknesses of the resistivity layers are kept fixed while changing the resistivity during the inversion. The thicknesses of the layers increase exponentially with depth. Typical inversion results from Occam 1D inversion of TEM data at Buranga (Ssemuyaba et al., 2023) are shown in Figure 7.2

7.2 MT Field procedure and measurement

The Buranga MT data were collected in three different campaigns in 2016, 2017 and 2019 by staff from GRD. MT data acquisition in the Buranga prospect was done using the five-component data acquisition (MTU-5A) instrumentation (Figure 7.3) from Phoenix geophysics. It is a relatively light equipment consisting of three magnetic field sensors, Hx, Hy, and Hz, and two electric field channels, Ex, and Ey (Figure 7.4a). The recorder has a 130 dB dynamic range with a gain that can be varied by a factor of 4 and has an inbuilt power

line notch filter of > 40 dB. Each MTU box comes with two MTC-50H, one AMT-30 induction coil and five non-polarizing porous pot electrodes.

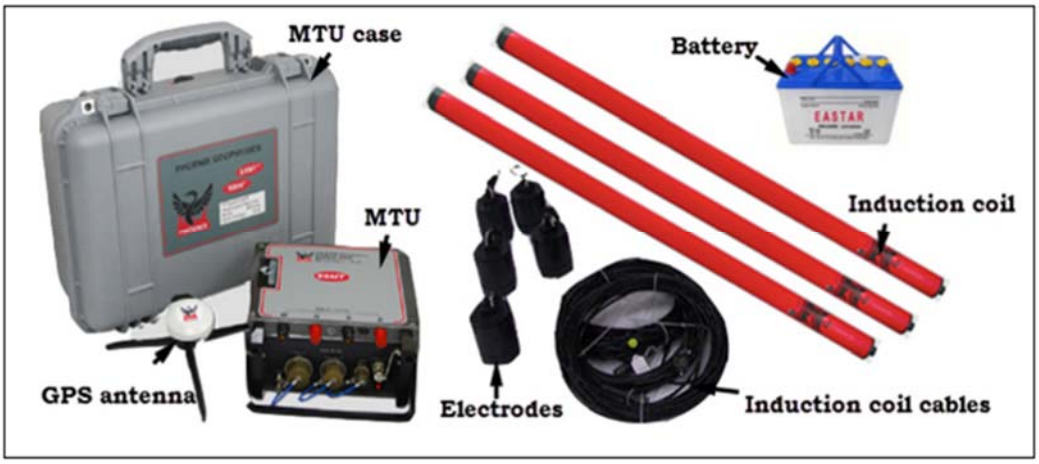

Figure 7.3: Instrumentation for a typical MTU-5A station. Adopted from (Phoenix, 2015)

Before the equipment is deployed for data acquisition, the MTU boxes, as well as the induction coils, are calibrated near or within the survey area and the amplitude response curves of the coils and boxes are checked to ensure that they are in good condition. A start-up file is created that contains equipment and site-specific parameters. The porous pot electrodes are usually checked using a multi-meter and paired according to the minimal static voltage that they generate between themselves.

In the field setup, the MTU data datalogger is placed at the centre of the sounding and grounded with a porous pot. The porous pot electrodes are buried into the ground and contact resistance is improved by pouring salt water or adding some bentonite clay solution in case the ground is very resistive. The electric field components Ex and Ey are measured using an electric dipole of two porous pot electrodes at a known distance of separation (i.e., 80 m at Buranga) with one dipole oriented in the magnetic N-S direction and the other in the E-W direction. The magnetic components are measured using three induction coils, H_x and H_y for the horizontal field and H_z for the vertical field. H_x and H_y are both horizontal but perpendicular to each other (same direction as E_x and E_y), normally magnetic N-S (H_x) and E-W (H_y), respectively.

The induction coils are oriented with the head (end of coil) facing north for H_x, facing east for H_y and facing down for H_z. They are levelled and buried to minimize effects due to temperature changes and noise caused by the shaking of trees or vegetation. The vibration of the coils causes unwanted noise in the data.

CF (storage data) card containing the start-up file is inserted into the MTU box and acquisition is started, usually lasting for at least 20 hours in geothermal prospecting. The data acquisition is GPS synchronized using a clock system. When the acquisition is done, the CF card is removed from the box and recorded time series data are dumped onto a field computer for storing and processing.

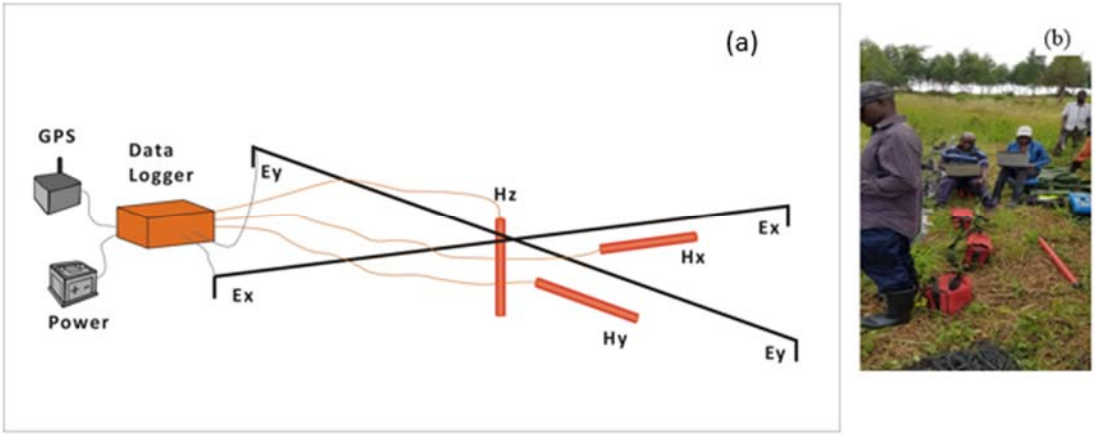

Figure 7.4: *(a) Layout of an MT sounding: Hx, Hy and Hz represent the magnetic coils oriented in the north, east and vertical direction, respectively, while Ex and Ey are the electric dipoles. Figure adopted from Hersir et al.(2022) ; (b): Field crew preparing for sensor and box calibration at Buranga.*

It is a common practice to have one MT station installed a few tens of kilometres away from the survey area and keep it running as a remote reference station to be used in data processing to reduce the effects of local noise sources. Noise reduction using remote reference sites is possible because magnetic signals are usually uniform over a large area. Most of the noise in MT is present in the electric field component. Consequently, the local electric field disturbances at the measurement station may not be recorded at the remote reference station, thus allowing robust processing and removal of disturbance at the local station using local and remote station coherency and uniformity of the magnetic source.

7.3 Time series processing

A total of 165 MT stations were deployed during MT data field campaigns (see Figure 7.5 for the sounding locations). For this research, time series (TSER) data were available from the 2016 and 2019 campaigns and processed edi (electrical data interchange standard) files were available for data collected in 2017. The processing software that was used is from Phoenix Geosystems (Phoenix, 2005). Using the Synchro time-series view program, time series data, and power spectra are graphically inspected (Figure 7.6), as a preliminary quality check of the data. This helps identify bad channels or channels that were completely off during acquisition. Repeated measurements are sometimes done for bad data acquisition. When this preliminary check is finished, the TSER data are Fourier transformed from time series to the frequency domain using the SSMT2000 software (Phoenix, 2005).

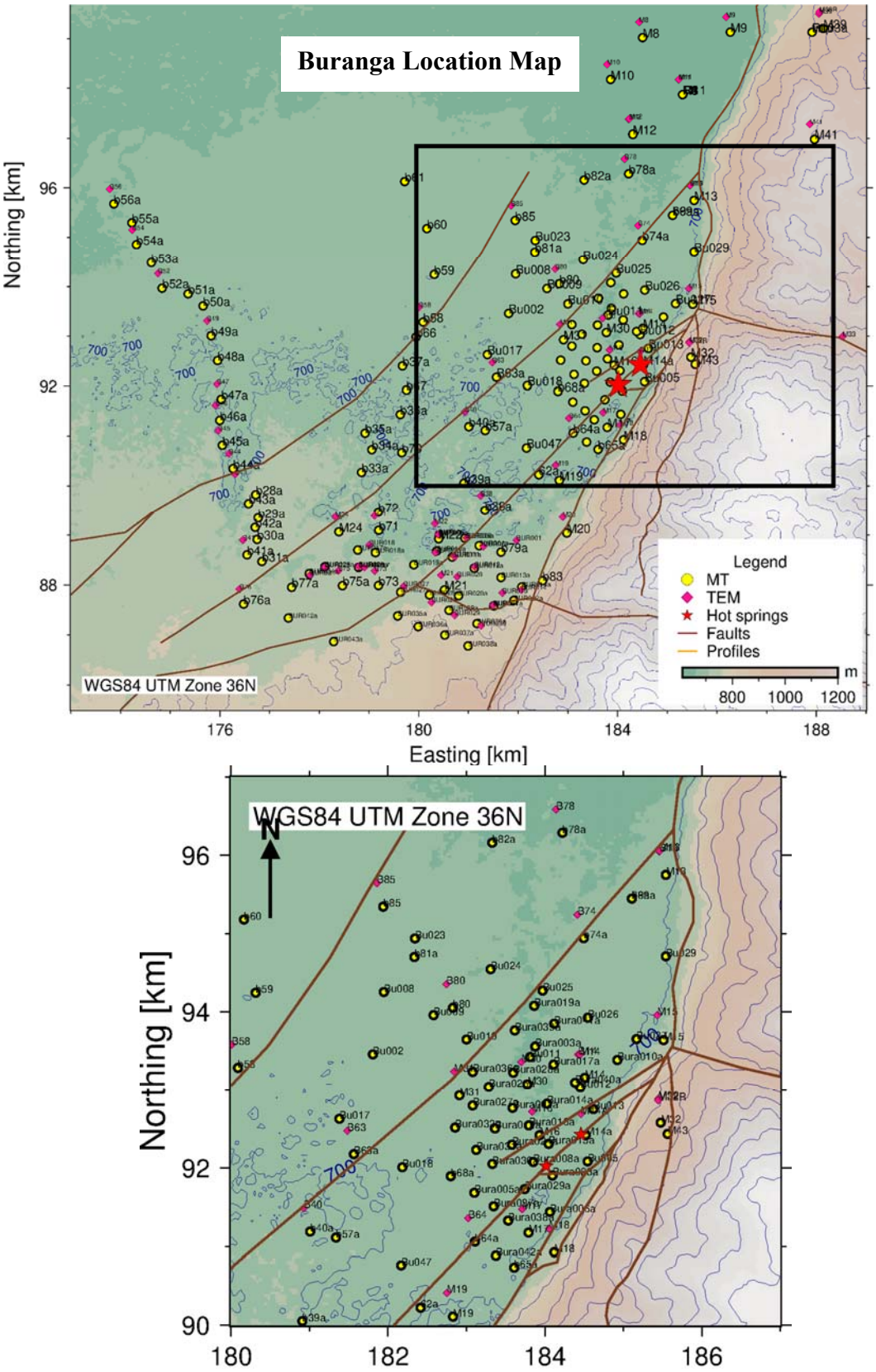

Figure 7.5: Location map of the MT (yellow dots) and TEM (pink diamonds) stations at Buranga geothermal prospect. The black square in the top figure represents the zoomed in region shown in the lower map.

Vozoff (1991) describes the Fast Fourier transformation (FFT) of each of the five recorded field components to yield phase and quadrature values for each component at as many frequencies as there are samples. This transformation helps to estimate the electromagnetic response functions. A detailed derivation of the electromagnetic response functions from time series to frequency domain through Fast Fourier transformation using the auto and cross spectra is given in (Vozoff, 1991).

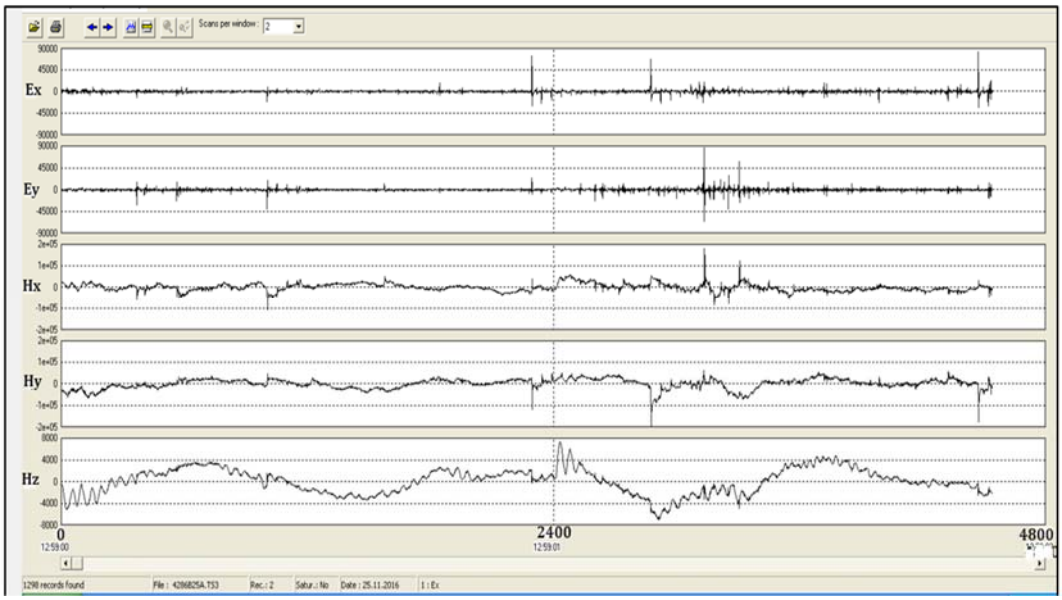

Figure 7.6: *Synchro time series view of data collected on 25-11-2016 displaying the two electric channels E_x and E_y and the three magnetic channels H_x, H_y, and H_z.*

After performing the Fourier transformation, a correction is applied to the resulting spectrum of each data channel. This correction accounts for the absolute complex frequency response of the instrumentation used for that particular channel. The purpose of this correction is to obtain the true spectra of the electric and magnetic fields. Each of these corrected spectra can be represented in terms of their equivalent magnitude and phase, which appear as smooth functions when plotted on a logarithmic frequency scale. Since the Fast Fourier Transform (FFT) algorithm generates more frequencies than are typically required for interpretation, the impedance values are averaged over adjoining frequency windows or bands. The key tools used in this band (or window) averaging procedure are the auto spectra and cross spectra of the data.

While solving for the electromagnetic transfer functions (impedance equations, 5.33a-5.33b) over an averaging band using the auto and cross spectra, there is an inherent problem of the biasing effect of noise through the auto powers. Generally, the MT signals are coherent over a given region, but the signals and noise are incoherent since noise is random, then the auto power estimates will be biased upwards and the impedance response functions (i.e., $Z_{xx}, Z_{xy}, Z_{yx}, Z_{yy}$) that contain auto powers will also suffer the bias error (Vozoff, 1991). To help compensate for the noise, the remote reference method has been recommended.

During the Fast Fourier transformation, the average cross and auto powers, which are products of the field components, and their complex conjugates were calculated for both high (MTH) and low (MTL) frequencies using either robust or non-robust processing.

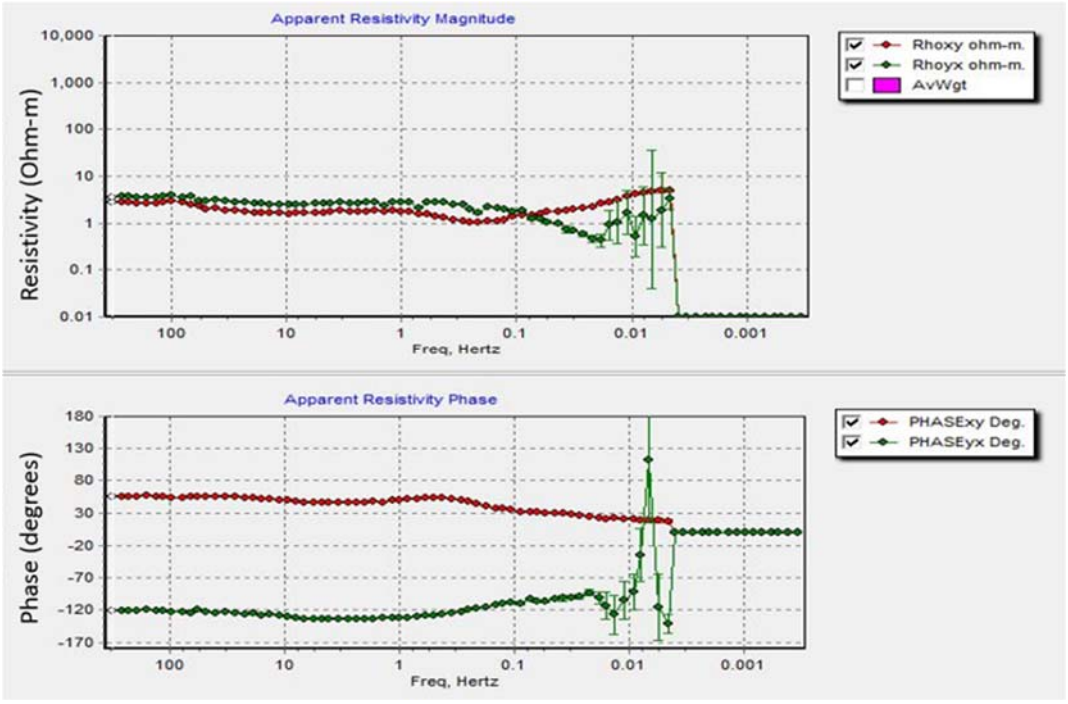

Figure 7.7: Apparent resistivity and phase curves obtained from masking noisy data points and removing outliers from the cross-power segments using the MTeditor program. (Red curve corresponds to the XY apparent resistivity and phase, green curve corresponds to the YX apparent resistivity and phase)

Using the MTeditor software (Phoenix, 2005), the MTH and MTL files are edited (discarding outliers) to evaluate apparent resistivity and phase until satisfactory smooth data curves are obtained see (Figure 7.7). The editing was done by masking noisy sections of the curves and outlying data points and finally exported as Electromagnetic data interchange (*.edi) files ready for the next step, which is 1D inversion using TEMTD software.

The *.edi files are further handled in the Linux environment where MT parameters are calculated from the spectral matrix such as impedance rotational angles, tipper, phase, apparent resistivity, Z-strike, ellipticity, t-strike, skew and coherency (Figure 7.8).

Apparent resistivity curves are plotted in the apparent resistivity panel on the top left in Figure 7.8. This helps to get a first impression of the subsurface resistivity. The

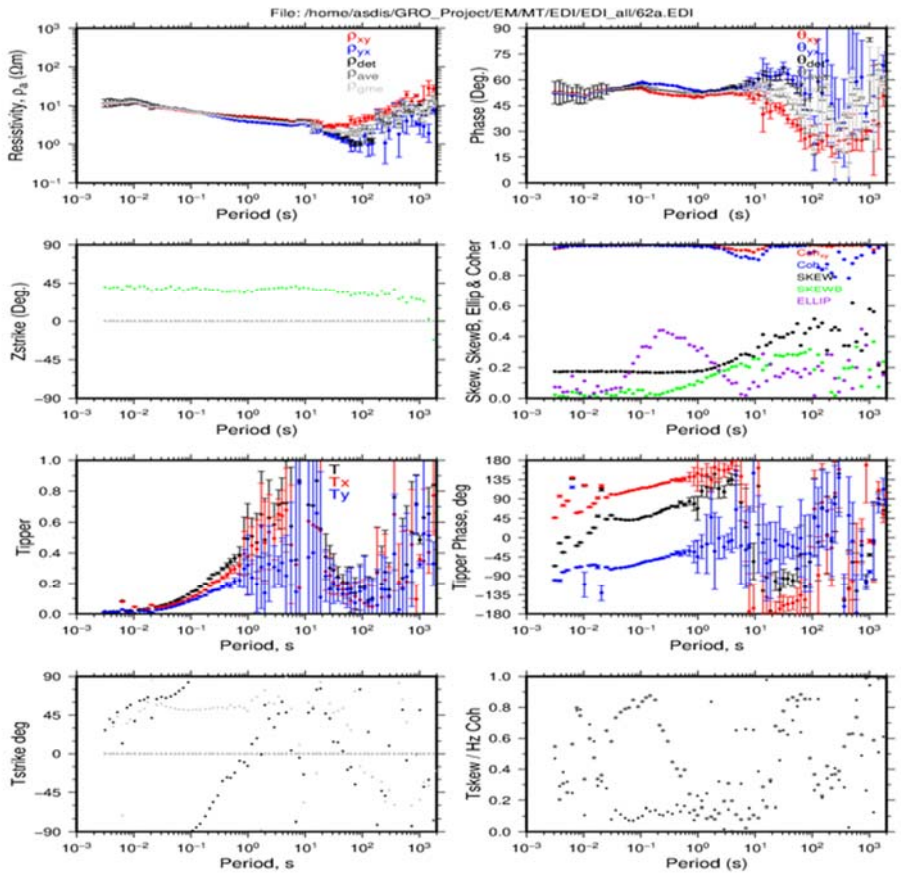

*Figure 7.8: Graphical representation of calculated parameters from the *.edi spectral matrix of MT stations 62a and b35a in panels A and B, respectively. The curves represent the XY and YX data, respectively, as well as the det, ave and gme data (see Section 5.3.3).*

dimensionality of the resistivity structure and strike is indicated by Z-strike and Skew.

7.4 1D Joint inversion of MT and TEM Data

7.4.1 1D inversion programs

To obtain a model of the subsurface resistivity structure, MT responses need to be analyzed by using either forward or inverse algorithms. Forward modelling involves calculating the data (data response) from a given resistivity structure. In inverse modelling, the forward model is used to simulate how different subsurface scenarios would produce observed data. The simulated data are compared with the actual measured data, adjusting the subsurface model iteratively until the simulated data closely match the observed data. This iterative process helps to refine and improve the understanding of the subsurface resistivity being investigated. So, in essence, inversion involves running the forward model in reverse to deduce the properties of the subsurface from the observed data.

This section discusses the inversion codes used in the 2D and 1D joint inversion of apparent resistivity and phase data from the Buranga geothermal prospect. For the 1D inversion, the data were inverted for the XY and YX data as well as the rotationally invariant determinant and average, using the TEMTD inversion program (Árnason, 2006a). GeoTools software was also used to perform 1D inversion for comparison with the 1D results of TEMTD. 2D inversion of MT data rotated 45º clockwise from the north was performed using GeoTools.

7.4.2 TEMTD inversion program

The inversion algorithm implemented in this program is the Levenberg-Marquardt non-linear least square inversion. The misfit function is the root mean square difference between measured and calculated values (chisq), weighted by the standard deviation of the measured values (Árnason, 2006a). Models can be kept smooth for both resistivity variations between layers and layer thicknesses. Damping factors can be imposed on the first and second derivatives to counteract sharp steps in the model and oscillations in the model values, respectively, the 1D inversion of TEM data using TEMTD consists of minimizing the potential function;

The TEMTD program employs the Levenberg-Marquardt non-linear least squares inversion algorithm for data inversion. The misfit function being minimized is the root mean square difference between the measured and calculated values (chisq), weighted by the standard deviation of the measured values (Árnason, 2006a). To keep the resulting models smooth, constraints can be imposed on both the resistivity variations between layers and the layer thicknesses. Damping factors can be applied to the first and second derivatives of the model parameters. This helps to counteract the formation of sharp steps in the model and oscillations in the model values.

In summary, the 1D inversion of Transient Electromagnetic data using the TEMTD program involves minimizing a potential function

$$Pot = \chi^2 + \alpha DS1 + \beta DS2 + \gamma DD1 + \delta DD2 \quad (7.1)$$

Where; chisq= The root mean square difference between measured and calculated values

DS1 = First-order derivative of log conductivities in the layered model

DS2 = Second-order derivative of log conductivities in the layered model

DD1 = First-order derivatives of the logarithms of the ratios of layer depths.

DD2 = Second-order derivatives of the logarithms of the ratios of layer depths

Coefficients α, β, γ and δ are the relative contributions of the different damping terms and are specified by the user.

The TEMTD program is capable of inverting TEM and MT data separately or jointly by either performing standard layered inversion or Occam's smooth inversion (minimum structure). The forward MT algorithm in TEMTD is the standard complex impedance 1D

recursion algorithm while the inverse algorithm is the Levenberg-Marquardt non-linear least square inversion (Árnason, 2006a) which is a robust inversion scheme with an almost certain convergency rate. It is called a non-linear inversion algorithm because the model response is non-linearly dependent on the model parameters. Considering the non-linear problem under Occam's smooth inversion, the data misfit equation is given as

$$\chi^2 = ||\boldsymbol{Wd} - \boldsymbol{WF}[\boldsymbol{m}]||^2 \quad (7.3)$$

which is a measure of the misfit between the measured and calculated data.

Where;

W is a weighting diagonal matrix of the associated data uncertainties,

d is measured data,

F[m] is the calculated model.

|| || denotes the usual Euclidean norm.

The goal is to get a minimum acceptable χ^2 value by finding a model F[m] that fits the observed data. This is done by finding a model of the smallest roughness with the specified misfit and systematically reducing the size of the change in the model from one iteration to the next (Constable et al., 1987). MT inversions produce non-unique solutions hence the preferred model would be the smoothest model that fits the data without including features which are not suggested by the data.

7.4.3 A 1D inversion of MT data

In a 1D environment, the MT impedance tensor reduces to $\boldsymbol{Z} = \begin{bmatrix} 0 & Z \\ -Z & 0 \end{bmatrix}$ and the three invariants reduce to the same scalar number, as described in Chapter 5.4.1. However, the resistivity structure of the Earth is rarely perfectly layered due to the complex nature of the geological environments and noise sources. Therefore, the on-diagonal components of the impedance tensor are non-zero for most geological settings.

If the environment is strictly 2D, then the determinant and the geometric mean would reduce to the same scaler value, while the arithmetic mean would be different. For 3D structures, all the impedance elements would be different. It is, therefore, not easy to decide which invariant parameter to use for characterizing the resistivity structure of the area. The determinant and arithmetic mean usually yield the same structures in most cases (Park & Livelybrooks, 1989) examples are given in Figures 7.9a and 7.9b. The rotationally dependent and independent variants were calculated and plotted for all the stations at Buranga, and some examples are shown below (Figure 7.9a & b). It can be observed that the apparent resistivity and phase curves (ρ_{xy} *and* ρ_{yx}) at station b80 and b82a in panel (c) and (b), respectively, diverge at periods greater than 1 s. Non-1D resistivity patterns can be detected by the non-parallel divergence of the apparent resistivity and phase curves for periods above 1s.

Stations b76a and BUR014a in Figure 7.9a panel (a) and Figure 7.9b panel (d), respectively, show a wide separation between the parallel ρ_{xy} *and* ρ_{yx} resistivity curves at periods below 1s (See Figure 7.5 for station locations). This is an indication of a static shift at those stations. However, the phase does not separate or diverge below 1 s since it is not affected by near-surface distortions. Separation of the apparent resistivity curves beyond 1 s is attributed to the change in dimensionality from a simple 1D structure to 2D or even 3D.

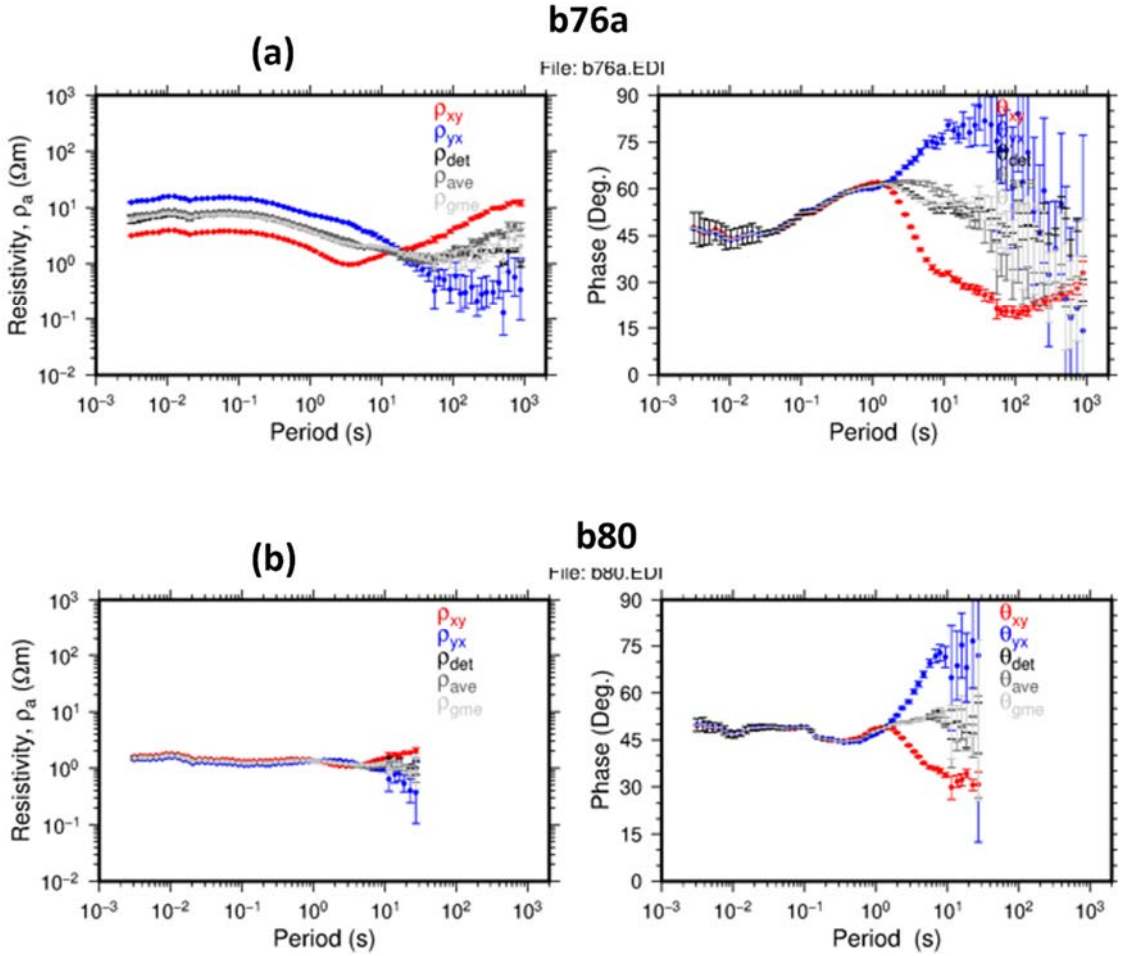

Figure 7.9a: Apparent resistivity and phase curves for the calculated rotationally variant and invariant impedance parameters of station b76a and b80.

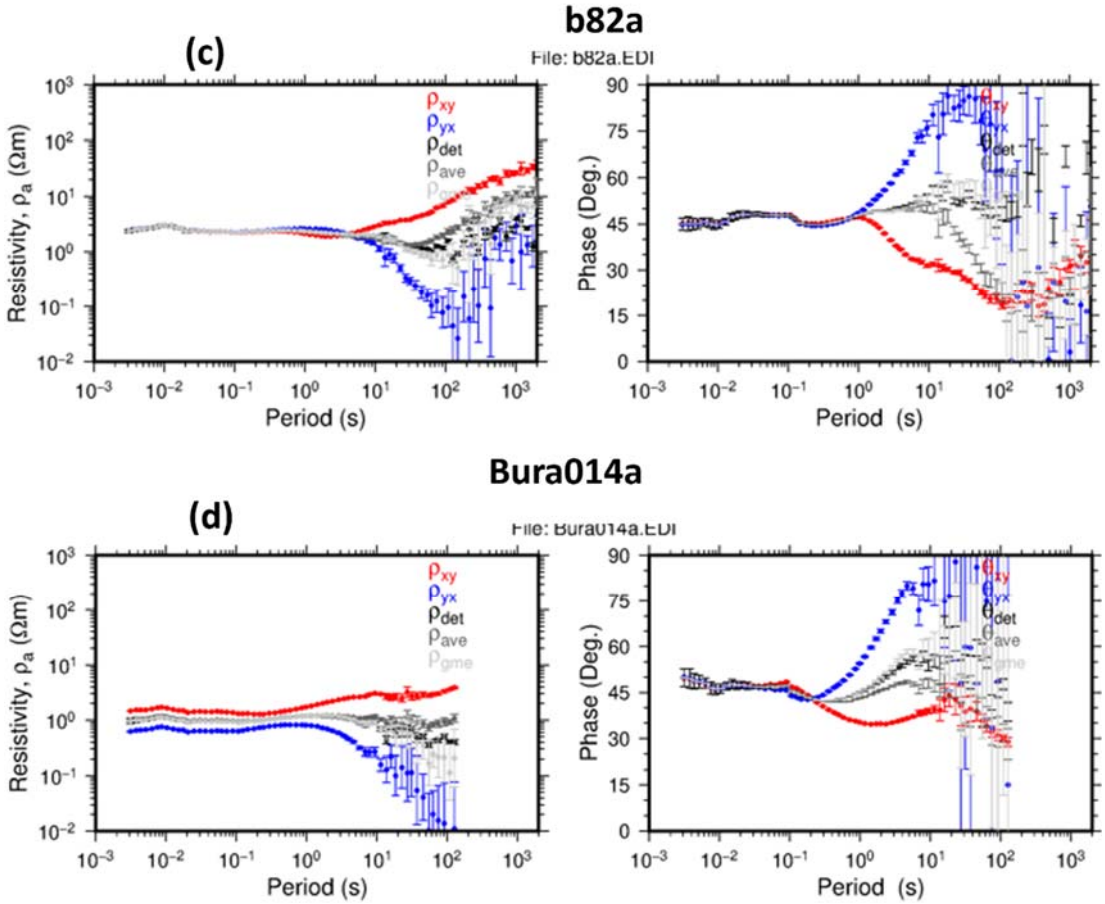

Figure 7.10b: Apparent resistivity and phase curves for the calculated rotationally variant and invariant impedance parameters of station b82a and Bura014a.

1D joint inversion of MT and TEM data was carried out for co-located MT and TEM stations to correct for static shift as discussed in Chapter 6.1. During the 1D inversion, a static shift multiplier is calculated to tie in the MT and TEM data and come up with a single resistivity model for both datasets as shown in Figure 7.10

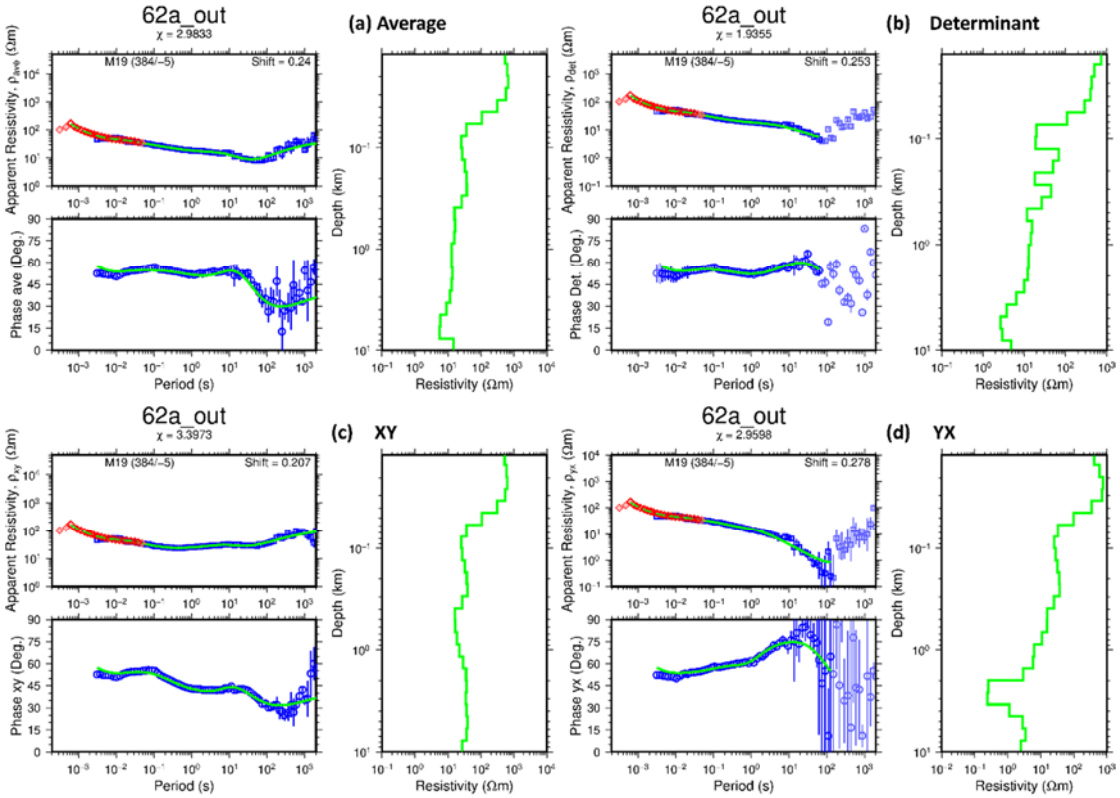

Figure 7.11: Results of 1D joint inversion of TEM and MT data at station 62a. In panels A, B, C and D, the plots show the measured MT data (resistivity as blue squares) and (phase as blue circles) together with the predicted phase and apparent resistivity (solid green). The 1D Occam inversion model (right) and the co-located TEM curve (red diamonds) with the predicted TEM data as green dashed lines. The static shift multiplier is shown in the upper right-hand corner while the chisq value is shown at the top of each plot below the station name. The average, determinant, xy and yx impedance parameters are plotted in A, B, C and D, respectively.

From the joint inversion of the co-located MT and TEM stations, it is observed that most of the MT stations have static shift factors below 1 implying that they were shifted downwards for all the computed MT invariant parameters (Figure 7.11). Without static shift correction, the observed apparent resistivity would give an impression of a very high conductivity structure at Buranga than what it is. Therefore, static shift correction is important in giving a more realistic apparent resistivity structure of the area.

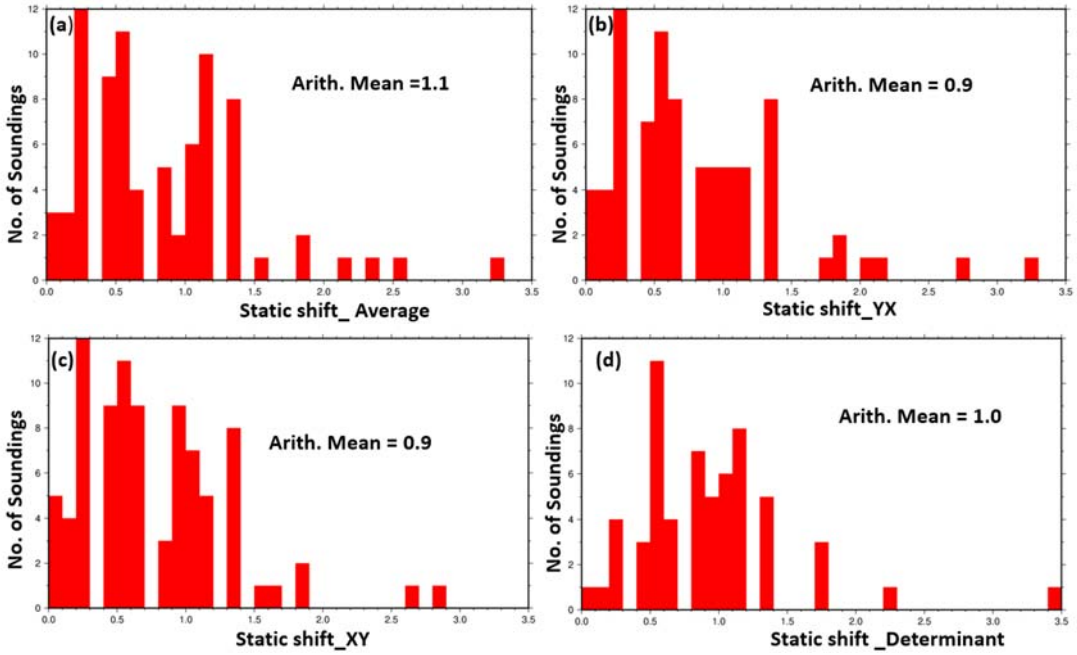

Figure 7.12: *Static shift histograms from the (a) average,(b) XY (c) YX and (d) determinant parameters. The arithmetic mean of the static shift multipliers from each impedance parameter is shown in each panel.*

7.5 2D MT Inversion

To characterize the subsurface resistivity structure of an area, observed MT data should be inverted through an iterative process aimed at obtaining a resistivity model whose predicted response matches the observed data within acceptable limits. It is important to model MT data for the true dimensionality represented by the resistivity response of the acquired data to avoid misinterpretation that arises from, say, modelling 3D data as 1D or 2D or modelling 2D data as 1D. Although 1D inversion has been the most common form of interpretation of MT data since the early development of the MT method, it has been common practice for the last couple of decades to compare the 1D results with either 2D or 3D inversion results and see how reproduceable the 1D results can be. Inversion models are non-unique since several resistivity models can be generated to fit the observed data closely or equally well. On some occasions, it is important to constrain the models with other geologic and drilling information if available.

2D inversion for the Buranga MT data set was done using the GeoTools inversion code developed by Randall Mackie for the former "Compagnie Générale de Geophysique," now known as CGG (CGG Multiphysics, 2019). The code is capable of inverting for the TE and

TM apparent resistivity and phase jointly or separately. In addition, the code can also invert for the vertical magnetic transfer function if present from the H_z magnetic sensor.

7.5.1 2D Inversion code

The GeoTools 2D MT inversion code is based on Tikhonov regularization (Tikhonov & Arsenin, 1977) in which a regularized inversion model that fits the available data within the acceptable errors is sought. The regularization is of the minimum structure model.

According to Rodie & Mackie (2001), the inverse problem can be formulated as

$$\boldsymbol{d} = F(\boldsymbol{m}) + \boldsymbol{e} \tag{7.4}$$

where;

e is a vector of the data uncertainties (errors),

d= [d_1, d_2, …d_N] is a data vector containing N observed data, with each d_i being either the log amplitude or the phase of apparent resistivity for a particular polarization, observation site and frequency.

m= [m_1, m_2,…m_M] is a model vector with M resistivity blocks with each m_j being the logarithm of resistivity for each block.

The inverse problem is solved in the sense of Tikhonov regularization and using the non-linear conjugate gradient (NLCG) algorithm (Rodi & Mackie, 2001) to minimize the non-linear objective function:

$$\Psi(\boldsymbol{m}) = \big(\boldsymbol{d} - F(\boldsymbol{m})\big)^T \boldsymbol{V}^{-1}\big(\boldsymbol{d} - F(\boldsymbol{m})\big) + \tau_1 \boldsymbol{m}^T \boldsymbol{L}^T \boldsymbol{L}\boldsymbol{m} + \tau_2 (\boldsymbol{m} - \boldsymbol{m}_o)^T \boldsymbol{D} (\boldsymbol{m} - \boldsymbol{m}_o) \tag{7.5}$$

Where,

V is a positive definite matrix that gives the variance of the error vector (diagonal covariance matrix), **D** is a diagonal weighting matrix, **L** is the approximation to the depth weighted Laplacian, d is the observed data, m is the model vector, F(**m**) is the model response, $\boldsymbol{m}_o$ is the prior model, τ_1 and τ_2 are smoothing and a priori weights that control model roughness and variations from the a priori model, respectively.

In Equation 7.5, the first term represents the squared L-2 norm of the weighted residuals (data misfit functional), the second term represents the L-2 norm of the model roughness, and the third term is the squared L-2 norm of the variations away from the a priori model. The last two terms can be thought of as the model structure stabilizing functional.

The NLCG algorithm of Rodi & Mackie (2001) is based on the Polak-Ribiere (Polak, 1971) variant of non-linear conjugate gradients in which the model sequence is determined by a sequence of univariate minimizations or line searches along computed search directions. The modifications to the Polak-Ribiere variant of NLCG by Rodi and Mackie which are indeed implemented in GeoTools are that,

(i) At every iteration, the software keeps track of the best (smallest non-linear objective

functional $\Psi(m)$ model encountered.

(ii) If the univariate function to be minimised increases during the iteration, then the next step size is calculated by bisection of the previous step size and the best step size.

(iii) If on the second or later steps of a line search, the current and previous best models constitute a minimum, then the next step size is calculated in a way yielding the local minimum of a cubic approximation to the univariate function to be minimized.

The inversion is said to converge when the estimated value of the objective function for the next step size is in agreement with the univariate function to be minimized for that step size within some prescribed tolerance (Rodi & Mackie, 2001).

To perform 2D inversion, forward solutions to several hundreds of 2D MT solutions are required and, therefore, GeoTools uses a finite difference 2D MT forward modelling algorithm based on the network analogue to Maxwell's equations. The mesh grid consists of 2D rectangular blocks of varying dimensions with a constant resistivity and an air layer at the top of the earth model. Electric fields are eliminated for the TM decoupled to yield a second-order system of equations for H_x. Similarly, the magnetic fields are eliminated for the TE decoupled mode to yield a second-order system of equations for E_x. The resulting second-order systems of equations are then solved using the sparse matrix (PARDISO) (CGG Multiphysics, 2019) solver which is fast and efficient. Calculating the electric and magnetic fields anywhere within the model is then possible.

8 Results, Analysis and Discussions

8.1 Dimensionality analysis

Phase Tensors

Phase tensor ellipses were plotted to investigate the dimensionality of the data at Buranga for different periods (and consequently estimated depths) according to a method by Caldwell et al. (2004) using GeoTools software. For periods between 0.01 s - 0.1 s (Figure 8.1 (a)), which corresponds to the shallow parts of the survey area, the phase ellipses are indistinguishable from perfect circles having equal radii. This is an indication of an isotropic and 1D conductivity structure with the radius of the circles dependent on the variation of the conductivity with depth.

For periods between 10 -100 s (Figure 8.1(b), (c) and (d)), the phase tensors take on an elliptical shape with the orientation of the major axis being aligned parallel to the main geological structures in the area probably controlling the (regional) conductivity distribution. In addition, Lake Albert is located just 50-60 km NE of Buranga with its waters having an electrical conductivity of 129.2 to 984 μS cm−1 (Kaddumukasa et al., 2012), its effect on the regional conductivity cannot be overlooked. This is an indication of a 2D conductivity structure starting from periods of 10 seconds and onwards.

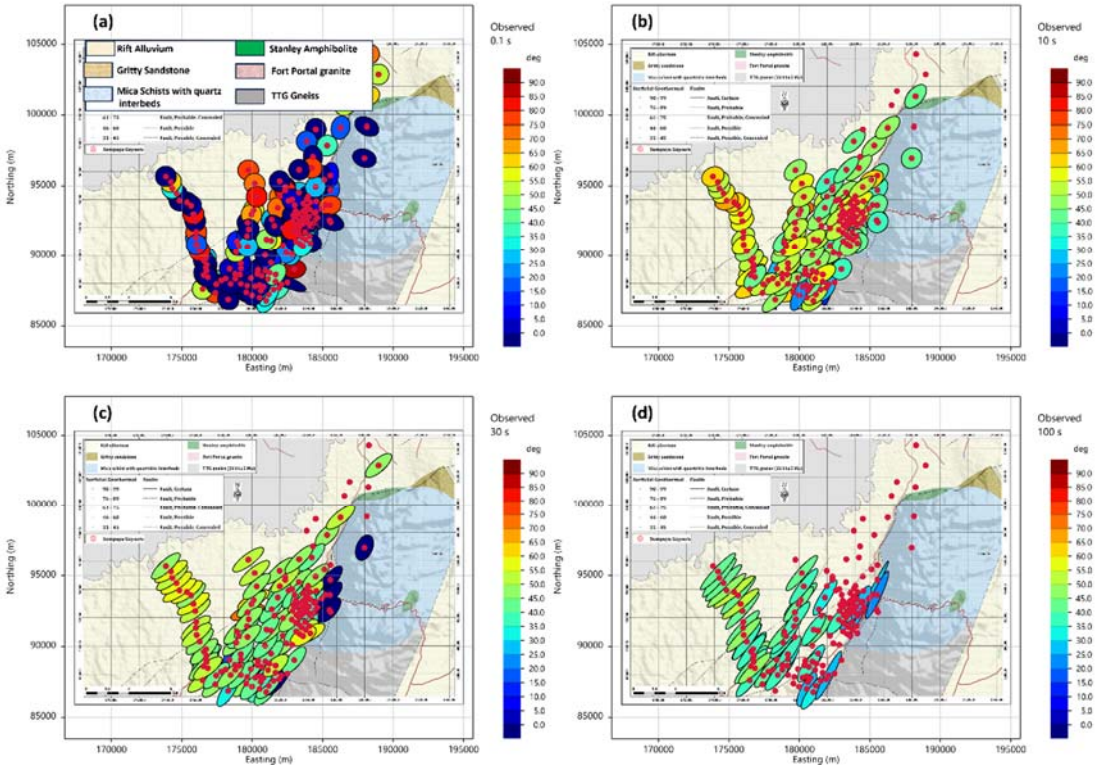

Figure 8.1: Phase tensor from the Buranga prospect overlain on the geological map of the area. The phase tensor is generated for the periods 0.1 s panel (a), 10 s panel (b), 30 s panel (c) and 100 s panel (d). Tensor ellipse color fill represents the value of $(\alpha - \beta)$ *which is the orientation of the major axis.*

8.2 Directional analysis

During field acquisition, MT data are measured in either geographical or geomagnetic directions. These are rarely the dominant geoelectrical strike directions in the survey area. Therefore, it is paramount to carry out directional analysis before inversion and a meaningful interpretation of the data. Strike direction analysis helps to determine the directions of resistivity contrasts that can be used to infer geological features such as faults which are not necessarily visible on the surface. As discussed in chapter 5.4. strike analysis was performed for the Buranga data set. The resulting Z-strike and T-strike maps are presented and discussed below.

Z-strike analysis of the Buranga MT data shows a non-uniform orientation of strike direction for periods below 1 s (Figure 8.2), whereas strike estimates tend to have a consistent pattern for longer periods (>1 s). For longer periods at the Buranga prospect, the strike direction is aligned NE-SW parallel to the direction of the main Bwamba fault and other secondary faults (Figure 8.3). The strike direction is also in agreement with the orientation of the western rift direction as seen on the geological and topographic maps of the area (Figure 7.5).

There is a scatter in the Z-strike estimates for some MT stations as seen in Figure 8.2 in the southern region and slightly north of the hot springs. The scatter at short periods is probably attributed to the influence of strong local shallow structures at the respective MT sites.

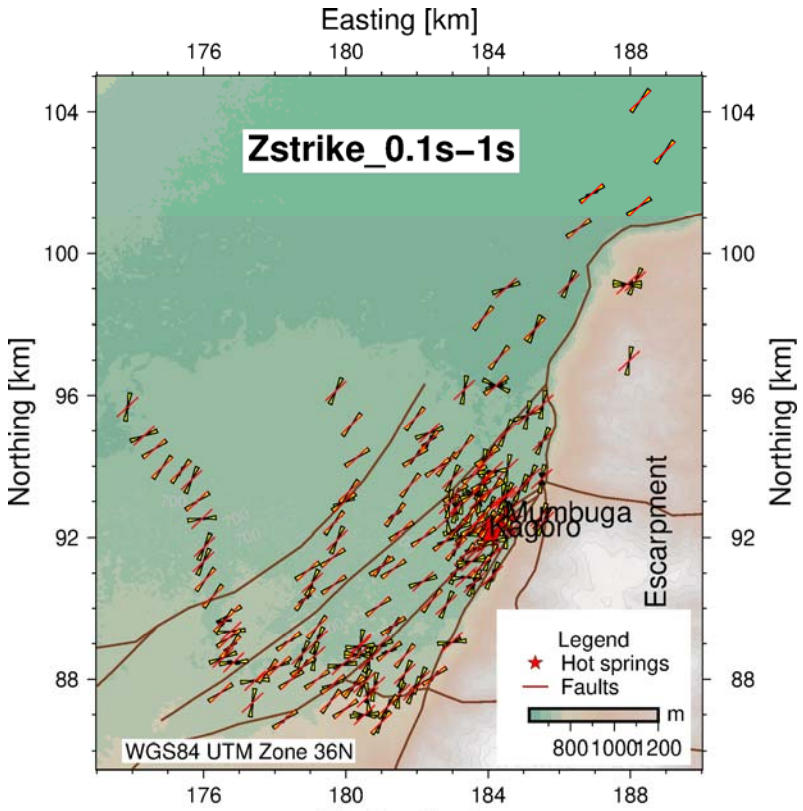

Figure 8.2: Z-strike map for periods between 1-10 s.The strike direction is NE-SW parallel to the major faults within the prospect area.

At higher periods there is a consistent NE-SW strike direction for almost all the stations (Figure 8.3) aligning perfectly parallel to the faults. This is indicative of a controlling structure at depth and that the resistivity varies the least in the NE-SW direction but changes considerably perpendicular to the faults. The dominant electrical strike can be different at varying depths reflecting different structures at different depths. Because of the inherent ambiguity in the Z-strike determination highlighted in chapter 5.4.3, Z-strike cannot solely be used to determine the electrical strike. Therefore, the so-called tipper T, which relates the vertical component of the magnetic field to the two horizontal components is used to compare with the Z-strike as discussed in Chapter 5.4.3 above.

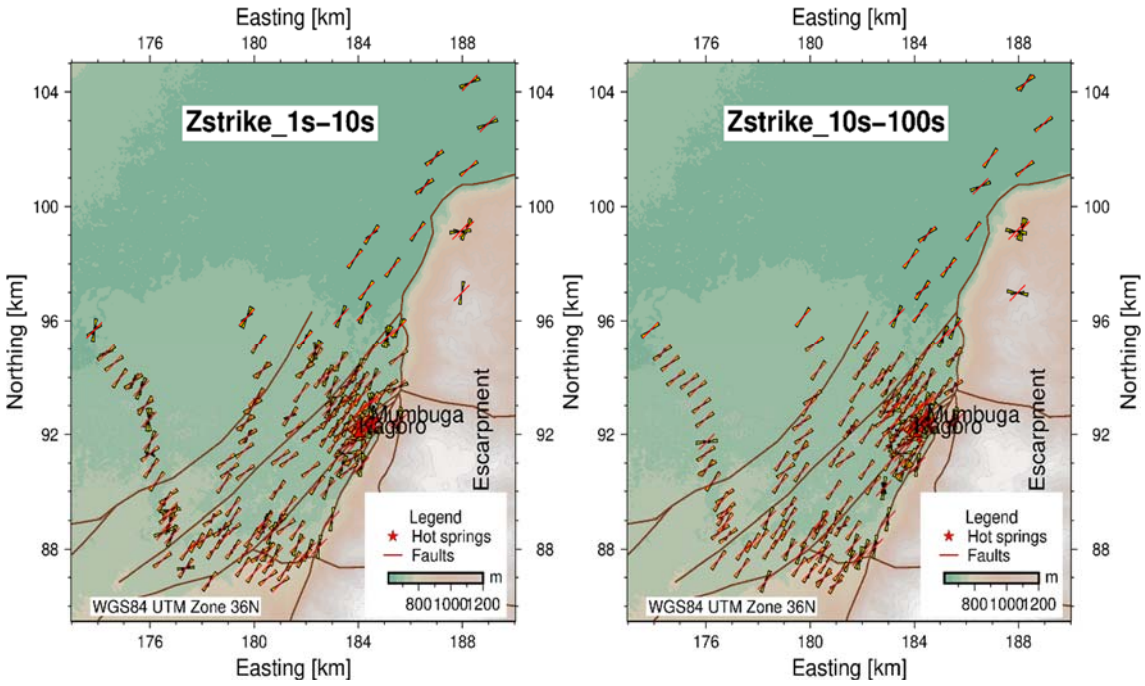

Figure 8.4: Z-strike maps for periods between 1-10 s and 10-100 s.The dominant strike direction is NE-SW parallel to the major faults within the prospect area with a few scatters in the south, north of the hot springs and on the escarpment.

Figure 8.4 shows the T-strike map for periods 1-10 s indicating a general NE-SW direction at the center of the area and a few southwestern and northeastern MT stations displaying some scatter. This is an indication of a more complex geological/resistivity structure at those

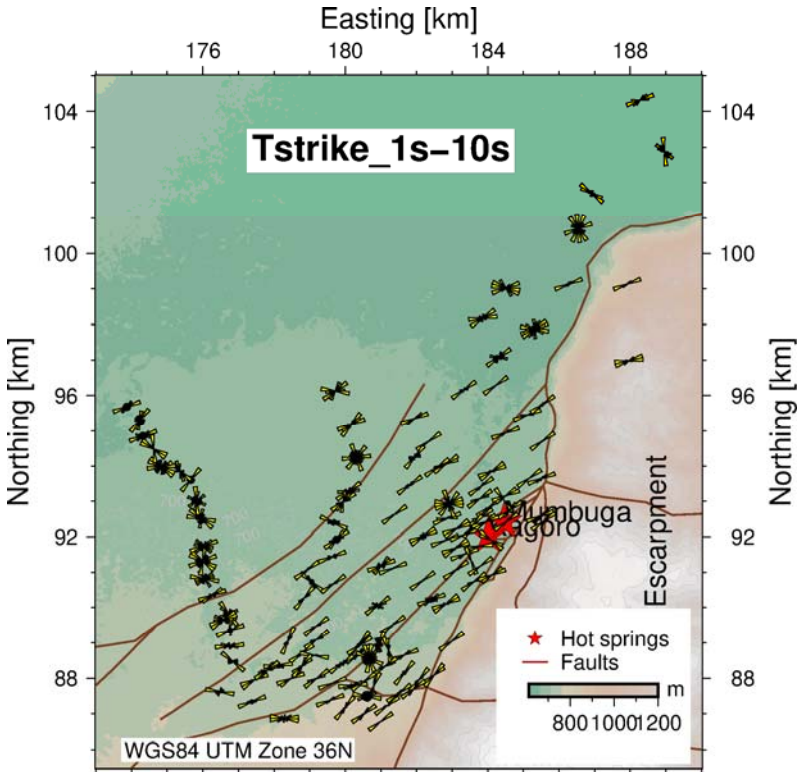

Figure 8.3: T-strike map for periods between 1-10 s.The general strike direction is NE-SW parallel to the major faults within the prospect area.

sites. Generally, we can say that the dominant strike at Buranga is NE-SW direction, and it is due to the deep-seated controlling faults of the western branch of the EARS.

8.3 1D resistivity models from Buranga

1D inversion for the different rotationally invariants (average and determinant) and rotationally variants (XY and YX) was carried out in this study. A total of 165 MT stations were inverted. Out of the 165 MT soundings, 88 had a TEM sounding at the same location and the sounding pair were jointly inverted to correct for static shift in the MT data. The remaining MT stations underwent inversion without the use of any additional data. The minimum structure inversion (Occam) routine was implemented for all the MT stations inverting for both apparent resistivity and phase. Model parameters were defined for the initial automatically generated model, and these were updated accordingly for each station during the inversion process to achieve the best fit with an acceptable chisq (χ^2) value.

Several starting models were tried in the inversion. They had a homogeneous resistivity of 1 -50 Ωm with 30-50 layers. A top layer with a thickness of 15 m and 30,000 m depth to the half-space of the model. Damping parameters were also defined to control the first and second-order derivatives of conductivities. For stations that were inverted jointly with co-located TEM data, initial static shift multipliers were suggested. These are then improved by the inversion until an acceptable multiplier is achieved for both the MT and TEM data. Most MT stations had a static shift factor of less than 1. The model misfit as shown by the (χ^2) value was mostly between 0.5 -2 and two stations with a (χ^2) value of 11.

Inversion results showing the data fit for selected stations for the four cases are shown in Figures 8.5 -8.6.

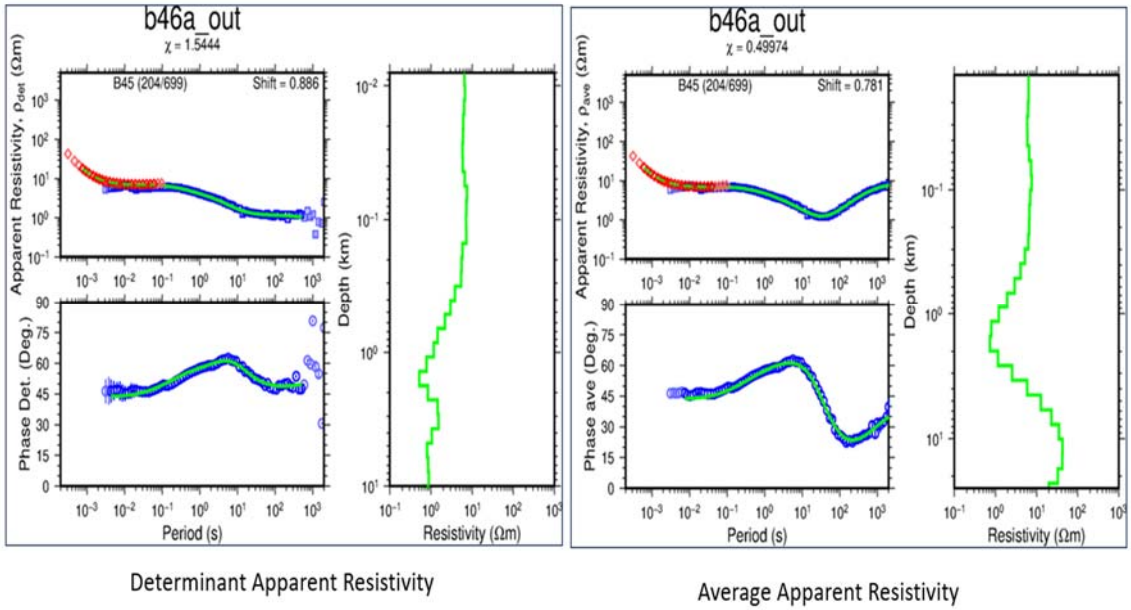

Figure 8.6: Results of 1D joint inversion of TEM and MT data for the rotationally invariant determinant and average for station b46a. The plots show the measured MT data (resistivity as blue squares) and (phase as blue circles) together with the model response phase and apparent resistivity (solid green). The 1D Occam inversion model (right) and the co-located TEM curve (red diamonds) with the predicted TEM data as green dashed lines. The static shift multiplier is shown in the upper right-hand corner while the chisq value is shown at the top of each plot below the station name.

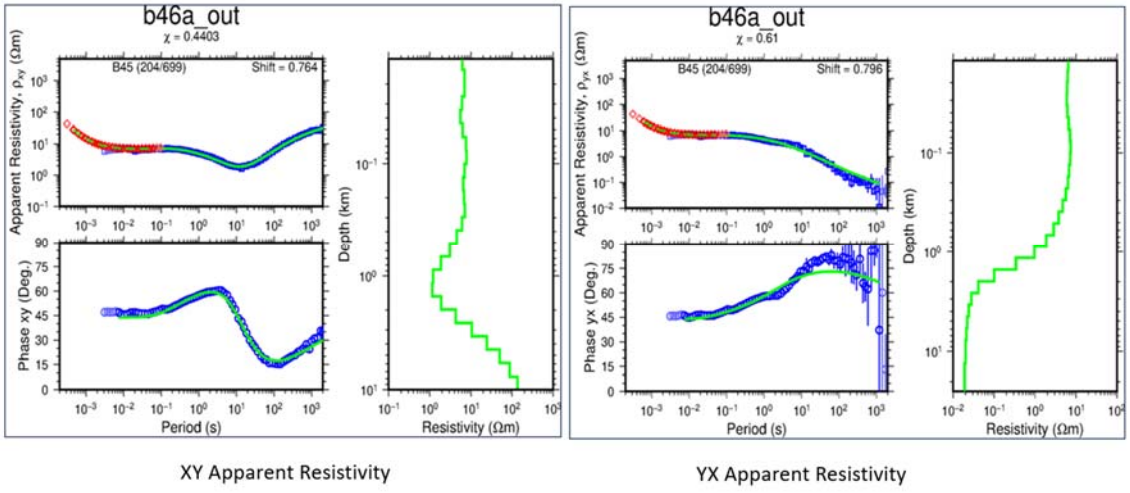

Figure 8.5: *Results of 1D joint inversion of TEM and MT data for the XY and YX apparent resistivity and phase at station b46a. For Figure caption, see Figure 8.5*

Model responses from the average and the XY-derived apparent resistivity and phase showed the best (lowest) χ^2 value. On the other hand, the YX models showed poor data fits especially for the phase. Because of this poor data fit, models generated from this apparent resistivity and phase cannot be trusted at Buranga.

8.4 1D Resistivity Structure at Buranga

To better view the final 1D resistivity models at Buranga, depth slices and resistivity cross sections are generated using the Temresd and Temcross programs respectively, written by Hjálmar Eysteinsson (Eysteinsson, 1998) at Iceland GeoSurvey (ÍSOR). The programs incorporate open-source GMT software to create maps for visualization of the resistivity variations.

8.4.1 Resistivity depth slices

Depth slices were generated from the inversion results of the determinant and average apparent resistivity and phase in addition to the rotationally variant XY and YX apparent resistivity and phase. The resistivity depth slices provide insight into the general lateral variations of the electrical resistivity at different depths below the surface.

Figure 8.7 shows the 1D resistivity structure at 600 m a.sl (50-100 m below the surface)

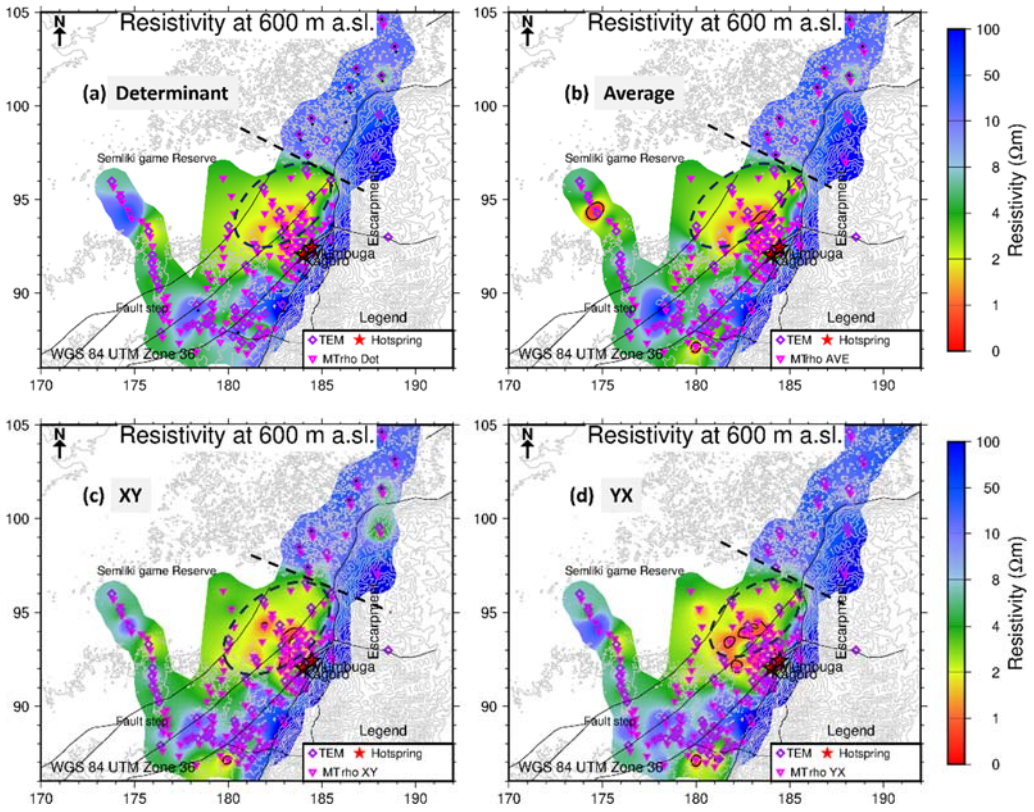

Figure 8.7: Resistivity depth slices at 600 m a.s.l for 1D inversion of the (a) determinant, (b) average (c) XY and (d) YX apparent resistivity and phase. Pink triangles represent the MT stations, and thin black continuous lines are faults.The black dashed oval represents the area extent of surface conductive zones while black dotted line is the inffered fault based on topography and resistivity discontiniuty.

from the four different apparent resistivities and phases. All four exhibit closely the same resistivity structure of a conductive zone of about 2-4 Ωm (marked in black stippled oval) around the hot springs and resistivity >10 Ωm towards the NE with a clearly defined and sharp boundary north of the surface manifestations which might be an indication of a contact

zone probably due to a cross-cutting fault (straight stippled line) trending almost E-W. There is also a high resistivity structure with 10 -100 Ωm in the far east, towards the Rwenzori massif. The similarity depicted by the four depth slices is an indication of a 1D earth at the near-surface.

At 400 m b.sl. (Figure 8.8.) the resistivity maps (a) and (b) for the rotationally invariant determinant and average, respectively, the conductive zone increases in size now covering most of the centre of the prospect area, starting at the border between the massif and the sedimentary plain to the west. This is probably due to the upflow of conductive geothermal waters through the contact zones and spreading out into the sediments along and above the damage zones or fault splays. At about 1 km below the surface (Figure 8.9) the conductive zone with a resistivity of 1-2 Ωm becomes very pronounced and demarcated, starting near the hot spring area and spreading out towards the west indicating thick conductive layers which could be due to out-flow of the system into the sediments. At this depth, the resistivity boundary in the NE and on the Eastern side is still maintained, clearly showing the high resistive Precambrian rocks of the mountain ranges and the conductive sedimentary basin in the graben.

The resistivity structure is somewhat different for the inversion based on the XY and YX

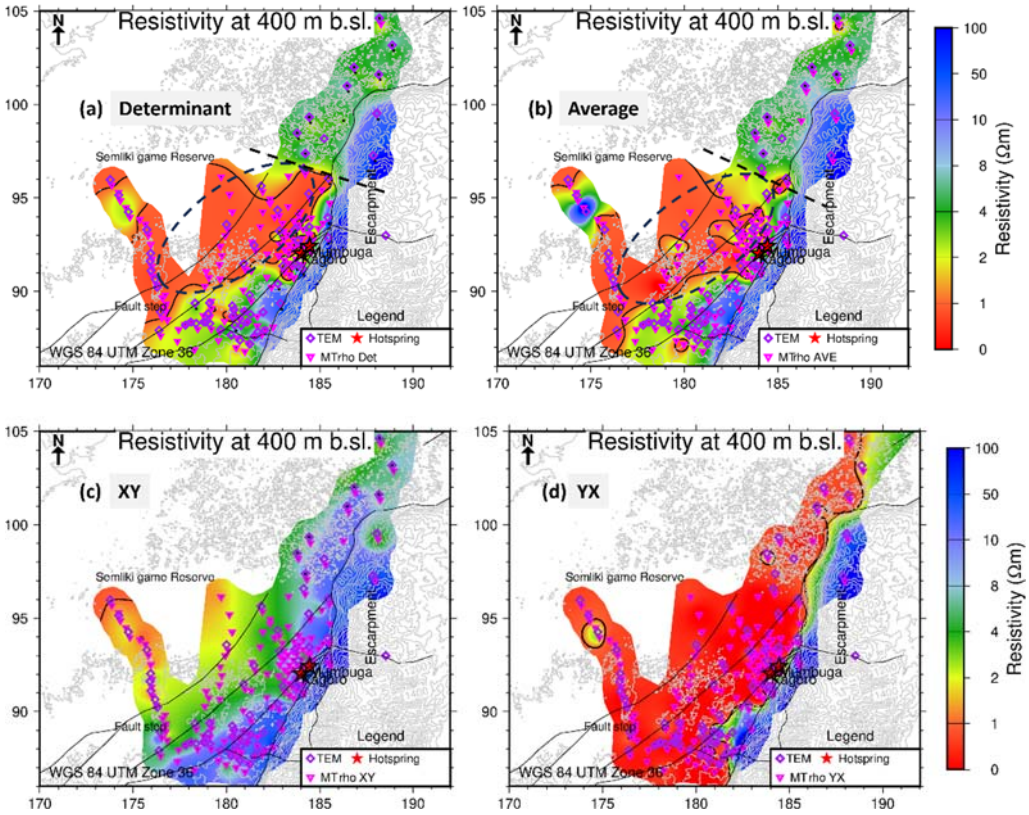

Figure 8.8: *Resistivity depth slices at 400 m b.sl for 1D inversion of the (a) determinant, (b) average (c) XY and (d) YX apparent resistivity and phase. Pink inverted triangles represent the MT stations, and thin black continuous lines are faults. The black dashed oval represents the area extent of conductive zones while the black dotted line is the inffered fault based on topography and resistivity discontiniuty.*

apparent resistivity and phase (Figure 8.9c and d) owing to the influence of 2D structures. The YX is influenced more by the underlying conductive sediments whereas the XY mode

tends to have a higher resistivity compared to the other three models.

Below 1200 m b.sl. the resistivity boundary towards the NE disappears. This might indicate that the controlling structure was shallow. However, the low resistivity structure 0.1-2 Ωm at the centre and westwards of the prospect persists to a depth of over 2500 m b.sl. The boundary between the resistive Precambrian rocks 50 -100 Ωm of the horst at the eastern end and the conductive sedimentary plain is distinctive at all depths.

At 3000 m b.sl. (Figure 8.10) the high conductive sediments at the centre of the prospect start to disappear in resistivity depth slices derived from the determinant, average and XY. The change in resistivity could be attributed to a change from the high conductive sediments of the rift graben to a more resistive layering probably the upper part of the basement rocks. However, the YX depth slice does not show this sort of transition in the resistivity. Since the YX shows a very conductive overall structure, it is possible that it skews the correct resistivity structure and hence should not be used in the interpretation of the subsurface resistivity conditions at Buranga.

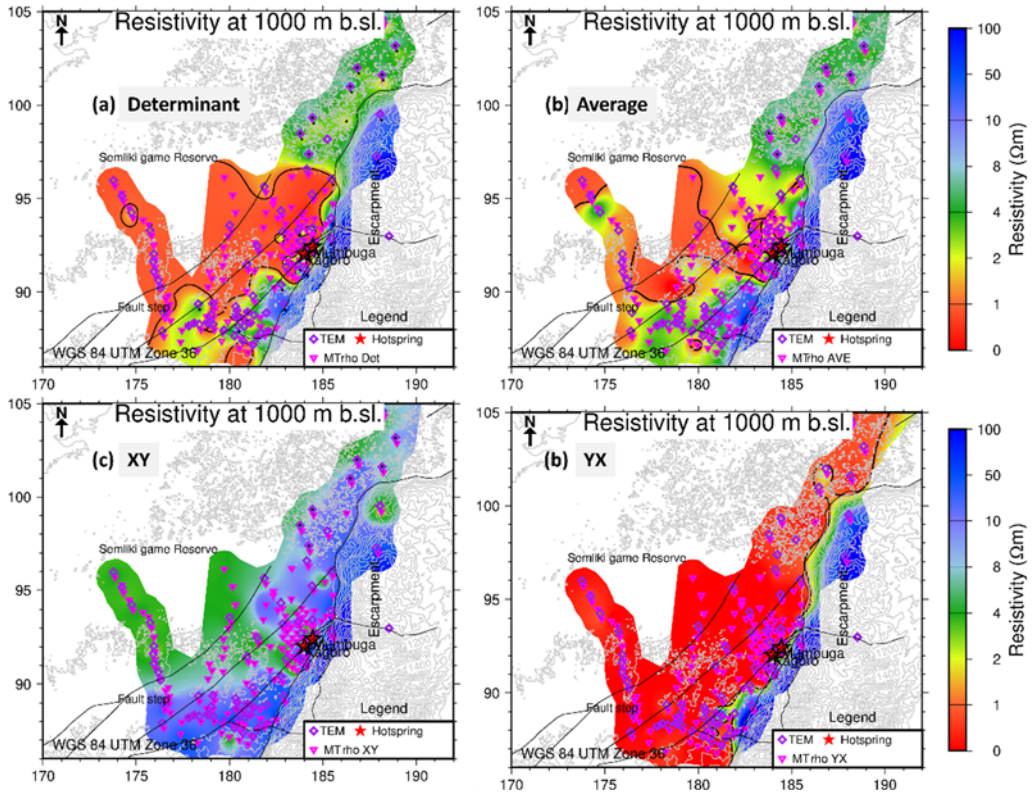

Figure 8.9: *Resistivity depth slices at 1000 m b.sl for 1D inversion of the (a) determinant, (b) average (c) XY and (d) YX apparent resistivity and phase. For Figure caption, see Figure 8.8.*

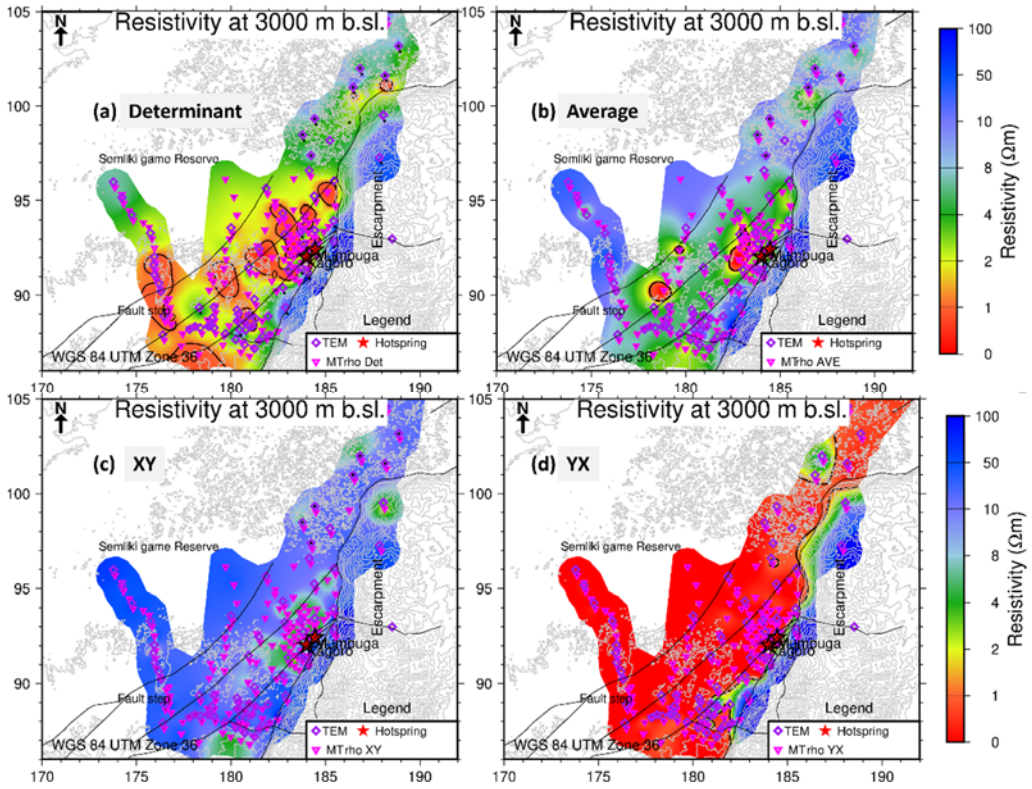

Figure 8.10: *Resistivity depth slices at 3000 m b.sl for 1D inversion of the (a) determinant, (b) average (c) XY and (d) YX apparent resistivity and phase. Pink inverted triangles represent the MT stations, and thin black continuous lines are faults.*

8.4.2 Resistivity cross-sections

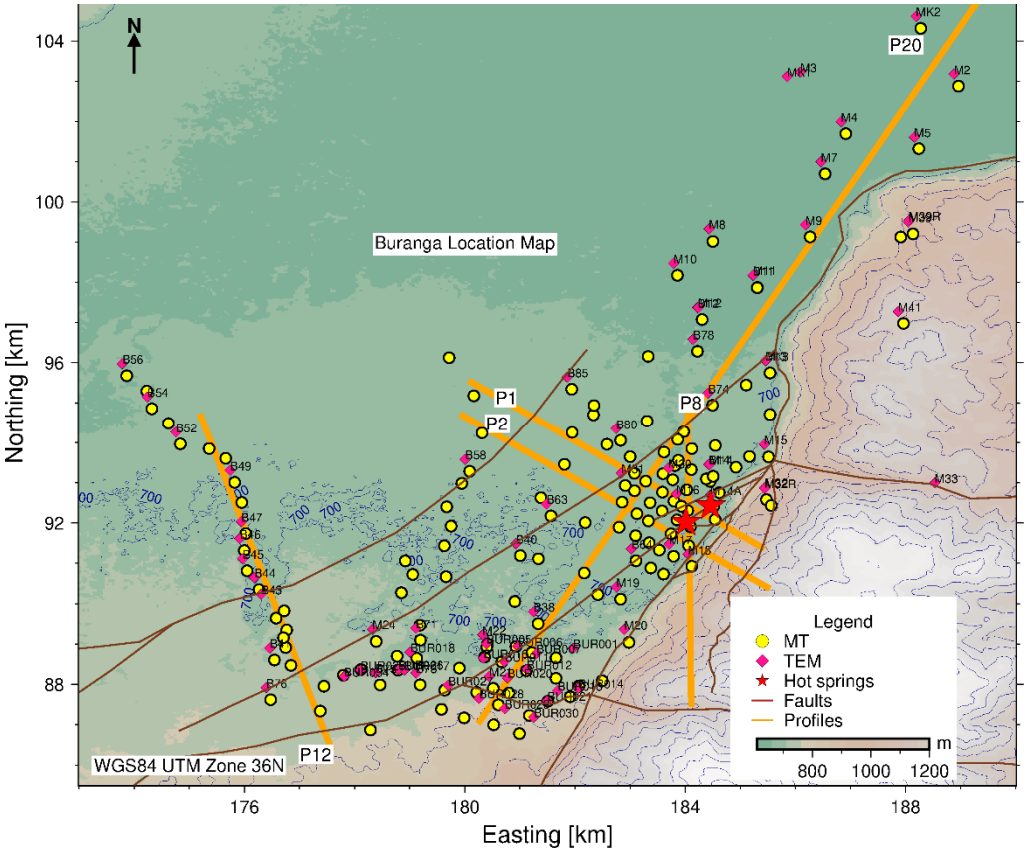

Figure 8.11: Location map of MT and TEM stations in Buranga and the resistivity cross sections presented in this thesis

The Temcross program (Eysteinsson, 1998) was used to create vertical cross-sections based on the 1D inversions. It calculates the best line between selected soundings and plots the resistivity isolines for each sounding on the profile. Most of the cross sections produced are oriented NW-SE perpendicular to the main boarder fault shown in Figure 8.10-8.14. Section 20 (Figure 8.13) was generated to investigate the resistivity boundary observed in depth slices at shallow depths (Figure 8.7, 8.8 (a), (b), and 8.9).

Cross section 1 NW-SE

Cross section 1 runs NW-SE passing near the Mumbuga hot spring area (Figure 8.12).

The cross sections derived from the determinant and the YX apparent resistivity and phase show similar structures i.e., a top relatively conductive layer of about 1-8 Ωm underlain by a more conductive thick conductive layer (rift alluvium/sedimentation) of 0.1 -2 Ωm that extends to a depth of about 7 km b.sl. The XY cross-section is different. It shows a conductive layer of 1-3 Ωm at the surface to a depth of about 1000 m b.sl. A more resistive 10-50 Ωm zone is then encountered starting at a depth of 2-4 km in the NW part of the section. From Figure 8.12, we can see that the XY cross-section is more influenced by the more resistive structures whereas the YX cross-section is more affected by the more conductive structures. Therefore, to avoid this sort of bias and overcompensation of some structures over others, we also generated the resistivity cross-sections from the average MT and determinant rotationally invariant modes for comparison.

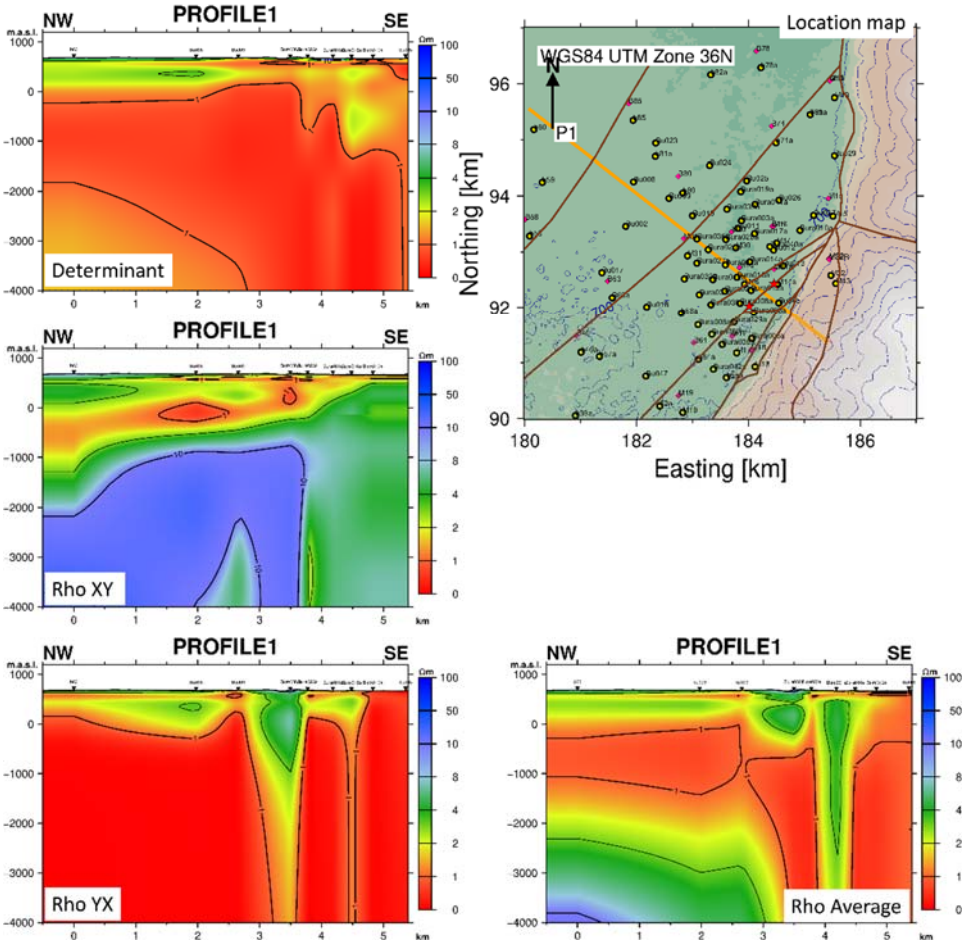

Figure 8.12: *Resistivity cross-sections based on 1D inversion of the determinant, XY, YX and average apparent resistivity and phase. On the top right is a map showing the location of the cross-section. The MT stations on the profile from NW-SW are b60, Bu008, Bu009, Bura036a, Bura025a, Bura001a, Bura016a, Bura015a.*

The average cross-section (Figure 8.12 bottom right) highlights a relatively less conductive layer at the surface from 650 m a.sl to sea level. This is probably caused by the local vegetation and forest cover at the near-surface as well as the topsoil. The next layer of resistivity 0.1- 2 Ωm starts at sea level and reaches about 2 km b.sl probably indicating rift sediments in which geothermal fluids that have been transported upwards within the fault conduits that have now percolated to form the soggy swamps observed within the area.

By visual inspection of the four cross-sections and with prior knowledge about the exposed basement rocks of the Rwenzori massif located on the southeastern end of the profile, XY cross-section seems to be a better representation of the resistivity structure at Buranga since it captures the already known resistive rocks on the southeastern end of the profile and the conductive soggy sediments under the forest canopy in the middle of the prospect area westwards. Subsequent interpretations for the 1D resistivity structure are, therefore based on the XY cross-sections.

Cross section 2 NW-SE

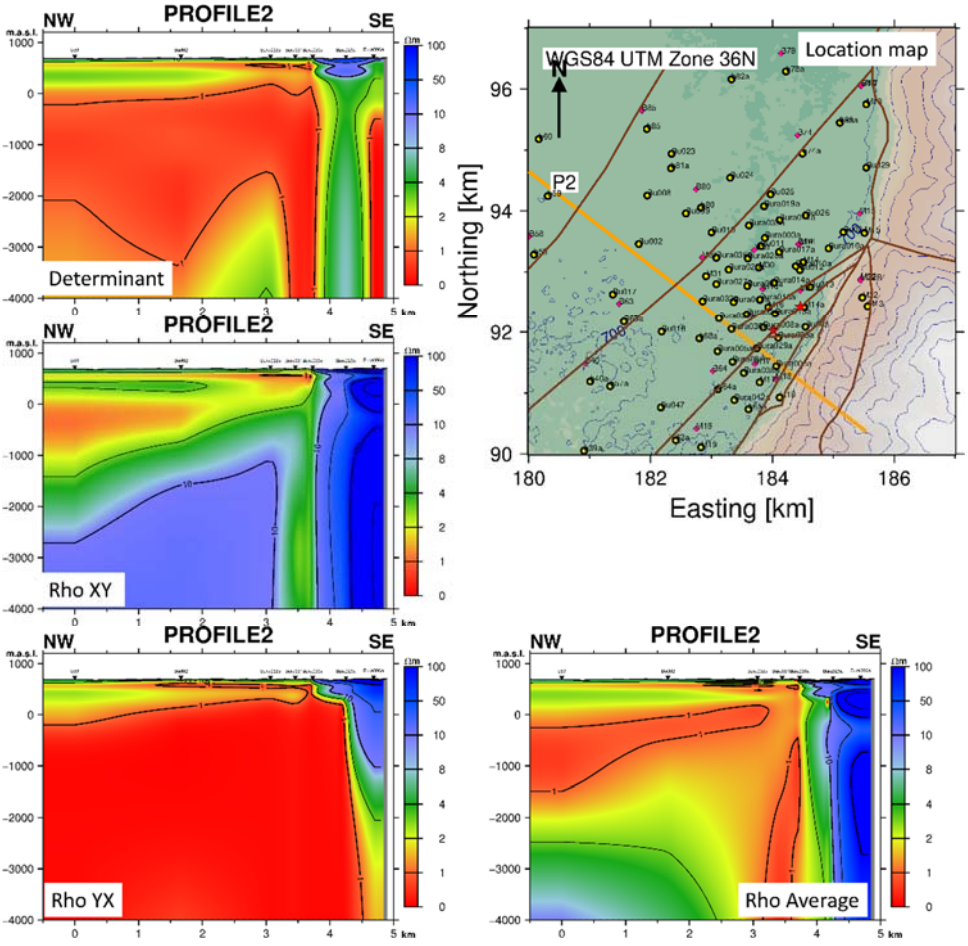

Figure 8.13: *Resistivity cross-sections based on 1D inversion of the determinant, XY, YX and average apparent resistivity and phase. On the top right is a location map showing the location of the cross-section. The MT stations on the profile from NW-SW are b59, Bu002, Bura032a, Bura031a, Bura030a, Bura029a, Bura006a*

Cross-section 2 (Figure 8.13) runs parallel to cross-section 1. It is oriented NW-SE passing near the Nyansimbe hot spring area and it runs through MT stations b59, Bu002, Bura032a, Bura031a, Bura030a, Bura029a and Bura006a. The XY and YX cross sections are more influenced by the high resistivity structures and the low resistivity structures, respectively. The average cross-section exhibits a complementary form of both the XY and YX cross-sections. The XY cross-section shows a highly resistive area furthest in the SE part typical of a Precambrian rock of the Rwenzori massif with a resistivity >50 Ωm. There is a

discontinuity of the resistive zone in the XY cross-section towards the SE part suggesting either an artefact or a possible fault zone around the hot spring area. The presence of the fault zone is confirmed by the surface mapping and geothermal manifestations in the vicinity of station Bura016a.

Cross section 12 NNW-SSE

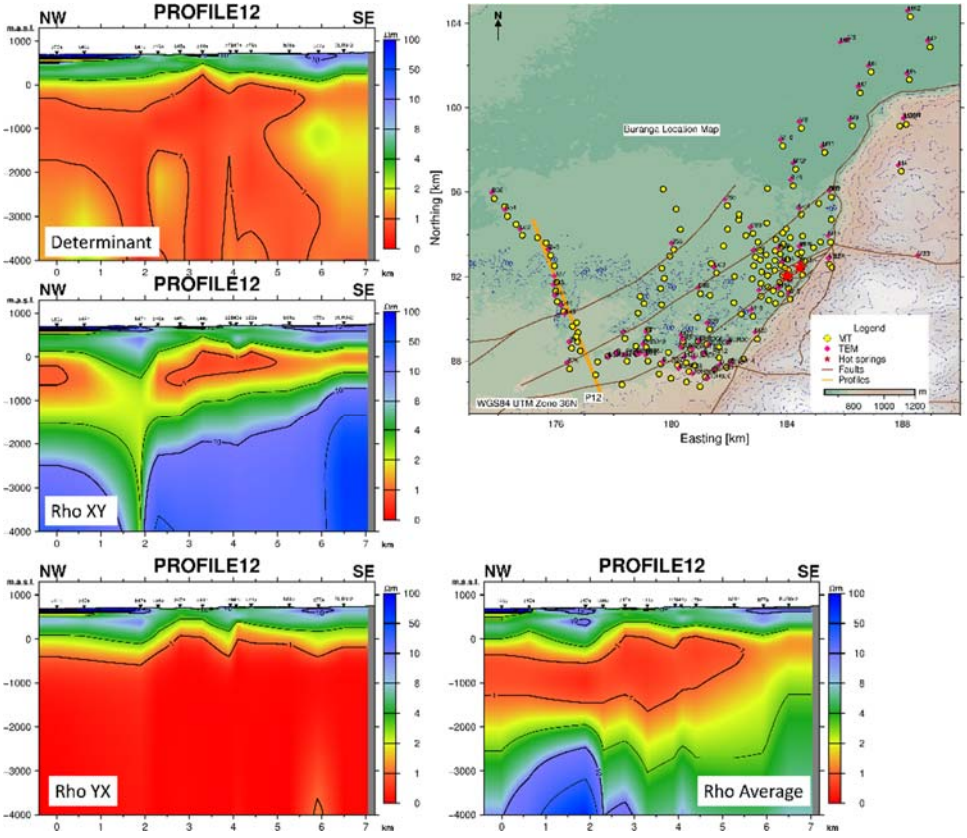

Figure 8.14: *Resistivity cross-sections based on the 1D inversion of the determinant, XY, YX and average apparent resistivity and phase. On the top right is a map showing the location of the cross-section. The MT stations on the profile from NNW-SSE are b50a, b49a, b47a, b46a, b45a,b44a,b28a,b43a,b29a,b31a,b77a,BUR042*

Cross section 12 (Figure 8.14) is in the southwestern part of the prospect area and is meant to investigate how the resistivity varies away from the area dominated by the surface manifestations. The cross-section runs in the NNW-SSE direction perpendicular to the local fault system of the area. Considering the XY cross-section, we see three distinct layers. A resistive surface layer (20-100 Ωm) is underlain by a conductive layer (0.1 -7 Ωm) about 2 km thick. From 3 km b.sl and downwards, there is a more resistive layer of 10-100 Ωm. The high resistivity at the surface represents the unaltered surface rocks, and the low resistivity corresponds to the altered clay cap minerals (smectite) usually sealing off the high resistivity reservoir at depth. The high resistivity at depth often seen in the reservoir rocks is probably due to high-temperature alteration producing high resistivity alteration minerals such as chlorite. Epidotes can also be produced in high-temperature geothermal fields although it's unlikely at Buranga since it's a low-temperature prospect. The alteration regime that can be

expected at Buranga falls in the smectite zone due to alteration temperatures predicted by geothermometry (Armannsson, 1994)

Cross section 20 SW-NE

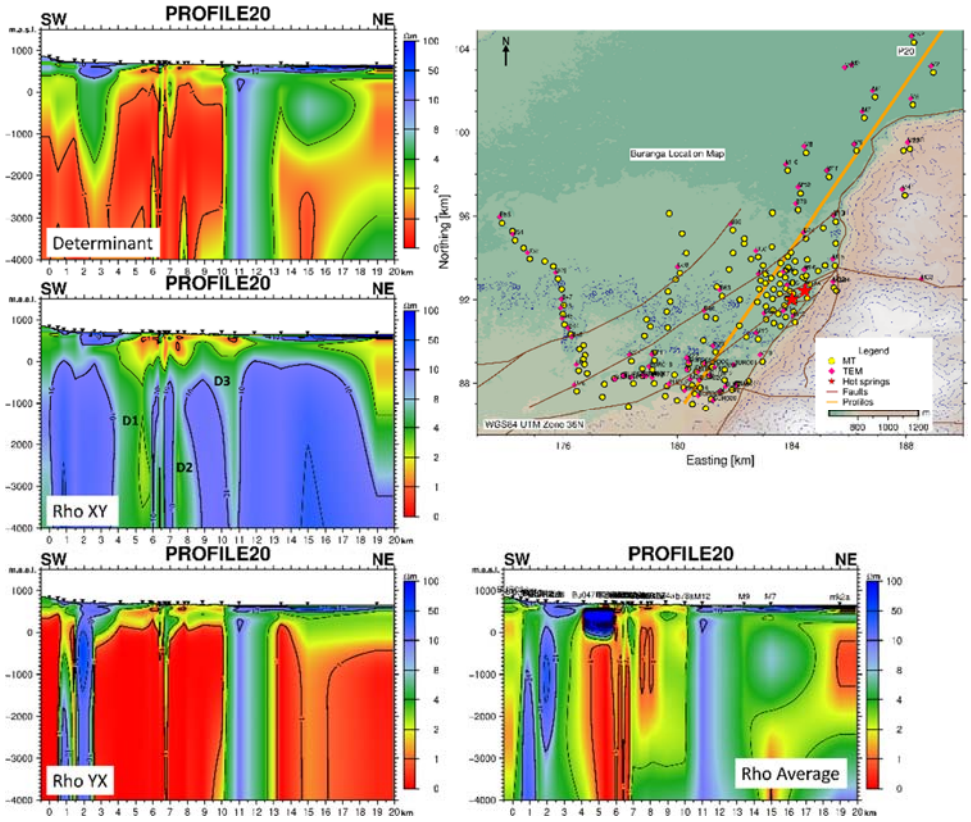

Figure 8.15: *Resistivity cross-sections based on 1D inversion of the determinant, XY, YX and average apparent resistivity and phase. On the top right a map showing the location of the cross-section. The MT stations on the profile from NW-SW are BUR037, BUR029, BUR020,BUR012,BUR007a,BUR006,b38,Bu047,b68a,Bura031a,Bura32a,Bura32a,Bura027a, M31,Bura025a, Bura036a,Bura028a,Bura039a,Bura019a,Bu025,b74a, b78a M12, M11, M9, M7, M4, Mk2a*

Cross section 20 runs SW-NE from the southern end of the prospect to the northeastern tip of the prospect area (Figure 8.15). This profile was constructed to investigate the resistivity boundary/contrast observed in the depth slices in Figure 8.7 a,b, 8.8 a, b and 8.9 a,b highlighted by a black dotted line.

The resistivity structure shown by the XY cross-section in Figure 8.15 mid-left shows three distinct horizontal resistivity layers. The surface layer has a resistivity of 8-20 Ωm extending to a depth slightly below sea level, the second layer is a more conductive layer with a resistivity of about 1-4 Ωm. Below this layer, there is a less conductive layer of about 10-100Ωm. However, it should be noted that there are three distinct vertical resistivity discontinuities along the profile, the first one, D1 is between *BUR020 and BUR012* coinciding with the first fault line shown on the location map, the second low resistivity

discontinuity D2 is located around the area of the surface manifestations between stations *Bura32a, Bura027a, M31, Bura025a, Bura036a, Bura028a, Bura039a.* This resistivity

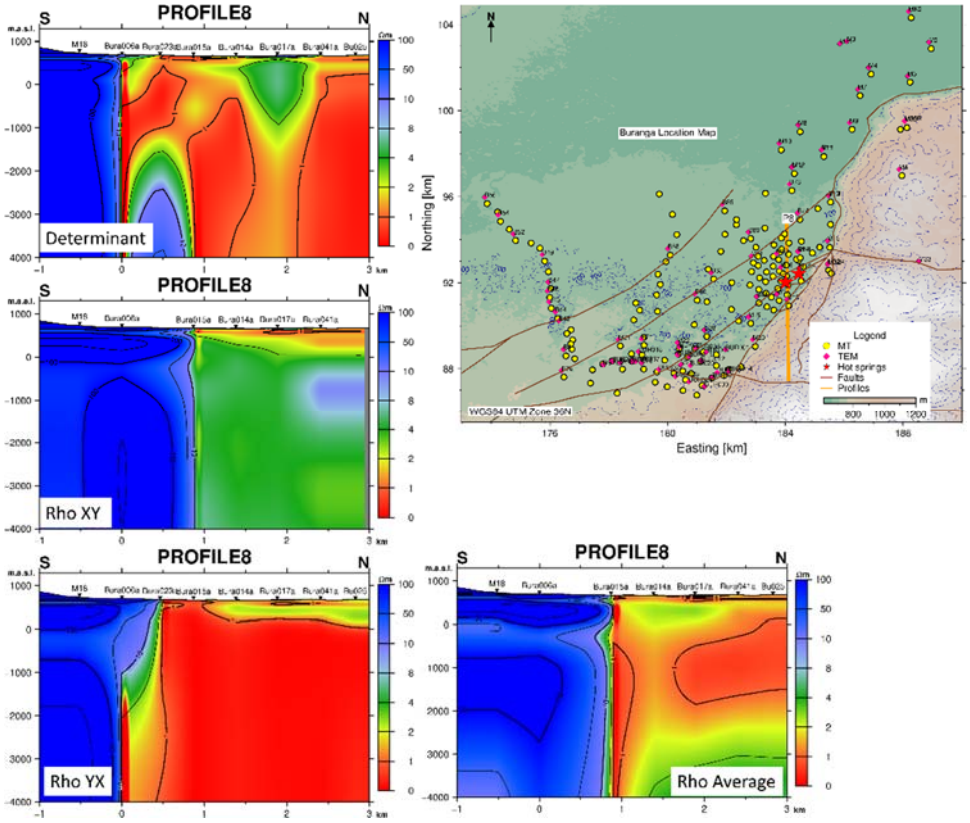

Figure 8.16: *Resistivity cross-sections based on the 1D inversion of the determinant, XY, YX and average apparent resistivity and phase. On the top right is the map showing the location of the cross-section. The MT stations on the profile from NW-SW are Bura006a, Bura023a, Bura015a,Bura014a, Bura017a, Bura041a, Bu025.*

boundary also coincides with the second fault step as shown on the location map. Beyond this fault step towards the northeast is another resistivity discontinuity D3, beginning at b74 and b78. This last discontinuity corresponds to the location of the resistivity discontinuity seen in the resistivity depth slices highlighted by the black dotted line. Therefore, it can be said that there is a concealed secondary NW-SE trending smaller fault around this area. This can also be observed in the topography of the area.

Profile 8 runs S-N through the hot spring area and was plotted to investigate the depth of the fault which could be acting as a conduit for the up-flow of geothermal fluids (Figure 8.16). From the XY and average cross-sections in Figure 8.16 mid left and bottom right respectively, it can be noted that this is a deep-seated fault extending beyond 4 km b.sl. This might well be the pathway for geothermal fluids to the surface and within the rift sediments creating the low resistivity zone observed in the middle of the cross-section as the geothermal fluids sip into the sediments.

8.5 2D Resistivity Models for Buranga

2D resistivity models were generated for profiles 1, 2 and 12, lying perpendicular to the geoelectrical strike according to both the Z-strike and T-strike (see Chapter 8.2). It is in the same direction as the regional geological strike. The data were rotated to N45°E, perpendicular to the profile direction and along the geoelectrical strike. The inversion code for GeoTools acts on the TE and TM mode as well as the tipper data T_{zy}. The inversion can be done separately for all modes, in pairs or all at once. The inversion seeks to obtain a minimum structure model subject to a certain acceptable level of misfit (see Chapter 7.5 above).

To carry out 2D modelling, a model is constructed on a rectangular grid of rows and columns

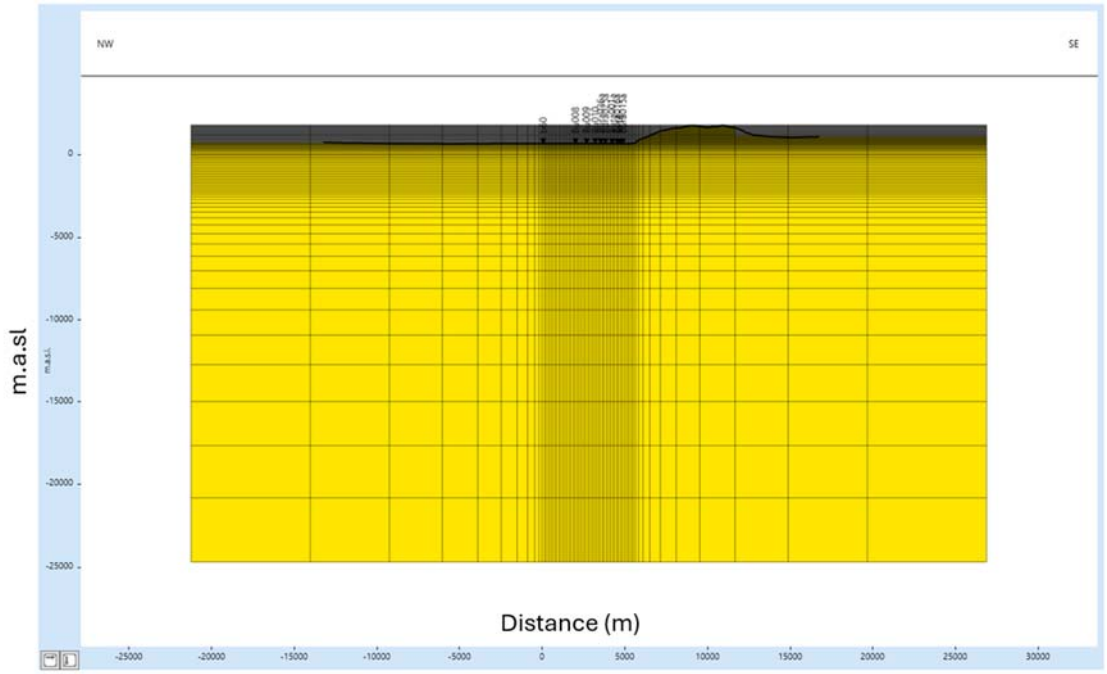

Figure 8.17: *2D inversion mesh grid for profile 1. The inverted red triangles at the top of the mesh represent MT stations on the profile.*

known as a regularization mesh (Bahr & Simpson, 2005). The grid consists of nodes in the y-z coordinate plane which form blocks or cells that have a uniform conductivity (Figure 8.17). The regularization mesh will remain fixed from one iteration to the next. For 2D modelling of data from Buranga, the regularization mesh shown in Figure 8.17 was constructed having a cell width of 125 m (usually four cells per site interval) and a padding factor of 1.5 that allows a 50% increase of the cell width outside the core area. A deep and wide padding of 25 km was used to fulfill boundary conditions helping to minimize edge effects and unwanted artifacts in the inversion process (CGG Multiphysics, 2019).

To test the convergence of the models, the resistivity of the starting models was set with a default fill (homogeneous starting model) of 100 Ωm for one set of inversion and 30 Ωm for the other set. 100 iterations were set for each inversion with an option of increasing them if the inversion did not converge within the first 100 iterations. Model sensitivity was tested

by varying different inversion parameters such as regularization type, smoothing weight and a priori weight. The results from these sensitivity tests are not presented here since they showed the same dominant resistivity structures with minor subtle variances. Static shift factors were also considered during the 2D inversion. When the option to invert for static shift is selected, the input data are the observed MT data corrected for user-set static shift factors obtained by adjusting the MT apparent resistivity curves based on collocated TEM soundings.

Using a 100 Ωm homogeneous starting model with the TM and TE mode noise floors set to 10%, TE and TM phase noise floors set to 5%, using a data frequency range of 0.01-1000 Hz, inversions were done for the TE, TM, TE+TM+T_{zy} and TE+TM modes in the NW-SE (perpendicular to the strike) oriented profiles 1, 2 and 12. Results from profile 1 are shown in Figures 8.18 – 8.21.

8.5.1 2D Inversion Results

Profile 1: NW-SE

Cross-section 1 is 5.4 km long and runs through the middle of the prospect area and within the hot spring area. 2D resistivity model results from the TE, TM, the combined TE+TM, and the combined TE+TM+T_{zy} mode show a conductive (≤ 2 Ωm) layer at the surface

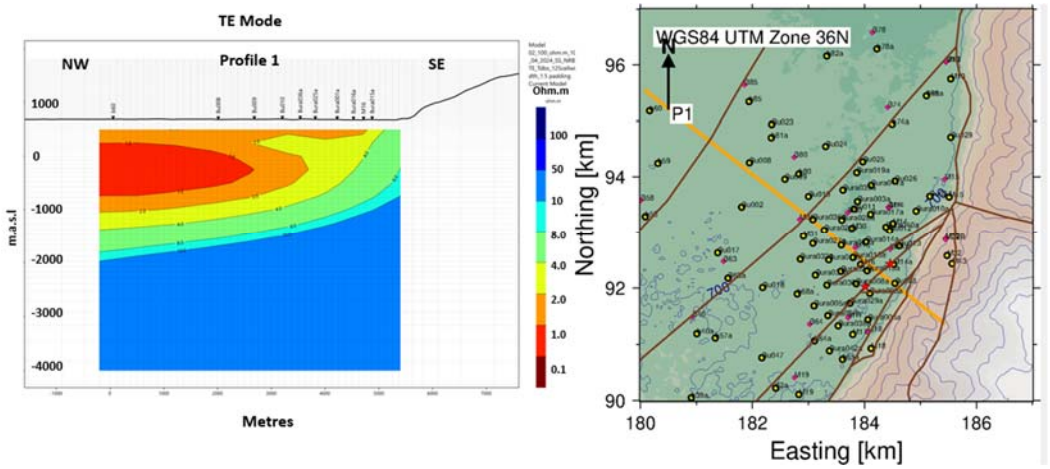

Figure 8.18: Profile 1; 2D resistivity model from the inversion of the TE mode. Location of the profile is shown on the figure to the right. Inversion converged after 100 iterations and an RMS of 1.02.

underlain by layers of increasing resistivity. Below the surface layer, there is a 4 Ωm layer underlain by an 8 Ωm layer which is also underlain by a 10 Ωm and a 50-100 Ωm layer down to a depth of about 4 km below sea level across the entire length of the profile. The depth of the cross sections has been clipped at 4 km below sea level because of poor data quality at longer periods especially for the TM mode. Therefore, the depth of resolution that we are confident about given the dataset at hand is slightly below 3 km b.sl. It is worth mentioning that below 4 km there is a conductive body (≤ 4 Ωm) present in the model that starts to show up from the centre of the profile towards the southeastern part beneath the exposed basement

rocks of the Rwenzori massif. This conductor beyond 4 km b.sl has been left out of the interpretation due to the resolution constraints of the data set.

The TM mode (Figure 8.19) exhibits some slight differences in terms of resistivity, thickness, and shape of the bottom layer. It depicts a high resistivity (≥ 100 Ωm) layer from sea level downwards for the entire length of the profile.

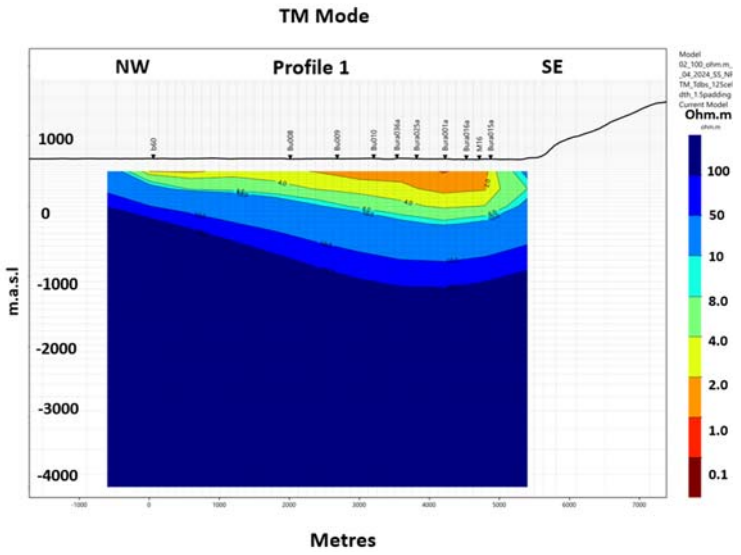

Figure 8.19: Profile 1; 2D resistivity model from the inversion of the TM mode. Inversion converged after 100 iterations and an RMS of 1.51.

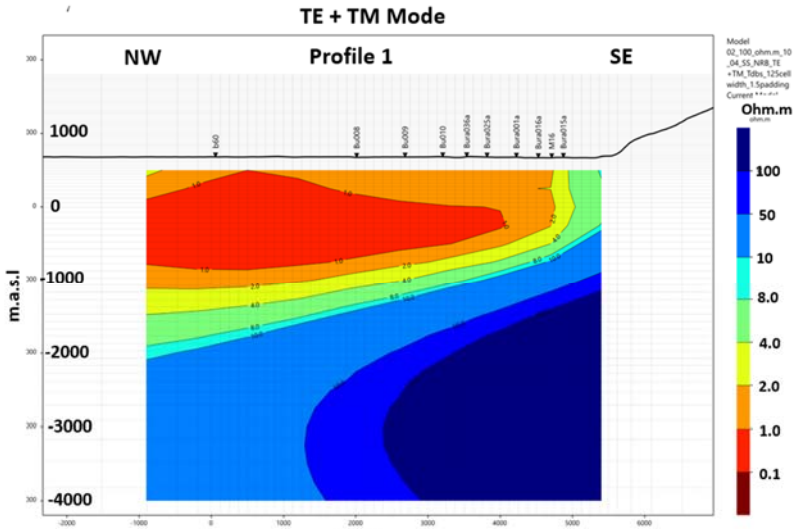

Figure 8.21: Profile 1; 2D resistivity model from the inversion of the TE+TM+Tzy modes. Inversion converged after 54 iterations and an RMS of 1.23.

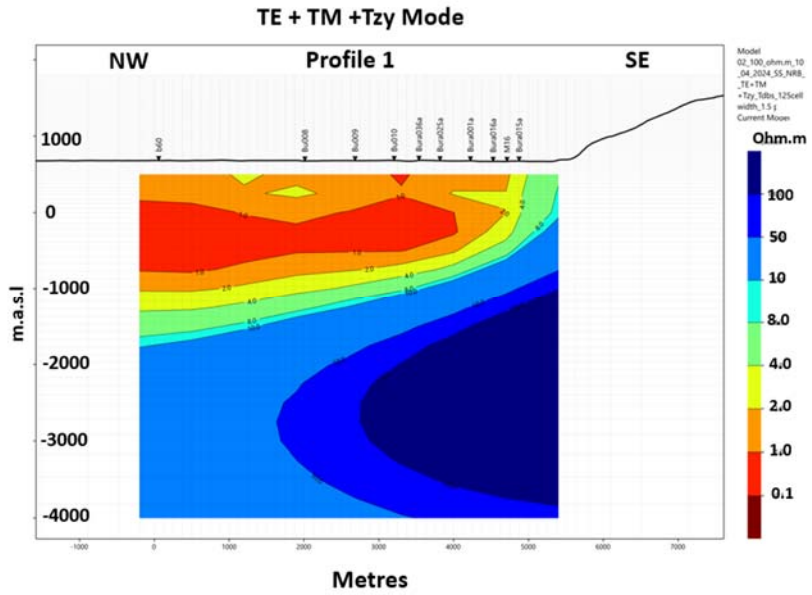

Figure 8.20: Profile 1; 2D resistivity model from the inversion of the TE+TM+Tzy modes. Inversion converged after 87 iterations and an RMS of 1.92.

To investigate how well the calculated data fit the measured data, model responses from the four 2D inversion modes (TE, TM, TE+TM, TE+TM+T_{zy}) were plotted together with the observed data, Figure 8.22 shows the data fit obtained for station b60 on profile 1 for the different modes. The TE mode exhibits the best fit between measured and calculated data followed by the TE+TM mode. However, considering the data complementary principle (Berdichevsky et al., 1998), where information from one mode is used to complement

information from another mode, the TE+TM mode inversion results are used in the characterization and interpretation of the resistivity structure at Buranga.

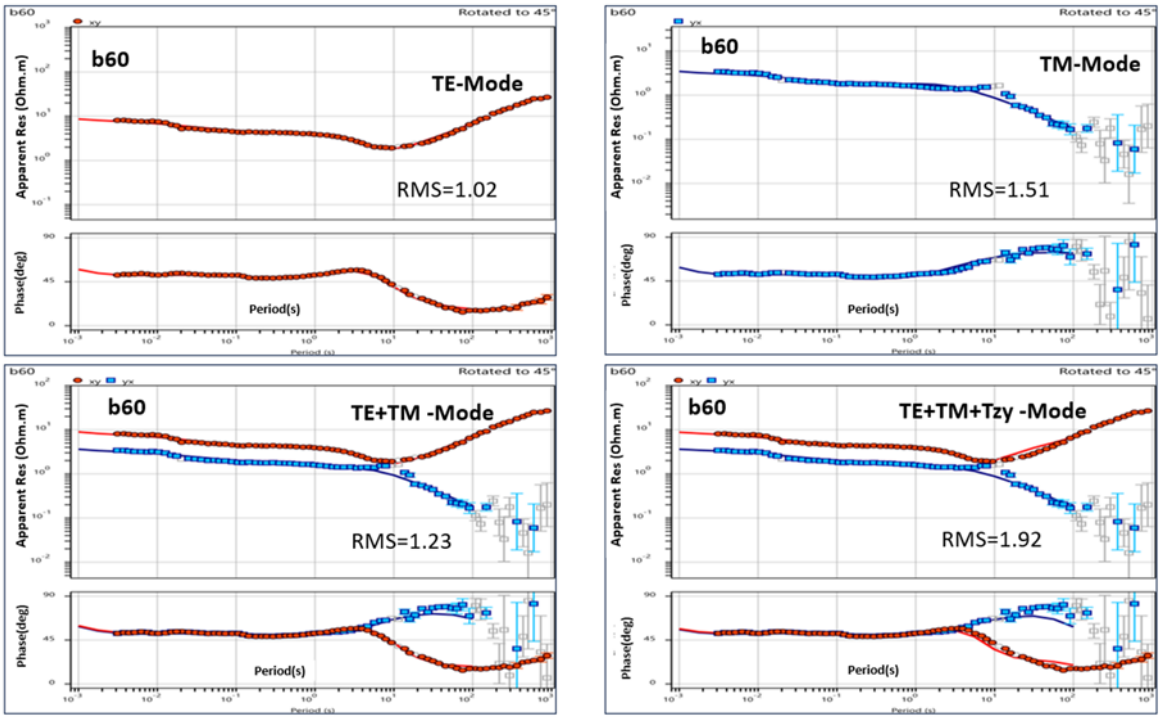

Figure 8.22: *Graphs showing the fit between the measured and calculated data obtained from 2D inversion of the TE, TM TE+TM and the TE+TM+T_{zy} modes for MT station b60. Red and blue dots are the measured data while red and blue lines are the calculated data.*

Profile 12: NNW-SSE

Cross-section 12 is on the southwestern part of the prospect area away from the area dominated by the surface manifestations. The cross-section runs in a NNW-SSE direction

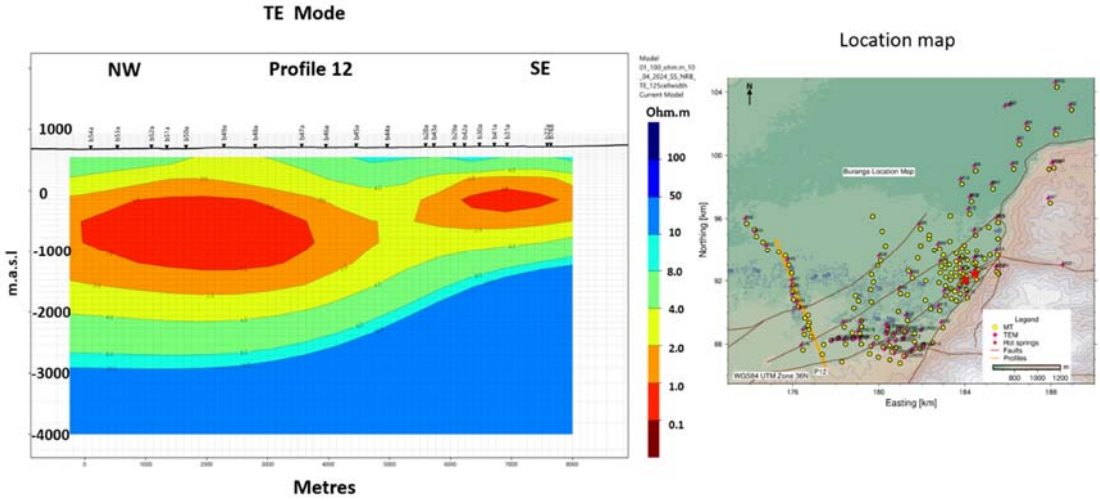

Figure 8.23: *Profile 12*; *2D resistivity model from the inversion of the TE+TM+T_{zy} modes. Inversion converged after 100 iterations and an RMS of 1.4. Location of the profile is shown on the figure to the right*

perpendicular to the local fault system of the area. Model results for profile 12 from the TE-mode, TM-mode, jointly inverted TE+TM and TE+TM+T_{zy} modes are shown in Figures 8.23, 8.24, 8.25, and 8.26, respectively. All modes show a surface layer (4-10 Ωm) across the entire length of the profile. The top layer is underlain by a more conductive layer (0.1-2 Ωm) segmented into two bodies in the TE mode, one to the far left towards the centre and the other to the far right of the profile. In the TE+TM and the TE+TM+T_{zy} modes, the conductive layer is continuous across the entire length of the profile.

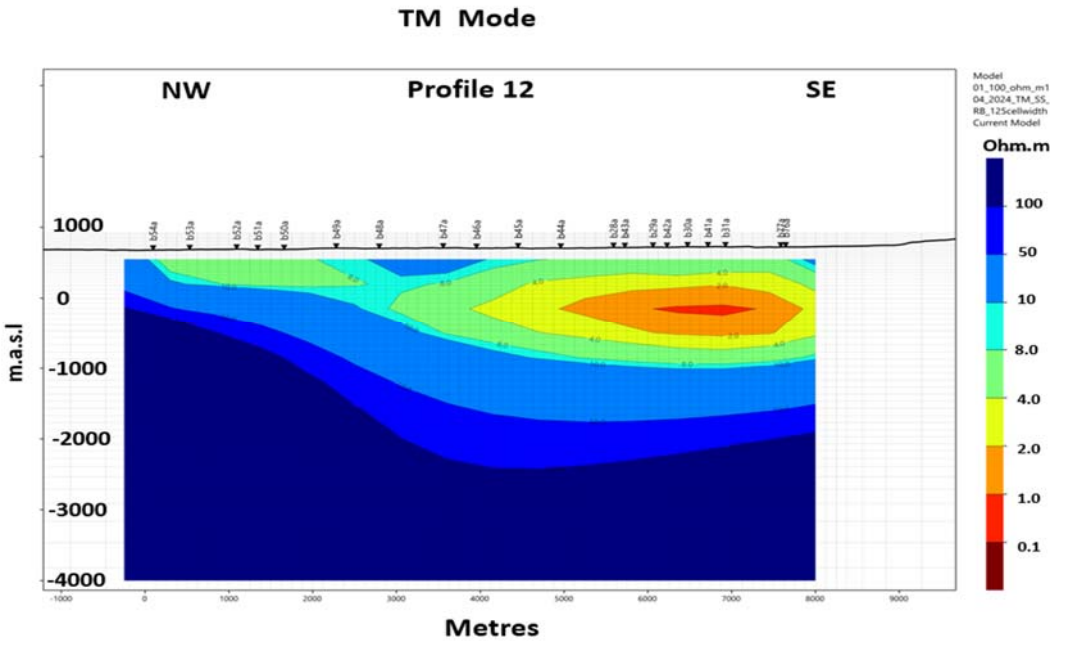

Figure 8.24: *Profile12*; *2D resistivity model from the inversion of the TM model. Inversion converged after 100 iterations and an RMS of 1.2.*

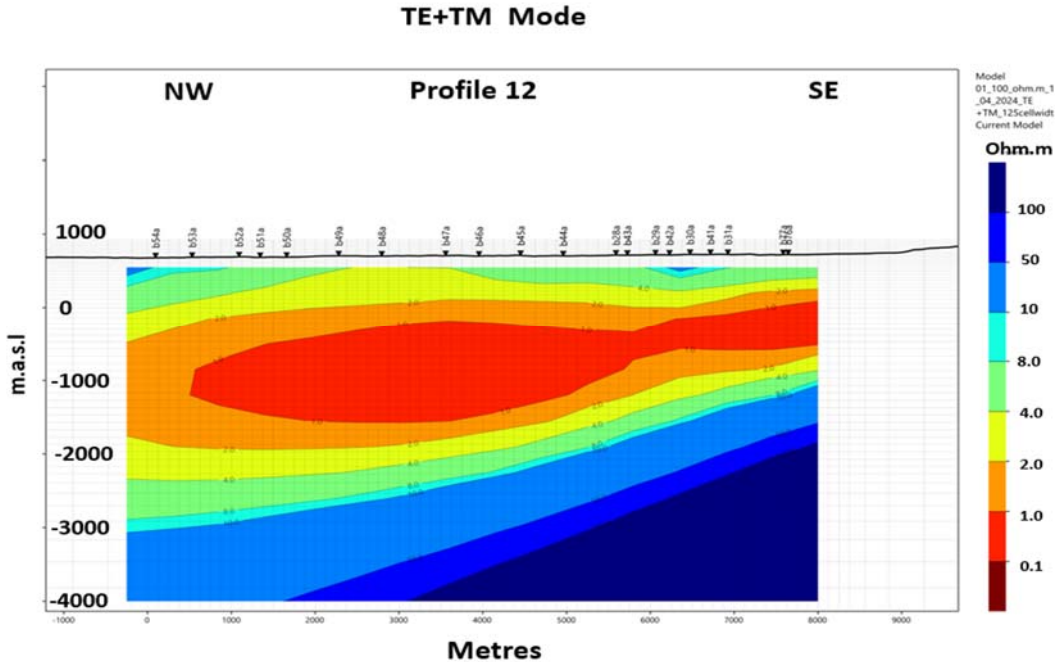

Figure 8.25: Profile12; *2D resistivity model from the inversion of the TE+TM mode: Inversion converged after 100 iterations and an RMS of 1.3.*

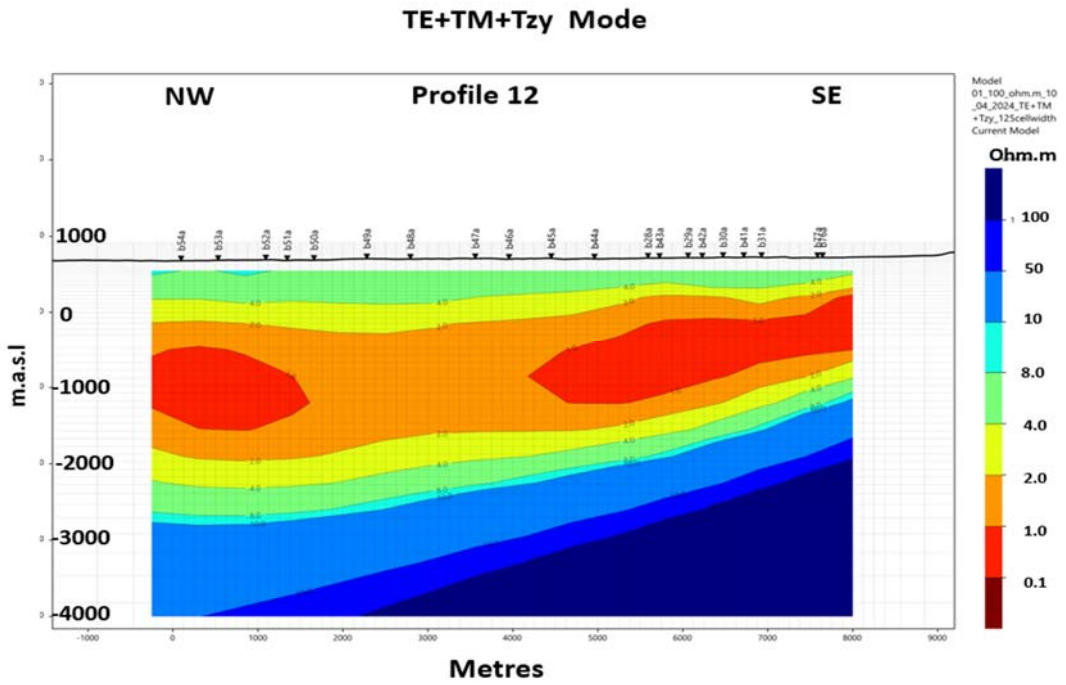

Figure 8.26: Profile12; 2D resistivity model from the inversion of the TE+TM+T_{zy} modes. Inversion converged after 131 iterations and an RMS of 1.5.

The 2D model from the TM mode differs from the other modes as it enhances the deep resistive structures more than the other modes. To avoid over or under approximating of structures by basing on inversion of a single mode say TE or TM, a bimodal inversion approach seems to be the most reasonable since gaps and shortcomings left by one mode are filled by another mode. Therefore, for interpretation purposes, the TE+TM or TE+TM+T_{zy} are more justifiable. Bimodal interpretation of the TE and TM modes satisfies the principle of information complementarity (Berdichevsky et al., 1998)

8.5.2 Comparison of 1D and 2D Results

Comparing the 2D models presented here (Figures 8.19 -8.26) and the 1D inversion results (Figures 8.12 -8.16), similarities are noted between the TE, TE+TM, TE+TM+T_{zy} modes and the 1D resistivity models generated from the XY apparent resistivity and phase. Both the 1D XY resistivity cross-sections and the 2D models highlight horizontal layers of varying resistivities with the most distinct ones being a surface layer of (4-10 Ωm) across the entire length of the 2D profiles underlain by a very conductive zone (0.1-2 Ωm). Below the very conductive layer lie several layers of progressively increasing resistivity from 2 Ωm to ≥ 100 Ωm. There is a discontinuity of this resistive layer in the 1D model probably due to some artefacts that mask the resistive basement rocks towards the SE of the profile. It is also important to mention that below 5 km, there is a conductive structure that is observed in the 2D models starting in the middle of the prospect area and extending under the Rwenzori

massif. However, due to the quality of the dataset at hand, the resolution of the models below 5 km cannot be trusted. Thus, the cross-sections have been clipped at 4 km b.sl.

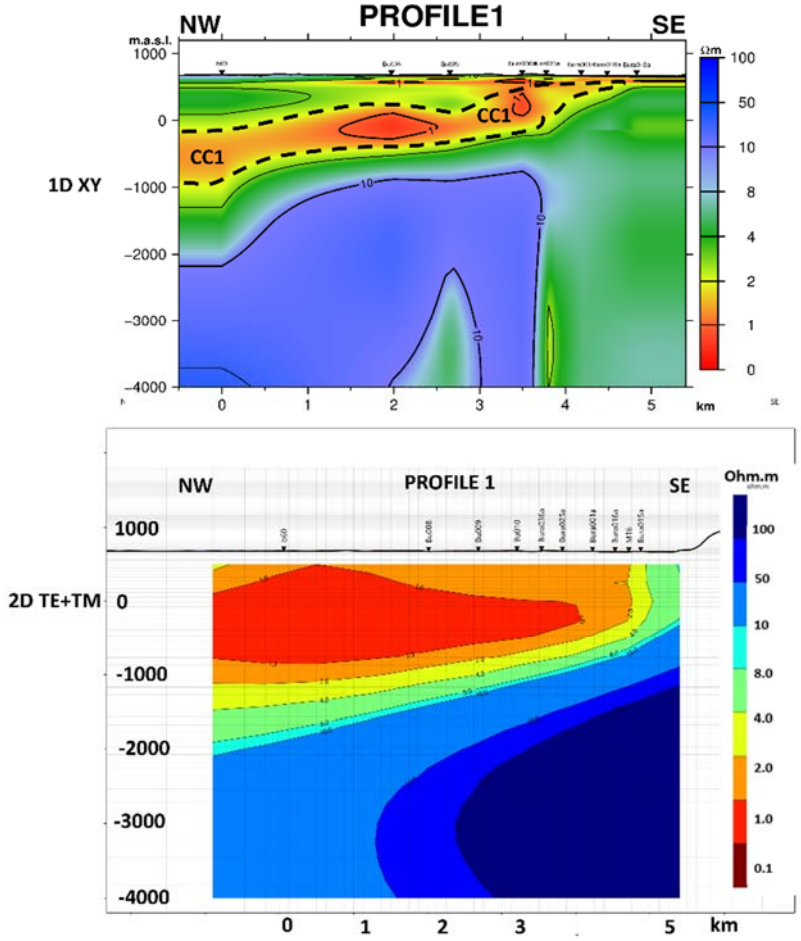

Figure 8.27: Profile 1; Comparison of resistivity cross-sections obtained through 1D joint inversion of TEM and XY MT data (upper part) and 2D inversion of the TE+TM mode of MT data (lower part) CC1 is the low resistivity layer that might be the seal cap of the geothermal system.

Although the 2D model shows a better representation of the sedimentary layers as well as the exposed basement rocks towards the southeastern end of the prospect, the 1D inversion of XY provides a better resolution of the thin low and high resistivity layers at the near subsurface. The low resistivity layer (CC1) highlighted by black dotted lines in the 1D cross-section in the upper part of Figure 8.27 is likely to consist of low-temperature alteration minerals/clays that act as a seal cap above the upflowing geothermal fluids that find their way to the surface at the hot springs through the permeable structures associated with the hostile fault zone.

8.5.3 Geothermal significance of 1D and 2D resistivity inversion results

Geothermal systems are known to exist in regions of elevated crustal heat flow where heat is transported to the upper crust mostly by convection through permeable zones such as faults, that control the fluid circulation. Heat sources usually comprise hot intrusive rocks

and shallow magma bodies or cooling intrusives. Some elements should be available for a geothermal system to exist, and these are a heat source, a geothermal reservoir, a clay cap (reservoir seal), permeable fluid pathways and geothermal fluids to transfer the heat. The elements of a geothermal system are not easily identifiable using conventional surface geological mapping but can be observed by using resistivity surveying techniques, especially MT. In a well-developed geothermal system, resistivity surveys highlight the clay cap as a very low resistivity layer due to the presence of highly conductive alteration minerals such as smectite resulting from the geothermal fluid-rock interaction. The reservoir is moderately resistive (due to high-temperature alteration minerals or slightly altered basement rocks) while a conductive signature usually highlights the heat source if seen below the reservoir. Unaltered basement rocks are depicted with the highest resistivity. Sedimentary regions usually have a low resistivity (Lévesque et al., 2023), at Buranga, the resistivity of sediments is lowered further due to the saturation of the sediments by geothermal fluids.

From geochemical analyses and geothermometry (Armannsson, 1994) Buranga has been characterized as a low-temperature sedimentary basin geothermal system with a possible maximum reservoir temperature of about 180^{o} C. Therefore, the classical high-temperature up-doming resistivity structure described in (Arnason et al., 2000; Eysteinsson et al., 1994; Hersir et al., 2022) is unlikely at Buranga and is not depicted by the results of this study. The resistivity structure at Buranga from this study can be summarized as follows.

A near-surface layers, R1 & R2 (Figure 8.28) comprising of highly resistive (50-100 Ωm) basement rocks starting at the border fault, F1 (Figure 8.28) in the SE part of the profile towards the Rwenzori massif and a conductive ($\leq$ 2 Ωm) layer, C1 (Figure 8.28) starting at the location of fault F3 to the NW of the profile underlain by layers of increasing resistivity marked as C2, C3, C4 and C5 in Figure 8.28. Below the surface layer, there is a 4 Ωm layer underlain by an 8 Ωm layer which is also underlain by a 10 Ωm and a 50-100 Ωm layer down to a depth of about 4 km below sea level across the entire length of the profile. The layers appear to be sheared towards the direction of the border fault.

Interpreting the resistivity units and the area's geology, the high resistivity on the southeastern end of the profile corresponds to the exposed basement rocks of the Rwenzori massif. These rocks continue downwards at a slanting angle similar to the border fault dip (60-65^{o}). These rocks have not been geothermally altered. The low resistivity layers starting at the border fault towards the northwestern end of the profile, correspond to a flat-lying series of sedimentary basin sands and clay-rich sediments whose resistivity has been lowered further by the percolation of geothermal fluids into these layers. This is because saturated sediments exhibit a remarkedly higher conductivity than unsaturated sediments (Lévesque et al., 2023). The geothermal fluid interaction with the rift polygenetic sands, grit, and biotite gneiss encountered during the drilling of boreholes at Buranga (McConnell & Brown, 1954) produces the low-resistivity clays that probably form the clay cap of the geothermal system. The geothermal fluids are brought to the surface through a network of permeable, negative flower fault system that might connect to one fault at depth and then forms numerous fault splays (Hinz et al., 2017) at the surface as evidenced by the surface geological map. The reservoir of the system could not be clearly defined from the resistivity model, but it is anticipated to be below 4 km b.sl. Upflow is by buoyancy-driven convection of geothermal fluids.

Beyond 5 km b.s.l, a conductive body starts to show up. However, this conductive structure has been excluded in the interpretations made here mainly because of poor data quality at

long periods hence, affecting our confidence in the data resolution beyond 4 km b.s.l. If confirmed by better quality data, this could represent an intrusive hot body that is the heat source for the Buranga geothermal system. The potential reservoir models would include permeability in the damage zone and fault splays within the faults and fractures along the N to NE striking, west-dipping faults.

8.6 Inferred Resistivity Conceptual Model

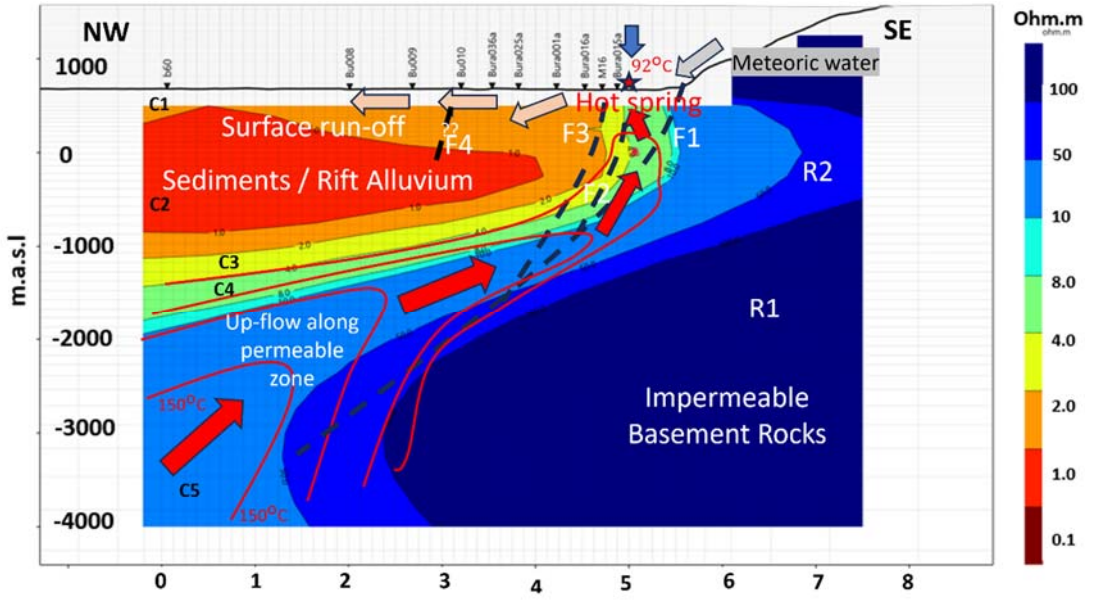

Figure 8.28: Preliminary conceptual model of the Buranga geothermal prospect; Isothermal lines are indicated in red while the red arrows indicate inferred up-flow direction. Recharge by meteoric water is shown by grey arrows while surface run-off is indicated by peach-colored arrows.

A preliminary conceptual model is presented from this study based on the resistivity data and other known geological and drilling information to help visualize the geothermal system at Buranga and facilitate decision-making on drilling targets for further exploration.

Geothermal surface manifestations are located only in the area surrounding the fault fractured zone hence indicating considerable permeability within these faults (F1, F2, and F3 indicated in Figure 8.28). The permeability has been verified from early drilling (Figure 2.4b) logs where a substantial loss of circulation was reported at depths between 180-190 m (McConnell & Brown, 1954). Beyond fault F4 towards the northwest, there have not been any recorded or visible geothermal manifestations (Hinz et al., 2017) which implies that either fault F4 is shallow and doesn't extend deep past the impermeable clay cap or that the fault has limited permeability due to the sealing effect of the calcareous clays that might have cemented the fault as observed in borehole 1 where the coarse breccias in the fault zone are cemented by calcareous tuffs at a depth of 173 m (McConnell & Brown, 1954). The

system can be thought to be hydrologically closed off since no evidence of mixing with cold water was noted from the mixing models (Armannsson, 1994). The conceptual model presented here is intended to depict a confined up-flow in fault-hosted permeability within the damage zones associated with the hostile faulting system. The isotherms are used to highlight a deep 150ºC up-flow ascending through a narrow zone of fault permeability shown by the wide spacing of the isotherms (Cumming, 2009) vertically as the fluid ascends through the structures.

8.7 Review of proposed temperature gradient holes

At the end of 2017, GRD staff and experts from EAGER completed a data review exercise for Uganda's three major geothermal prospects, i.e., Kibiro, Buranga and Panyimur. The review exercise was intended to assess the progress of exploration activities and plan for the next phase of action depending on the exploration stage at each site. At that time, 30 infill MT stations and 40 co-located TEM stations were recommended for Buranga together with focused structural geological mapping. In addition, 16 temperature gradient holes (TGHs) were proposed based on results from the available MT and TEM data (Cumming et al., 2017). The recommended infill MT survey was undertaken and incorporated into the data presented in this thesis. It is, therefore, important to review the effectiveness of the TGHs that were proposed at that time against the updated resistivity models presented in this thesis. Figure 8.29 shows the location of the proposed TGHs while Figure 8.30 shows TGH locations superimposed onto the 2D resistivity model from profile 1.

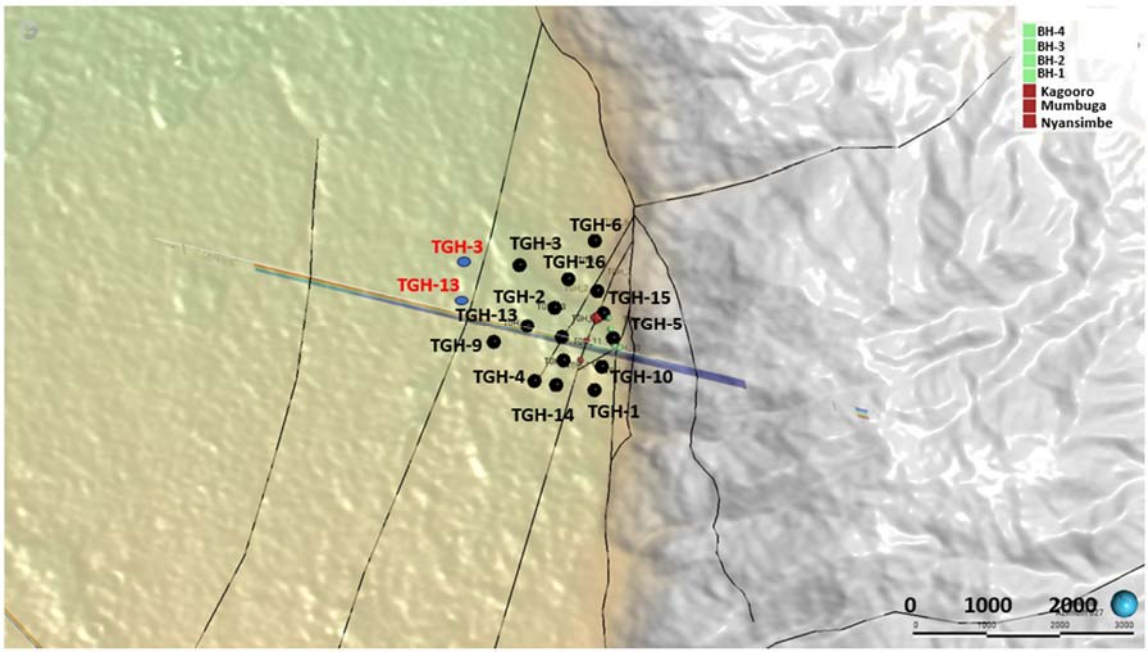

Figure 8.29: Map showing the location of proposed TGHs at Buranga (Cumming et al., 2017). TGHs highlighted in red represent suggested locations based on this study.

TGH drilling is an exploration method that aims to reduce the upfront risks associated with deep full-sized geothermal exploration wells in structurally controlled low-temperature

geothermal fields. TGHs help in assessing the up-flow and out-flow zones based on the temperature gradients obtained from the temperature logs of the gradient hole. The TGHs that were proposed by EAGER are mostly located around the area with the most surface manifestations and thus the predicted up-flow zone based on the updated resistivity model. Therefore, the locations for the TGHs within this heavily faulted zone are justifiable.

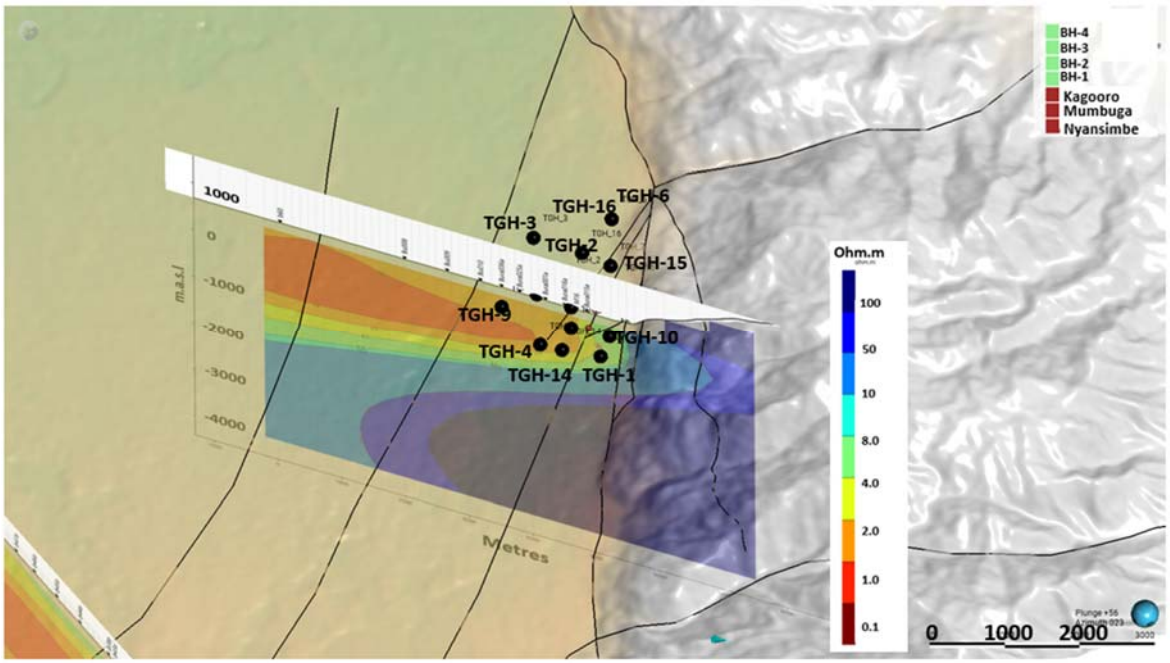

Figure 8.30: Map showing the location of proposed TGHs at Buranga superimposed on the 2D resistivity model from profile 1.

From the 2D resistivity model, the thickness of the sediments increases as one moves to the west from the border fault and, therefore, TGHs 2, 3, 9, 13 and 16 will only end up in the sedimentary layers since the planned depth of these TGHs is only about 300 m. Therefore, a staggered strategic approach should be adopted during the drilling campaigns such that priority is given to TGHs 5, 7, 10, 11, 12, 14, and 15 (the listing is not in any particular order of priority). We propose to shift the locations of TGH-3 and TGH-13 westward by 670 m and 950 m, respectively. The purpose is to investigate the temperature gradient west of the presumed barrier fault (F4) and extend the area of investigation beyond the surface manifestation zone. TGH 8 is located almost 10 km southwest of profile 12. It is unclear why this TG H was sited in this location, but it should not be drilled until it has been reviewed against the results of priority drilling and an updated conceptual model. Once the priority wells have been drilled, we can review and update the locations of the remaining TGHs such that they are more spaced to have better coverage of the area based on the initial drilling results.

9 Conclusions and Recommendations

In reconstructing the subsurface resistivity structure by modelling resistivity data, one is often faced with the ambiguity problem in which calculated data from multiple resistivity models can fit the same measured data making interpretation challenging and sometimes misleading. The ambiguity could stem from the limitations of the method employed such as resolution, sensitivity to subsurface geometry, effects of distortions and noise etc.

In this study, 1D joint inversion of MT and TEM data and 2D inversion of MT data were done. 1D models from the rotationally invariant determinant and average as well as the rotationally variant XY and YX apparent resistivity and phase were generated and compared with each other. The known geology of the area was used as a constraint to identify the 1D model that best represents the area. The XY mode was chosen to characterize the 1D resistivity structure most reasonably. 2D inversion of the MT data was also undertaken by inverting for the TE, TM, TE+TM as well as the TE+TM+Tzy modes. Three initial models (100, 30, and 10 Ωm homogeneous half-space models) were used to test the convergence and robustness of the 2D inversion. Final 2D models from all modes were compared in terms of RMS and data fit.

Inversion results from the 1D XY and average modes were comparable whereas models from the YX and determinant modes showed considerable disparities. Results from the 2D models from the three initial models reproduced resistivity structures that were consistent for all the modes except the TM mode which recovered a higher resistivity at depths of about 1 km downwards. Owing to the data complementary principle in which information from one mode (TE) is used to complement the information from another mode (TM), the 2D model from the bimodal inversion of the TE+TM modes is considered most reasonable in the characterization of the subsurface resistivity in two dimensions. Comparison of the 1D and 2D inversion approaches for the XY and TE+TM, respectively, shows that the results are comparable. Although the 2D model shows a better stratigraphic sequence of the sedimentary layers as well as the exposed basement rocks towards the southeastern end of the prospect, the 1D XY mode provides a better resolution of the thin low and high resistivity layers at the near subsurface which are of great importance for a geothermal system since they form the clay cap to the geothermal reservoir.

The subsurface resistivity structure at Buranga can be characterized as follows based on the two interpretation approaches (1D and 2D) of EM data; A near-surface layer comprised of highly resistive (50-100 Ωm) basement rocks starting at the border fault in the SE part of the profile towards the Rwenzori massif and a conductive ($\leq$ 2 Ωm) surface layer starting at the location of fault F3 (on which the three major hot springs lie) to the NW of the prospect area underlain by four layers of increasing resistivity. Below the surface layer, there is a 4 Ωm layer underlain by an 8 Ωm layer which is also underlain by a 10 Ωm and a 50-100 Ωm layer down to a depth of about 4 km b.s.l across the entire length of the profile. This layering highlights sediments of different depositional regimes to a depth of about 2 km b.s.l. Beyond 2 km b.s.l, we encounter slightly high resistivities probably due to minimally altered basement rocks. The layers appear to be sheared towards the direction of the border fault. Beyond 5 km b.s.l, a conductive structure shows up starting in the middle of the prospect area and under the Rwenzori massif. This structure has not been considered in this interpretation due to data resolution constraints. No high resistivity core or up-dooming was

detected at depth. Therefore, there is little or no high-temperature alteration to produce high-temperature alteration minerals such as epidote.

Therefore, Buranga can be classified as a low-temperature, deep-circulation amagmatic fault-controlled system extracting heat from the crustal heat flow. Up-flow is within the permeable damage zones and fault splays along multiple fault segments which are associated with the N to NE striking west-dipping faults.

A gravity survey can be undertaken within the area together with a local scale refraction seismic survey to map the topography of the basement. If such data exists from previous studies (oil and gas exploration), they should be reviewed and used to constrain the current model. In future, More MT soundings could be acquired at a more regular grid to allow for 3D modelling of the entire dataset to resolve the conductive structure observed at 5 km properly.

The proposed drilling of Thermal Gradient Holes (TGHs) should be undertaken in a strategic and phased approach. The initial priority should be given to drilling TGHs 15, 7, 12, 5, 14, 10, and 11. After completing these initial TGHs, the results should be carefully reviewed to inform the decision-making process. Based on the findings from the initial TGHs, the project team can then determine whether to relocate the remaining TGHs or proceed with drilling in the previously proposed locations. This staggered approach will allow the team to assess the data and make informed decisions before proceeding with the full drilling plan. Targeting deep exploration wells within the permeable fault zones should also be based on the results of the updated conceptual model.

References

Archie, G. E. (1942). The electrical resistivity log as an aid in determining some reservoir characteristics. *Transactions of the American Institute of Mining, Metallurgical and Petroleum Engineers*, *146*(01), 54-67. https://doi.org/10.2118/942054-G

Armannsson, H. (1994). *Geochemical Studies on Three Geothermal Areas in West and SouthWest Uganda* (UGA/92/002 & UGA/92E02).

Armannsson, H., Bahati, G., & Kato, V. (2007). Preliminary investigations of geothermal areas in Uganda, other than Katwe-Kikorongo, Buranga and Kibiro. *Final Report. ICEIDA, MEMD, Uganda*.

Árnason, K. (1989). Central Loop Transient Electro-magnetic Soundings Over a Horizantally Layered Earth. In G. D. National Energy Authority (Ed.). Reykjavik.

Árnason, K. (2006a). TEMTD (Program for 1D inversion of central-loop TEM and MT data). *ISOR–Iceland GeoSurvey*.

Árnason, K. (2006b). TemXshort manual. ÍSOR–Iceland GeoSurvey. *Reykjavik, manual*.

Árnason, K. (2008). *The magnetotelluric Static Shift Problem* (Report ISOR-08088,16 pp).

Árnason, K. (2015). The static shift problem in MT soundings. Proceedings world geothermal congress, Melbourne, Australia.

Árnason, K., Eysteinsson, H., & Hersir, G. P. (2010). Joint 1D Inversion of TEM and MT data and 3D Inversion of MT data in the Hengill area, SW Iceland. *Geothermics*, *39*(1), 13-34.

Arnason, K., Karlsdottir, R., Eysteinsson, H., Flóvenz, Ó., & Gudlaugsson, S. T. (2000). The resistivity structure of high-temperature geothermal systems in Iceland. Proceedings of the World Geothermal Congress 2000, Kyushu-Tohoku, Japan,

Bahati, G., Pang, Z., Ármannsson, H., Isabirye, E. M., & Kato, V. (2005). Hydrology and reservoir characteristics of three geothermal systems in western Uganda. *Geothermics*, *34*(5), 568-591. https://doi.org/https://doi.org/10.1016/j.geothermics.2005.06.005

Bahr, K., & Simpson, F. (2005). *Practical Magnetotellurics*. Cambridge University Press. https://doi.org/DOI: 10.1017/CBO9780511614095

Berdichevsky, M., & Dmitriev, V. (2009). *Models and Methods of Magnetotellurics, Springer, Berlin, 563 pp*. https://doi.org/10.1007/978-3-540-77814-1

Berdichevsky, M., Dmitriev, V., & Pozdnjakova, E. (1998). On two-dimensional interpretation of magnetotelluric soundings. *Geophysical Journal International*, *133*(3), 585-606.

Berdichevsky, M. N., & Dmitriev, V. I. (2010). *Models and Methods of Magnetotellurics*. Springer Berlin Heidelberg. https://books.google.is/books?id=-Fs8cPqeCcQC

Bromley, C. (2018). The role of advanced geophysical monitoring in improved resource expansion and make-up drilling strategy. Proceedings,

Caldwell, T. G., Bibby, H. M., & Brown, C. (2004). The Magnetotelluric Phase Tensor. *Geophysical Journal International*, *158*(2), 457-469.

CGG Multiphysics. (2019). *GEOTOOLS - Magnetotelluric and Time Domain EM Data Analysis*. In (Version 1.9.1.12310) CGG Electromagnetics.

Chave, A. D., & Jones, A. G. (2012). *The Magnetotelluric Method: Theory and Practice*. Cambridge University Press.

Christopher , S., Ochmann , N., Kato , V., Micheal , K., & Uwe , S. (2007). *Detailed surface analysis of the Buranga geothermal prospect, West-Uganda*.

Constable, S. C., Parker, R. L., & Constable, C. G. (1987). Occam's Inversion: A Practical Algorithm for Generating Smooth Models from Electromagnetic Sounding Data. *Geophysics*, *52*(3), 289-300.

Cumming, W. (2009). Geothermal resource conceptual models using surface exploration data. Proceedings,

Cumming, W., Hinz, N., Sussman, D., Heath, J., Nelson, I., & Marini, L. (2017). *Updated Exploration Plans For Panyimur and Buranga* (U23-D04). EAGER.

Dakhnov, V. N. (1962). *Geophysical Well Logging: the Application of Geophysical Methods*. https://books.google.is/books?id=H7K3tAEACAAJ

Didana, Y. L. (2010). *Multidimensional Inversion of MT data from Krysuvik High Temperature Geothermal Field,SW Iceland, and study of how 1D and 2D Inversion can reproducea given 2D/3D resistivity structure using synthetic MT data* University of Iceland.]. Reykjavik.

Didas, M. M., Armadillo, E., Hersir, G. P., Cumming, W., & Rizzello, D. (2022). Regional thermal anomalies derived from magnetic spectral analysis and 3D gravity inversion: Implications for potential geothermal sites in Tanzania. *Geothermics*, *103*, 102431.

EDICON. (1984). *Aeromagnetic Interpretation of Lake Albert-Edward portion of the Western Rift Valley* [Report].

Eysteinsson, H. (1998). TEMRESD, TEMMAP and TEMCROSS plotting programs. *ÍSOR-Iceland GeoSurvey, unpublished programs and manual*.

Eysteinsson, H., Árnason, K., & Flóvenz, Ó. G. (1994). Resistivity methods in geothermal prospecting in Iceland. *Surveys in geophysics*, *15*(2), 263-275.

Faulds, J., Coolbaugh, M., Vice, G. S., & Edwards, M. L. (2006). Characterizing Structural Controls of Geothermal Fields in the Northwestern Great Basin: A Progress Report. *Transactions - Geothermal Resources Council*, *30*, 69-76.

Faulds, J. E., & Hinz, N. H. (2015). Favourable tectonic and structural settings of geothermal systems in the great basin region Western USA: Proxies for discovering blind geothermal systems. World Geothermal Congress, Melbourne Australia.

Georgsson, L. S. (2009). Geophysical methods used in geothermal exploration. *Short Course on Surface Exploration for Geothermal Resources*.

Groom, R. W., & Bailey, R. (1991). Analytic investigations of the effects of near-surface three-dimensional galvanic scatterers on MT tensor decompositions. *Geophysics*, *56*(4), 496-518.

Harris, N., Pallister, J. W., & Brown, J. (1956). *Oil in Uganda*. Government Printer, South Africa.

Harvey, M. C., & Harvey, C. C. (2015). Soil CO2 flux surveys: a review of the technique in geothermal exploration. Proceedings world geothermal congress,

Heath, J., Sussman, D., Lonsdale, A., & Bayarsaikhan, M. (2018). Advancing Geothermal Development in East Africa: Lessons Learned During the 2015–2018 EAGER Programme. The Proceedings, 7th African Rift Geothermal Conference Kigali, Rwanda 31st October–2nd November,

Heimlich, C., Gourmelen, N., Masson, F., Schmittbuhl, J., Kim, S.-W., & Azzola, J. (2015). Uplift around the geothermal power plant of Landau (Germany) as observed by InSAR monitoring. *Geothermal Energy*, *3*(1), 2. https://doi.org/10.1186/s40517-014-0024-y

Hersir, G., & Arnason, K. (2009). Resistivity of Rocks. . In *Short Course on Surface Exploration for Geothermal Resource. UNU-GTP and LaGeo in Ahuachapan and Santa Tecla. El Salvador, 17-30th October,San Salvador, El Salvador: UNU-GTP and LaGeo*

Hersir, G. P., Guðnason, E. Á., & Flóvenz, Ó. G. (2022). 7.04 - Geophysical Exploration Techniques. In T. M. Letcher (Ed.), *Comprehensive Renewable Energy (Second Edition)* (pp. 26-79). Elsevier. https://doi.org/https://doi.org/10.1016/B978-0-12-819727-1.00128-X

Hill, G. J. (2020). On the Use of Electromagnetics for Earth Imaging of the Polar Regions. *Surveys in geophysics*, *41*(1), 5-45. https://doi.org/10.1007/s10712-019-09570-8

Hinz, N., Cumming, B., & Sussman, D. (2018). Exploration of Fault-Related Deep-Circulation Geothermal Resources in the Western Branch of the East African Rift System: Examples from Uganda and Tanzania. Proc. 7th African Rift Geothermal Conference,

Hinz, N., William, C. D., Sussman John, Heath, & Fred, B. (2017). *Structural Geology at Panyimur and Buranga* (U23-D02)[Unpublished report]. EAGER.

Huenges, E., & Ledru, P. (2011). *Geothermal energy systems: exploration, development, and utilization*. John Wiley & Sons.

Jiracek, G. R. (1990). Near-surface and Topographic Distortions in Electromagnetic Induction. *Surveys in geophysics*, *11*(2-3), 163-203.

Jones, A. G., & Groom, R. W. (1993). Strike-angle determination from the magnetotelluric impedance tensor in the presence of noise and local distortion: rotate at your peril! *Geophysical Journal International*, *113*(2), 524-534. https://doi.org/10.1111/j.1365-246X.1993.tb00905.x

Kaddumukasa, M., Nsubuga, D., & Muyodi, F. J. (2012). Occurence of Culturable Vibrio cholerae from Lake Victoria, and Rift Valley Lakes Albert and George, Uganda. *Lakes & Reservoirs: Science, Policy and Management for Sustainable Use*, *17*(4), 291-299. https://doi.org/https://doi.org/10.1111/lre.12009

Kahwa, E. (2012). *Geophysical exploration of high-temperature geothermal areas using resistivity methods – case study: Theistareykir area, NE-Iceland* (14).

Kahwa , E., Nishijima , J., & Fujimitsu , Y. (2020, 2nd-8th November). Subsurface Characterization of Panyimur Geothermal Prospect, NW Uganda using Magnetotelluric Data. African Rift Geothermal Conference, Nairobi, Kenya.

Kato, V. (2016). Geothermal Exploration in Uganda. In *SDG Short Course I on Exploration and Development of Geothermal, Kenya, 10–31 November 2016*.

Kato, V. (2018). Pre-Drilling Geothermal Investigation Surveys in Uganda. Proceedings of the 7th African Rift Geothermal Conference,

Keller, G. V., & Frischknecht, F. C. (1966). *Electrical methods in geophysical prospecting*. Pergamon Press.

Klusman, R. W., Moore, J. N., & LeRoy, M. P. (2000). Potential for surface gas flux measurements in exploration and surface evaluation of geothermal resources. *Geothermics*, *29*(6), 637-670. https://doi.org/https://doi.org/10.1016/S0375-6505(00)00036-5

Kristmannsdóttir, H. (1979). Alteration of basaltic rocks by hydrothermal-activity at 100-300 C. In *Developments in sedimentology* (Vol. 27, pp. 359-367). Elsevier.

Larsen, J. C. (1977). Removal of Local Surface Conductivity Effects from Low Frequency Mantle Response Curves. *Acta Geodaet, geophys. et Montanist. Acad. Sci. Hung. Tomus 12 (1-3)*, 183-186.

Lévesque, Y., Walter, J., Chesnaux, R., Dugas, S., & Noel, D. (2023). Electrical resistivity of saturated and unsaturated sediments in northeastern Canada. *Environmental Earth Sciences*, *82*(12), 303.

Lichoro, C. M. (2013). *Multi-dimensional Interpretation of Electromagnetic data from Silali geothermal field in kenya: Comparison of 1D, 2D and 3D MT Inversion* University of Iceland]. Haskolaprent, Falkagata 2,107 Reykjavik.

Lichoro, C. M. (2015). Comparison of 1-D, 2-D and 3-D inversion approaches of interpreting electromagnetic data of Silali Geothermal Area. Proceedings of the World Geothermal Congress, Melbourne, Australia,

Lichoro, C. M., Árnason, K., & Cumming, W. (2017). Resistivity Imaging of Geothermal Resources in Northern Kenya Rift by Joint 1D Inversion of MT and TEM Data. *Geothermics*, *68*, 20-32.

Lindenfeld, M., Rümpker, G., Batte, A., & Schumann, A. (2012). Seismicity from February 2006 to September 2007 at the Rwenzori Mountains, East African Rift: earthquake distribution, magnitudes and source mechanisms. *Solid Earth*, *3*(2), 251-264.

McConnell, R. B., & Brown, J. M. (1954). *Drilling For Geothermal Power at Buranga Hot Springs, Toro*.

Morley, C., & Wescott, W. (1999). Sedimentary environments and geometry of sedimentary bodies determined from subsurface studies in East Africa. *Geoscience of rift systems-evolution of East Africa. AAPG Studies in Geol*, *44*, 211-231.

NASA. (2023). *The Solar Wind across our Solar System*. NASA. Retrieved 1/29/2024 from https://science.nasa.gov/resource/the-solar-wind-across-our-solar-system/

Natukunda, J. F. (2010). Geology of Kibiro, Katwe and Buranga geothermal prospects of Uganda. Proceedings World Geothermal Congress, Indonesia, 11p,

Nyakecho, C. (2008). *Preliminary environmental impact assessment for the development of the Buranga geothermal prospect, Uganda* (25).

Ochmann, N., Lindenfeld, M., Barbirye, P., & Stadtler, C. (2007). Microearthquake survey at the Buranga geothermal prospect, western Uganda. Proceedings of Thirty-Second Workshop on Geothermal Reservoir Engineering,

Olmsted, F. H., & Ingebritsen, S. E. (1986). Shallow subsurface temperature surveys in the basin and range province—II. Ground temperatures in the upsal hogback geothermal area, West-Central Nevada, U.S.A. *Geothermics*, *15*(3), 267-275. https://doi.org/https://doi.org/10.1016/0375-6505(86)90104-5

Park, S., & Livelybrooks, D. W. (1989). Quantitative interpretation of rotationally invariant parameters in magnetotellurics. *Geophysics*, *54*(11), 1483-1490.

Pedersen, L., & Svennekjaer, M. (1984). Extremal bias coupling in magnetotellurics. *Geophysics*, *49*(11), 1968-1978.

Phoenix, G. (2005). Data processing user guide. Phoenix Geophysics Ltd., ON Canada.

Phoenix, G. (2015). *V5 System 2000 MTU/MTU-A User Guide. Version 3.0 July 2015,*. In (Version 3.0)

Polak, E. (1971). *Computational methods in optimization: a unified approach* (Vol. 77). Academic press.

Rodi, W., & Mackie, R. L. (2001). Nonlinear conjugate gradients algorithm for 2-D magnetotelluric inversion. *Geophysics*, *66*(1), 174-187.

Ssemuyaba, F. (2021). *Processing and 1D Joint Inversion of MT and TEM Resistivity Data from Buranga Geothermal Field, Uganda. Report* (24, 39 pp.).

Ssemuyaba, F., Arnason, K., Hersir, G. P., & Benediktsdotir, A. (2023). Analysis and 1D Joint Inversion of MT and TEM Resistivity Data from Buranga Geothermal Field, Uganda. . World Geothermal Congress, Beijing, China.

Swift, C. (1967). A magnetotelluric investigation of an electrical conductivity anomaly in the southern United States. *Ph. D. Thesis*.

Tezkan, B. (1999). A review of environmental applications of quasi-stationary electromagnetic techniques. *Surveys in geophysics*, *20*, 279-308.

Thiel, S. (2008). *Modelling and Inversion of Magnetotelluric Data for 2D and 3D Lithospheric Structure, with Application to Obducted and Subducted Terranes* University of Adelaide]. Australia.

Tikhonov, A. N., & Arsenin, V. Y. (1977). *Solutions of ill-posed problems* (F. John, Ed.). V.H Winston & Sons.

Vozoff, K. (1991). The Magnetotelluric Method. In M. N. Nabighian (Ed.), *Electromagnetic Methods in Applied Geophysics: Volume 2, Application, Parts A and B* (Vol. 3, pp. 677-682). Society of Exploration Geophysicists. https://doi.org/10.1190/1.9781560802686.ch8

Ylagan, R. F., Altaner, S. P., & Pozzuoli, A. (1996). Hydrothermal alteration of a rhyolitic hyaloclastite from Ponza Island, Italy. *Journal of Volcanology and Geothermal Research*, *74*(3), 215-231. https://doi.org/https://doi.org/10.1016/S0377-0273(96)00046-7

Zehner, R. E., Tullar, K. N., & Rutledge, E. (2012). Effectiveness of 2-meter and geoprobe shallow temperature surveys in early stage geothermal exploration. *Geothermal Resources Council Transactions*, *36*, 835-841.

Zhang, P., Roberts, R., & Pedersen, L. (1987). Magnetotelluric strike rules. *Geophysics*, *52*(3), 267-278.

Zonge Engineering & Research organization, I. (1993). *Zonge Data Processing TEM Data Averaging Program*. In (Version 7.2x)